A millimetre and submillimetre wave detector using cyclotron resonance in a Ga1-xAlxAs/GaAs heterojunction

Smith, Suzanne M.

Award date:
1991

Awarding institution:
University of Bath

A MILLIMETRE AND SUBMILLIMETRE WAVE DETECTOR USING CYCLOTRON RESONANCE IN A $Ga_{1-x}Al_xAs$/GaAs HETEROJUNCTION.

submitted by Suzanne M. Smith

for the degree of Ph.D

of the University of Bath

1991

ProQuest LLC
789 East Eisenhower Parkway
P.O. Box 1346
Ann Arbor, MI 48106-1346

ABSTRACT

The exploration of the submillimetre region of the spectrum has been restricted by the limited range of detectors operating within this wavelength band. The aim of this project was to investigate the potential of and to develop a novel millimetre and submillimetre wave detector. The detector was based upon the photoconductive cyclotron resonance signal from a modulation doped $Ga_{1-x}Al_xAs/GaAs$ heterojunction.

The $Ga_{1-x}Al_xAs/GaAs$ heterojunction detector was used to detect radiation from a Gunn oscillator (98 GHz), an Impatt oscillator (90 GHz, 180 GHz, 270 GHz), a klystron (113 GHz) and an optically pumped infrared laser (2.5 THz).

Four detector systems were developed during the course of the project. The preliminary experiments were carried out at Oxford University. The final system developed at Bath achieved a measured responsivity of 20 to 64 V/W for input powers of 7 to 100 μW showing an increase of over two orders of magnitude from preliminary measurements. The improvement was achieved in a compact system fitted within a standard Infrared Laboratories HD3 cryostat, with small permanent magnets taking the place of the bulky electromagnets used in the earlier detector systems. The responsivities quoted above made no allowance for losses within the detector system. An estimate of the detector's intrinsic responsivity carried out for the preliminary detector system gave a value of 5500 V/W.

The detector's noise equivalent power and time constant were also estimated giving values of 4×10^{-12} W $Hz^{-1/2}$ and 2×10^{-7} s respectively.

Table of Contents

LIST OF SYMBOLS

$\underline{A}$ - magnetic vector potential

a - broad dimension of rectangular waveguide

B - magnetic field - magnetic induction

b - narrow dimension of rectangular waveguide

C_{el} - electronic heat capacity

$D(\epsilon)$ - density of states

E - electric field

e - charge of an electron

F - effective electric field

$f(\epsilon)$ - Fermi-Dirac function

H - magnetic field intensity

h - Planck's constant

$\hbar$ - modified Plancks constant

I - electric current

j - current density

k_B - Boltzmann's constant

k - wavevector

k_F - Fermi wavevector

m_o - electron rest mass

m^* - effective mass of electron

l - zero impedance distance

N - Landau level index

N_{Ac} - net acceptor electron concentration

N_C - channel electron concentration

N_D - depletion layer electron concentration

N_{INV} - inversion layer electron concentration

n_L - degeneracy of Landau levels

P - power

P_B - black body power

P_e - power input per electron

P_N - noise equivalent power

p - momentum

q_{TF} - Thomas-Fermi screening parameter

$\Re$ - voltage responsivity

R - resistance

T_o - cryostat bath temperature

T_{el} - electron temperature

T_L - lattice temperature

t - time

U_e - increase in the total energy of a system of N electrons

U(z) - confining potential

V - voltage

V_B - blackbody noise voltage

V_D - detector noise voltage

V_N - total noise voltage

V_S - signal noise voltage

V_T - thermal noise voltage

v_d - drift velocity

W - probability of scattering

Γ - Landau level width

ϵ - energy

ϵ_F - Fermi energy

ϵ_{eff} - effective dielectric constant

ϵ_0 - energy of first subband

ϵ_{10} - energy between first and second subband

H - Hamiltonian for electron in a magnetic field

θ - scattering angle

κ - background dielectric constant

λ - wavelength

λ_c - waveguide cut-off wavelength

λ_g - waveguide wavelength

λ_o - free space wavelength

μ - chemical potential

ρ - resistivity

σ - conductivity

σ_0 - d.c. Conductivity

τ_m - momentum scattering lifetime

τ_q - quantum scattering lifetime

ψ - wavefunction of position and time

ω - angular frequency

ω_c - cyclotron angular frequency

CHAPTER 1 INTRODUCTION

The submillimetre region of the spectrum extending from 300 to 3000 GHz, is one of the last major windows in the electromagnetic spectrum to remain unexplored. The primary application for submillimetre wave technology has been basic scientific research including astrophysics, plasma diagnostics and laboratory spectroscopy. More recently this spectral range has been considered for space-based radar and communications systems.

The exploitation of the full potential of this region has been restricted by the limited range of devices which are capable of functioning within this wavelength band. The Schottky diode detector operates up to a frequency of around 300 GHz, while the indium antimonide hot bolometer has been used between 100 and 600 GHz, but with limited speed. Germanium bolometers are often used around 1000 GHz but are even slower. In fact, one of the most significant shortcomings has been the absence of a fast submillimetre detector. Submillimetre detectors can be used in two modes, either in direct detection or as a heterodyne receiver. A heterodyne receiver downconverts the submillimetre signal from a remote source by mixing it with a local oscillator signal. The

difference or intermediate frequency is usually in the microwave region so that it can be processed using conventional microwave techniques.

The aim of this project was to investigate the potential of and to develop a novel millimetre and submillimetre wave detector/mixer. The detector was based on cyclotron resonance in a modulation doped $Ga_{1-x}Al_xAs/GaAs$ heterojunction.

Chapter one describes the figures of merit that are used to characterise detectors. It then goes on to describe present day detectors and some of their shortcomings.

Chapter two describes the system concerned which is a modulation doped $Ga_{1-x}Al_xAs/GaAs$ heterojunction. The chapter explains how a two dimensional electron gas is formed at the junction of the two materials. It then goes on to describe the basis of magnetic quantization and cyclotron resonance in a two dimensional system. The chapter concludes with the advantages shown by a two dimensional system over a three dimensional system for use as a millimetre and submillimetre detector.

Chapter three describes the initial experimental set-up which was based at Oxford University. The chapter describes the preliminary results of experiments detecting signals from a 119 μm laser, a 98 GHz Gunn oscillator and a 90 GHz Impatt oscillator.

Chapter four describes the development of experimental apparatus for use at Bath University. The system consisted of a detector mounted inside a continuous flow cryostat, which was situated within an electromagnet. The radiation was coupled to the detector using a quasi-optical system. The detector could be illuminated while at 4.2 K. The chapter describes the results taken using this system to detect radiation from a 98 GHz Gunn oscillator.

Chapter five describes the development of a compact detector system fitted into a standard Infrared Laboratories HD3 cryostat, the type frequently used in current telescope detector systems. In the new system the detector was situated between two small permanent magnets mounted within the cryostat. A variable backshort was provided to optimise power absorption in the detector. The detector itself was mounted onto a quartz suspended substrate filter. The chapter describes results of detecting radiation from a 98 GHz Gunn oscillator and a 113 GHz klystron.

Chapter six discusses the results obtained in terms of the figures of merit used to evaluate millimetre and sub-millimetre detectors. The new detector is compared to an indium antimonide hot electron bolometer. The chapter then describes further work that needs to be carried out to completely characterise the detector.

Chapter seven concludes the thesis.

1.1 Detector parameters

The submillimetre part of the spectrum involves detection techniques similar both to those used in the near infrared and those used in the microwave region. In order to properly compare the performance of detectors it is necessary to define certain figures of merit, which describe performance under specified operating conditions [Kimmit 1970, Arams 1973]. This section describes the four principle figures of merit.

1.1.1 Responsivity

The purpose of a detector is to convert radiation into an electrical signal, thus the basic property defining the performance is the ratio of the electrical output to the incident power. This quantity is called the responsivity. The voltage responsivity, $\Re$, is defined to be the change in the root mean square (rms) signal voltage, dV, from the detector produced by a change, dP, in the power incident upon it.

$$\Re = \frac{dV}{dP}. \qquad 1.1$$

It is given in units of volts/watt.

1.1.2 Noise equivalent power

The minimum detectable power is described using a figure of merit relating the radiant power capable of producing a signal voltage equal to the noise voltage, that is a signal to noise ratio of unity. This is called the noise equivalent power (N.E.P.) and is defined as the rms value of the sinusoidally modulated radiant power falling upon the detector which will give rise to a rms signal voltage equal to the rms noise voltage of the detector.

The N.E.P. of a detector is given by

$$P_N = \frac{V_N}{R} \qquad 1.2$$

where V_N is the root mean square voltage produced by the detector as a result of all sources of noise. These sources are as follows :-

(i) The detector receives black-body radiation from its surroundings and as this radiation fluctuates in intensity a noise voltage V_B is produced.

(ii) Electrical fluctuations in the detector produce a noise voltage V_D. At a minimum this is the Johnson noise voltage, but it can be increased by noise, called shot noise, produced by the bias current through the detector.

(iii) There is a noise voltage V_A of the associated amplifier which can increase the observed noise in a complete detector system.

(iv) The fluctuation in the observed signal itself will produce a noise V_S, although this is usually small compared with the background radiation noise.

(v) Thermal noise from the heat sink to which the detector is attached gives rise to a noise voltage V_T.

In an ideal detector

$$V_B^2 \geq V_D^2 + V_A^2 + V_S^2 + V_T^2 \qquad 1.3$$

and the N.E.P. is equal to the fluctuations in the blackbody power P_B falling on the detector, so

$$P_N = P_B. \qquad 1.4$$

N.E.P. is usually referenced at 1 Hz bandwidth and expressed in units of watts / $\sqrt{hertz}$.

1.1.3 Spectral response

The spectral response defines the band of the spectrum to which the detector responds and the manner in which some figure of merit referring to excitation by monochromatic radiation varies within this band. The spectral response is

displayed as a graph having wavelength on the abscissa and a figure of merit of the detector on the ordinate. Frequently the ordinate is given as relative response, defined as the relative signal voltage per unit monochromatic radiant power.

1.1.4 Response time

One of the factors of paramount importance in the characteristics of a detector is the dependence of the detector response upon the rate at which the incident radiation is modulated. The detector has a response time which limits the rapidity with which it will respond to the chopped radiation. A detector with a long response time will still detect a fast modulating signal but will only give an averaged value.

It is the response time that determines the maximum usable intermediate frequency bandwidth, if the detector is to be used in a heterodyne mode. If the response time is too long, then a low intermediate frequency must be used because the mixer is not able to respond to rapid variation in power. It is important in heterodyne systems to use as large an intermediate frequency bandwidth as possible. The reasons for this are to obtain a large information bandwidth, to reduce the frequency stability requirements for the local oscillator and to avoid noise close to the nominal local oscillator frequency.

1.2 Available detectors

The principle detectors currently available for the sub-millimetre band include Schottky diodes, hot electron bolometers and germanium bolometers [Frerking 1987]. The superconductor-insulator-superconductor, SIS, detector currently works up to a frequency of approximately 230 GHz, leaving it just outside the submillimetre band. Current SIS development aims to increase this high frequency limit.

The detection mechanisms of these devices rely upon one or more of three basic physical effects.

The first of these is non-linear current-voltage characteristics. Consider a device for which the current is a quadratic function of the voltage, such that

$$I = \alpha V^{2.} \qquad 1.5$$

When an electromagnetic signal is applied, where

$$V = V_o \cos(wt) \qquad 1.6$$

then the resultant current will be

$$I = \alpha V_o^2 \cos^2 wt. \qquad 1.7$$

This can be expressed as

$$I = \frac{\alpha V_o^2}{2}\{1 + \cos 2\omega t\} \qquad 1.8$$

The first part of this constitutes a d.c. component, which is directly proportional to V_o^2 and therefore to the power of the a.c. input. Therefore it can be used to directly detect power.

The current does not have to be a quadratic function of the voltage, as any non-linearity will produce a d.c. component related to the power of the incident electromagnetic wave. Therefore if a device has any non-linearity in its current-voltage characteristics it can be used as a detector.

The second mechanism of detection relies upon the bolometric effect. In this type of device, the radiation is absorbed and heats the detector. The detector is constructed from a material with a high temperature coefficient of resistance. The detector is arranged so that when the absorption of the radiation causes its temperature to rise, the resulting change in resistance can be measured. The change in resistance is used as a direct measure of incoming signal power.

The final detection mechanism evolves from quantum effects. In these detectors individual quanta of input radiation release charge carriers, usually by excitation across a forbidden energy band between bound and free current carrying states.

1.2.1 Schottky diode detector

The most widely used detector/mixer element at microwave and millimetre wavelengths is the Schottky barrier diode [Cronin 1985]. It consists of a small metal contact deposited on a semiconductor (usually GaAs). Rectification occurs in Schottky barrier diodes because of the differences in the Fermi level in the metal and semiconductor. The Fermi level in the metal is usually lower than in the semiconductor. Therefore when the two are brought into contact, some of the electrons move spontaneously into the metal. These leave behind ionised donor locations, which are positively charged and create a negative charge where they collect on the surface of the metal. An electric field is set up between these charges and the electrons that eventually prevents further electron flow into the metal. When a forward bias is applied, the energy of the electrons in the semiconductor is increased relative to the barrier height, allowing increased electron emission from the semiconductor to the metal. Under reverse bias the electron energy is lowered and the electron emission is reduced.

In general, conduction in Schottky barrier diodes is due to a combination of two types of electronic processes (i) thermionic emission and (ii) field emission. The former consists of electrons with sufficient thermal energy to cross the barrier and the latter consists of electrons that

tunnel through the barrier. The current is an exponential function of the voltage, which enables it to be used as a detector.

The Schottky barrier is a wide bandwidth, i.e. fast, device having a high sensitivity and good mechanical stability. It can be operated satisfactorily at room temperature, but its sensitivity can be increased by cooling. Its high frequency performance, however, relies on the very low capacitance of the rectifying junction. Therefore the area of the junction must fall as the operating frequency increases. So the upper frequency limit depends upon the accuracy achievable by photolithographical techniques. Another fundamental limitation of the Schottky barrier diode, as far as mixer applications in the submillimetre wave band are concerned, is the high local oscillator power requirement, being in the order of 0.1-1 mW [Frerking 1987].

1.2.2 Hot electron indium antimonide bolometer

The use of indium antimonide as a detector is due to Putley [1960, 1961] and this type of detector is often described as the "Putley detector". He discovered in 1960 that millimetre and submillimetre radiation increased the mobility of electrons in indium antimonide held at a temperature of 4.2 K. This may be attributed to the so called hot electron effect [Kogan 1963]. At low temperatures the coupling between the free carriers and the lattice is weak.

The application of an electromagnetic field results in electrons absorbing energy. The kinetic temperature of the conduction electrons is raised above the lattice temperature producing a change in their mobility. Consequently the detectors resistance is changed. The scale of the effect is such that it can only be seen at very low temperatures. At normal temperatures the heated carriers would give up their thermal energy to the lattice which, having so great a thermal capacity would be relatively unaffected. Putley originally used the detector in a magnetic field. An alternative system without a magnetic field was first proposed by Rollin [1961] and developed by Kinch and Rollin [1963]. This is sometimes referred to as the "Rollin detector".

The detectors are once again operated at cryogenic temperatures. They have a high responsivity and low noise. The weakness of indium antimonide detector lies in the comparative slowness of the response compared with the Schottky barrier diode. Typical response times are in the region of 10^{-6} s [Q.M.C. Instruments 1991] giving a maximum intermediate frequency of 1MHz when used in a mixer system.

1.2.3 Germanium bolometer

In germanium doped with a concentration of 10^{16} to 10^{17} cm^{-3} of impurities, usually gallium or indium, a marked bolometric effect is observed at liquid helium temperatures. Pure

germanium is transparent to submillimetre radiation and it appears that the impurity carriers are responsible for absorbing the radiation. Unlike the indium antimonide hot electron bolometer the carriers are tightly coupled to the lattice and the energy absorbed by them raises the temperature of the whole detector, thus changing its resistance. The Germanium detector is intrinsically slow having a time constant of 10^{-3} to 10^{-4} s [Arams 1973].

1.2.4 Superconductor-insulator-superconductor detector

Superconducting tunnel junctions consist basically of a Josephson junction in which two superconducting electrodes are separated by a thin insulating layer. They operate by utilizing either the Dayem-Martin effect [Dayem and Martin 1962] which involves a single quasi-particle tunnelling current or the Josephson effect [Josephson 1962] which involves a pair tunnelling current. The acronym SIS, superconductor-insulator-superconductor, is generally used for devices employing the first effect, which has been found to yield the best performance for low noise applications.

The physical effect involved in SIS detectors was first observed by Dayem and Martin in 1962. Burstein [1961] had discussed the use of tunnelling between two superconducting films for the quantum detection of microwave and sub-millimetre wave radiation. If the microwave frequency ν is

such that $h\nu > 2\epsilon_1$, an electron pair in metal 1 may be excited across the gap and subsequently tunnel through the barrier in metal 2. This is shown schematically in figure 1.1(a).

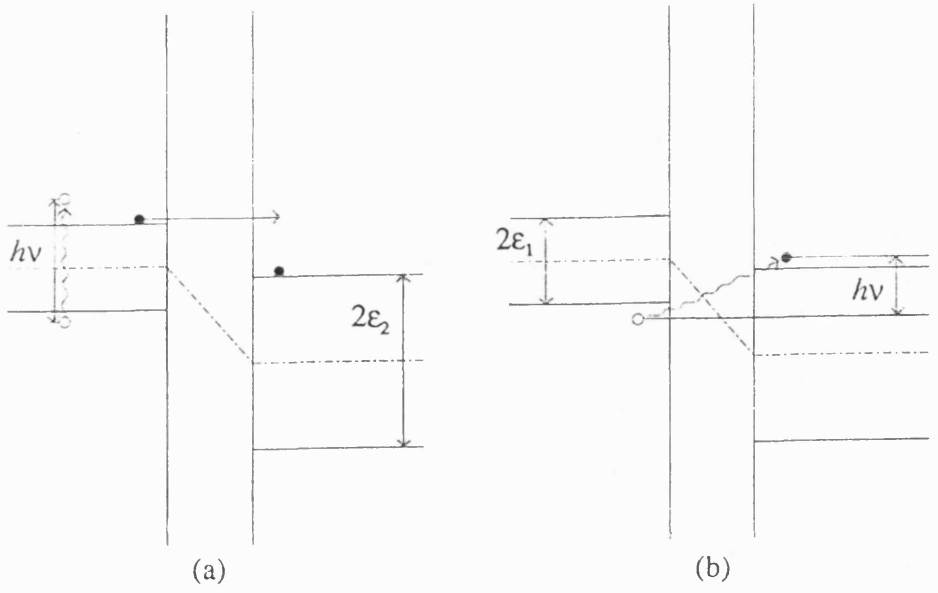

FIGURE 1.1 (a) Optical excitation across the gap of metal 1 followed by tunnelling through the barrier to metal 2, $h\nu > 2\epsilon_1$. (b) Photon absorption by a tunneling electron, $h\nu < 2\epsilon_1$.

If this was the only possible interaction with the electromagnetic field, no change in tunnelling current would be observed for $h\nu < 2\epsilon_1$. Dayem and Martin noticed experimentally, however, that considerable interaction with the microwave field occurs for $h\nu < 2\epsilon_1$. Their experimental

results suggested that with a bias voltage which brings the top of the filled band on one side of the barrier to a level lower by an amount $h\nu$ from the bottom of the empty band on the other side, an electron may absorb a photon and tunnel from one side to the other as shown in figure 1.1(b). Therefore it can be seen that by monitoring the appropriate region of the current-voltage characteristics shown by the junction the presence of incident radiation can be detected.

SIS detectors are operated at cryogenic temperatures. In addition to their inherent low noise, one of the primary advantages of SIS detectors is the low level of local oscillator power , 1 μW, required when used in a heterodyne system [Frerking 1987]. A fundamental high frequency limit of the SIS detector is set by the superconducting energy gap. The practical limitation for the high frequency operation of the detector, however, is its parasitic capacitance and resistance. It relies on a small area junction for its high frequency performance and therefore is dependent upon the accuracy achievable by photolithographical techniques.

CHAPTER 2 THE $Ga_{1-x}Al_xAs$/GaAs HETEROJUNCTION DETECTOR

2.1 $Ga_{1-x}Al_xAs$/GaAs heterojunctions

Modulation doped $Ga_{1-x}Al_xAs$/GaAs heterojunctions, with x typically having the value 0.33, consist of a wide band-gap $Ga_{1-x}Al_xAs$ layer grown onto a narrower band-gap layer of GaAs. The resultant band structure is shown in figure 2.1.

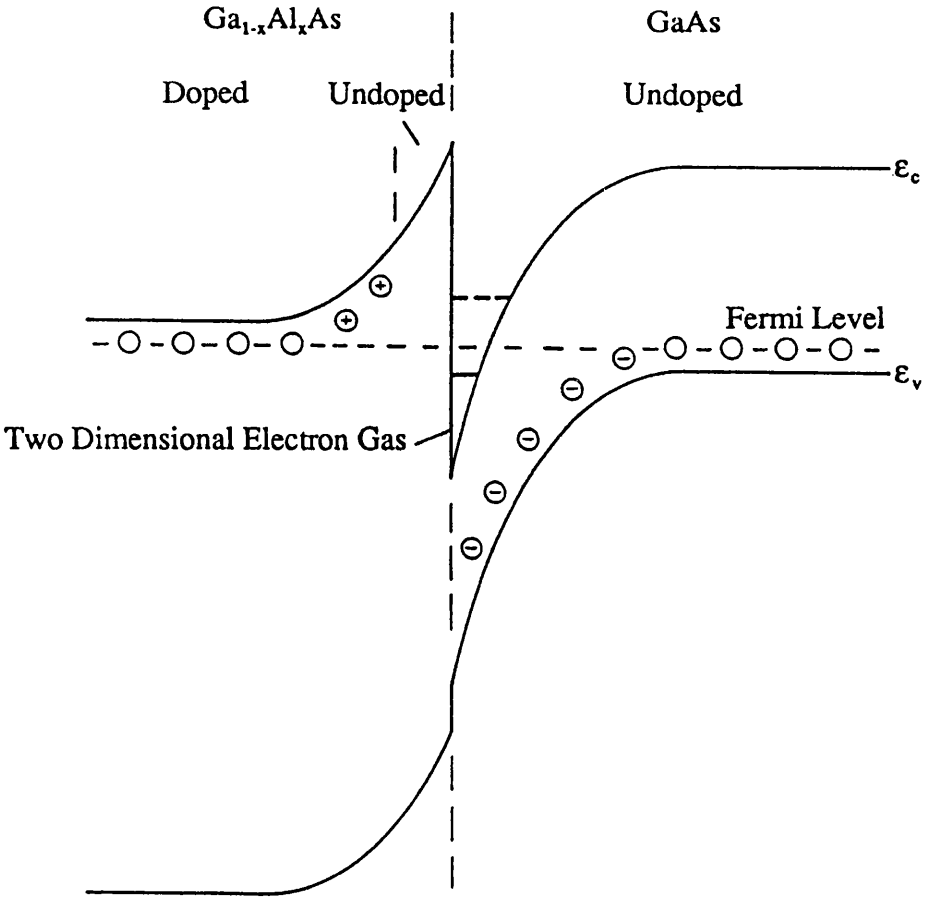

FIGURE 2.1 Band bending in a modulation doped $Ga_{1-x}Al_xAs$/GaAs heterojunction.

It is possible using molecular beam epitaxy to grow atomically sharp interfaces between these two materials. Molecular beam epitaxy is a refined form of vacuum evaporation in which directed beams of atoms or molecules are condensed onto a heated substrate under ultra-high vacuum conditions. The particular merits of the technique are that thin films can be grown with precise control over thickness, composition and doping level. The composition and dopant concentrations can be changed abruptly (within a few Angstroms) or continuously, permitting previously unobtainable structures to be prepared. The growth technique is described in detail by Foxon and Harris [1986].

A dopant impurity, usually silicon, is incorporated into the $Ga_{1-x}Al_xAs$ layer and free carriers from this region can diffuse into the undoped GaAs. There is a positive charge left on the dopant impurity which attracts these electrons to the interface, causing an accumulation layer to be formed in the GaAs at the heterojunction. The conduction band discontinuity at this point provides a potential barrier which restricts the return of electrons into the $Ga_{1-x}Al_xAs$. The transfer of electrons from the $Ga_{1-x}Al_xAs$ to GaAs will continue until the dipole layer formed from the positive donors and the negative electrons is sufficiently strong. The dipole layer gives rise to a potential discontinuity which makes the Fermi level of the GaAs equal to that of the $Ga_{1-x}Al_xAs$. The band bending in the GaAs caused by the

accumulation region produces an approximately triangular, one-dimensional potential well perpendicular to the interface. Carrier motion in the perpendicular direction is quantized, forming a set of bound energy states. Electron motion along the interface remains unhindered forming a two dimensional electron gas 2DEG [Stormer et al. 1979]. These electrons have a high mobility due to the reduction in ionised impurity scattering (the limiting factor for the low temperature mobility) which is caused by the spatial separation of parent donors and free electrons [Hess 1979]. The effect can be further enhanced by inserting an undoped $Ga_{1-x}Al_xAs$ spacer layer between the mobile electrons in the GaAs and the ionised impurities in the doped $Ga_{1-x}Al_xAs$, as shown in figure 2.1.

The spacer layer further reduces the strength of the Coulomb potential of the ionised impurities in the doped $Ga_{1-x}Al_xAs$ layer. Harris et al. [1986] carried out a systematic study of the mobility dependence of $Ga_{1-x}Al_xAs$/GaAs heterostructures on the spacer layer thickness. Figure 2.2 shows the mobility for high purity samples, at 4.2 K, as a function of the spacer layer thickness.

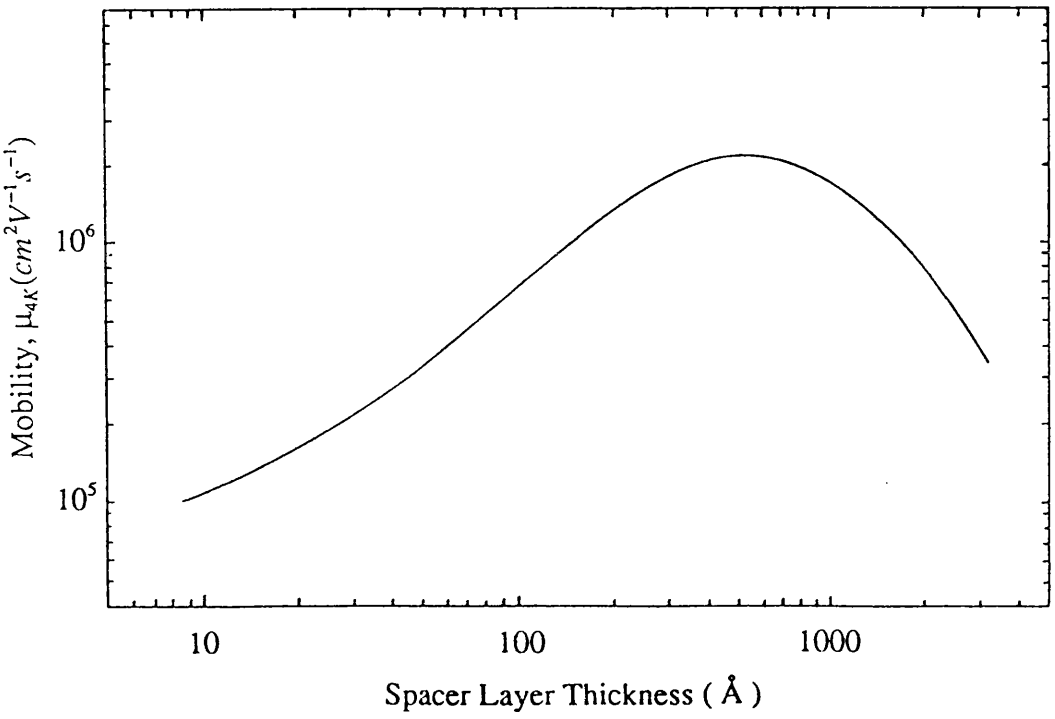

FIGURE 2.2 Mobility as a function of undoped spacer thickness.

The curve can be divided into two regions:

The region with a spacer layer of less than 400 Å shows an increase in mobility with increase in the spacer layer thickness. This derives from the increased separation of the ionised impurities in the doped $Ga_{1-x}Al_xAs$ layer from the two dimensional electron gas.

The region with a spacer layer greater than 800 Å shows a reduction of mobility which is a result of the dependence

of various scattering mechanisms on the two dimensional electron gas density, i.e. ionised impurity and piezoelectric scattering.

The introduction of this spacer layer combined with the improved cleanliness in the molecular beam epitaxy growth process has lead to the production of very high mobility $Ga_{1-x}Al_xAs/GaAs$ heterostructures.

2.2 Electric quantization

The calculation of the electron energy levels in $Ga_{1-x}Al_xAs/GaAs$ heterojunctions have been investigated by several authors [Stern and Das Sarma 1984, Vinter 1984]. This section will initially outline an approximate solution and then briefly describe a more advanced treatment of the problem as carried out by Stern and Das Sarma.

2.2.1 Triangular potential approximation

When considering an electron gas in the presence of an external potential, the spatial electronic distribution is described in general by two equations. The first equation is the Schrödinger equation for the wavefunction, which contains an effective potential. The second equation is the Poisson equation for the potential which contains the wavefunction through the charge density. The two equations

are to be solved together in a self-consistant way. To simplify the problem for this calculation, the effective potential is assumed to be fixed.

In the effective mass approximation for a spherical energy band the Schrödinger equation reads

$$\left[\frac{p^2}{2m^*}+U\right]\Psi=\epsilon\Psi. \qquad 2.1$$

If the potential is one-dimensional, U = U(z), solutions are in the form

$$\Psi=A\exp[ik_x x+ik_y y]\phi(z) \qquad 2.2$$

the Schrödinger equation then reduces to :-

$$\left[\left[\frac{1}{2m^*}\right]p_z^2+U(z)\right]\phi=\epsilon_z\phi \qquad 2.3$$

in which

$$\epsilon_z=\epsilon-\frac{\hbar^2}{2m^*}[k_x^2+k_y^2]. \qquad 2.4$$

The potential at the interface of the two materials is an approximately triangular one dimensional asymmetric well [Stormer 1979]. It is possible to compute the exact energies of the eigenvalue problem [Bastard 1982] for this potential and the results of an advanced application will be discussed

later; however in a simple treatment the semiclassical Wentzel-Kramers-Brillouin approximation [Cassels 1982] may be used. The approximation in its lowest order is given by :-

$$\int_{z_1}^{z_2} p_z dz = h\pi[r + c_1 + c_2] \qquad 2.5$$

where p_z is to be treated as a non-operator and determined from equation 2.3, z_1 and z_2 are turning points of the classical motion, at which $p_z = 0$, and $r = 1,2,..$ is the number of nodes in the wavefunction.

The potential for the asymmetric triangular well is shown schematically in figure 2.3.

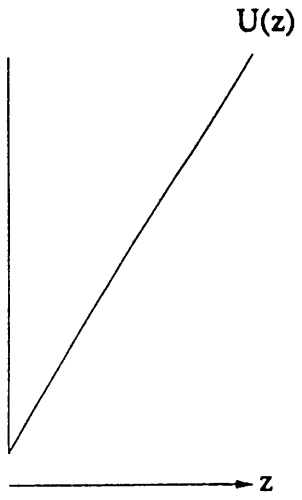

FIGURE 2.3 Potential for an asymmetric triangular well.

The potential is given by:-

$$U(z) = eFz \quad \text{for} \quad z \geq 0 \tag{2.6}$$

$$U(z) = \infty \quad \text{for} \quad z < 0, \tag{2.7}$$

where F is the effective electric field.

In this case c_1 = 1/2 since at the left turning point z_1 = 0 the wavefunction must vanish, and c_2 = 1/4 since at the right turning point $z_2 = \epsilon_z/eF$ this potential is linear.

Equation 2.5 becomes:-

$$[2m^*]^{\frac{1}{2}} \int_0^{z_2} [\epsilon_z - eFz]^{\frac{1}{2}} dz = \hbar\pi \left[r + \frac{3}{4} \right] \tag{2.8}$$

$$r = 0, 1, 2, \ldots$$

Integrating this gives the energy of the r th subband as:-

$$\epsilon_r = \left[\frac{\hbar^2 e^2 F^2}{2m^*} \right]^{\frac{1}{3}} \left[\frac{3\pi}{2} \left[r + \frac{3}{4} \right] \right]^{\frac{2}{3}} \tag{2.9}$$

The exact solutions have the term r + 3/4 in equation 2.9 replaced by 0.7587, 1.7540 and 2.7575 respectively, for the three lowest solutions [Ando et al. 1982]. However the above equation approximates exact eigenvalues up to a fraction of a percent.

2.2.2 Stern and Das Sarmi calculation

Detailed calculations of the energy levels in $Ga_{1-x}Al_xAs/GaAs$ heterojunctions were carried out by Stern and Das Sarma [1984] by solving the Schrödinger equation and the Poisson equation in a self-consistent way. In this calculation the heterojunction effect is modelled using a graded interface in which the barrier height as well as the effective mass and dielectric constant are assumed to change smoothly in a transition layer whose thickness is specified.

Energy levels were calculated for a range of temperatures and material parameters, some of these results are shown in figure 2.4. The calculated values are shown of (a) the energy ϵ_0 of the bottom of the lowest subband and (b) the energy difference ϵ_{10} between the first excited subband and the lowest subband at absolute zero versus channel electron density, N_c, for the six indicated values of net acceptor doping, N_{Ac}, in the GaAs. The corresponding values of N_d, the density of charges in the depletion layer, are 0.146, 0.46, 0.80, 1.47, 2.56 and 4.69×10^{11} cm^{-2} respectively.

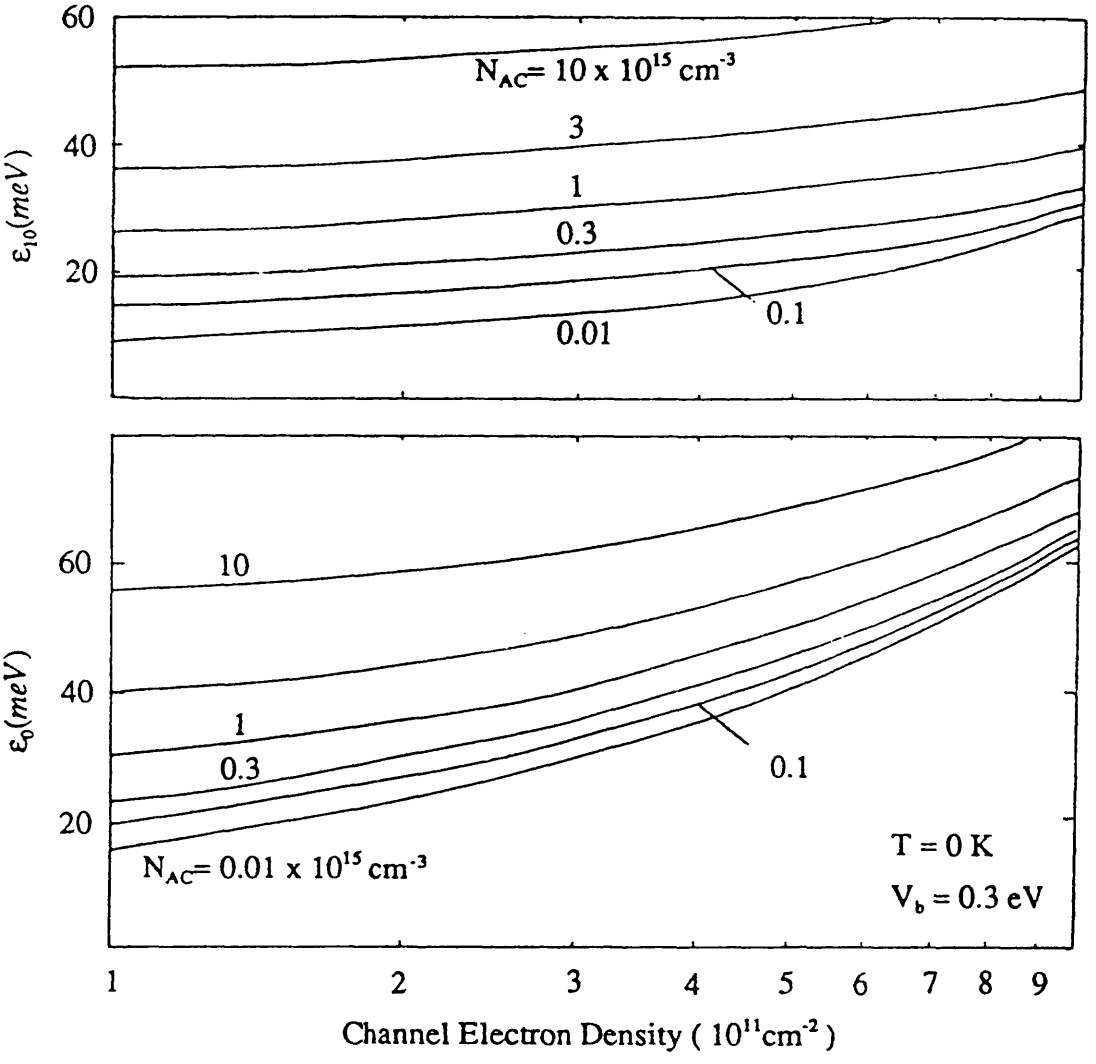

FIGURE 2.4 Calculated values of (a) the energy ϵ_0 of the bottom of the lowest subband and (b) the energy difference ϵ_{10} between the first excited subband and the lowest subband at absolute zero versus channel electron density, N_C, for the six indicated values of net acceptor doping, N_{AC}, in the GaAs. Stern and Das Sarma [1984].

2.3 Magnetic quantization

If a carrier moves in a d.c. magnetic field B at an oblique angle, its motion is an orbit around the direction of the field with an angular frequency known as the cyclotron frequency [Lax 1961] given by

$$\omega_c = eB/m^* \qquad 2.10$$

and a cyclotron radius of

$$r_c = \sqrt{\hbar/[eB]}. \qquad 2.11$$

If $\omega_c \tau_m > 1$ where τ_m is the time between scattering events, then not only will an electron describe complete orbits between scattering events but the electron density of states will also alter. The states fall into allowed energy levels called Landau levels [Landau and Lifshitz 1974] due to the quantization of the orbits of the carriers.

Consider electrons in a two dimensional system in a magnetic field B. The Hamiltonian for the electron is given by

$$H = \frac{1}{2m_0}[\underline{p} - e\underline{A}]^2 + U(z) \qquad 2.12$$

where U(z) is the confining potential which leads to two dimensional behaviour. The operator which represents the electron momentum p is

$$\underline{p} = -i\hbar\nabla \qquad 2.13$$

giving the Schrödinger equation

$$\left[\frac{1}{2m^*}[-i\hbar\nabla - e\underline{A}]^2 + U(z)\right]\Psi = \epsilon\Psi \qquad 2.14$$

where the electron spin has been neglected but the free electron mass has been replaced by the effective mass m^*.

The magnetic field is related to the vector potential $\underline{A}$ through the relationship

$$\underline{B} = \nabla \times \underline{A}. \qquad 2.15$$

The cartesian components of $\underline{A}$

$$\underline{A} = [-yB, 0, 0] \qquad 2.16$$

generate a uniform magnetic field which points in the z direction:-

$$\underline{B} = [0, 0, B]. \qquad 2.17$$

Substituting this value of $\underline{A}$ and knowing from the previous section that U(z) leads to a quantum number defining the subband, and a confinement energy ϵ_z, the Schrödinger equation above becomes

$$[\frac{1}{2m^*}\left[-i\hbar\frac{\partial}{\partial x}+eyB\right]^2-\frac{\hbar^2}{2m^*}\frac{\partial^2}{\partial y^2}]\Psi=[\epsilon-\epsilon_z]\Psi. \qquad 2.18$$

Since the coordinate x is missing from the Hamiltonian it follows that the momentum in the x direction is unaffected by the magnetic field. The eigenstate of the momentum in this direction is given by

$$\Psi_{K_x}=e^{i[k_x x]}. \qquad 2.19$$

The common eigenstates are then written in the form

$$\Psi=e^{i[k_x x]}f(y)\phi(z) \qquad 2.20$$

where $\phi(z)$ comes from the z quantization. Substituting this product into equation 2.18 gives

$$\left[\frac{-\hbar^2}{2m^*}\frac{\partial^2}{\partial y^2}+\frac{e^2B^2}{2m^*}\left[y-\frac{\hbar k_x}{eB}\right]^2\right]f=[\epsilon-\epsilon_z]f. \qquad 2.21$$

Setting

$$\frac{K}{m^*}=\left[\frac{eB}{m^*}\right]^2=\omega_c^2 \qquad 2.22$$

and

$$y_0=\frac{\hbar k_x}{eB} \qquad 2.23$$

gives

$$\left[-\frac{\hbar^2}{2m^*}\frac{\partial^2}{\partial y^2}+\frac{K}{2}[y-y_0]^2\right]f=[\epsilon-\epsilon_z]f. \qquad 2.24$$

The above Schrödinger equation is the same as that for a simple harmonic oscillator [Ziman 1964] constrained to move along the y axis, about a point y_0, with natural frequency ω_c.

The eigenenergies of this equation are given by

$$[\epsilon_n-\epsilon_z]=\hbar\omega_c\left[n+\frac{1}{2}\right] \qquad 2.25$$

which gives the result

$$\epsilon_n=\hbar\omega_c\left[n+\frac{1}{2}\right]+\epsilon_z. \qquad 2.26$$

The kinetic energy term $\hbar\omega_c\left[n+\frac{1}{2}\right]$ relates to the quantization of the energy states in the plane normal to the magnetic field. The energy states form a ladder of Landau levels whose energy separation is given by

$$\hbar\omega_c=\frac{\hbar eB}{m^*}. \qquad 2.27$$

Ideally the levels are perfectly sharp, but in a real system broadening of the levels occur due to the scattering of the carriers.

2.4 Cyclotron resonance theory

Cyclotron resonance is the result of the transition of electrons between the Landau levels of the same energy state. When a free electron is allowed to move in the presence of a magnetic field, it executes a helical path axially about the direction of the magnetic field with the cyclotron frequency. If an alternating electric field is applied perpendicular to the magnetic field, a small oscillatory component is added to the rotational motion of the electron. The electron takes up energy from the electric field by moving into unoccupied states of higher energies. As a result of the previously described quantization of the electron orbits in the plane perpendicular to the magnetic field, the nearest available states have an energy which is higher by $\hbar\omega_c$. Therefore the alternating electric field wave is strongly absorbed if its frequency is made equal to the cyclotron frequency, resulting in the transition of the electrons into a higher Landau level. As in any resonance observation, a peak is not found for the case of strong damping, such as when most carriers make a collision before

rotating at least through one radian. Since the number of collisions per unit time is $1/\tau_m$, the condition for resonance peak is given by

$$\omega_c > \frac{1}{\tau_m} \qquad 2.28$$

This condition poses a severe limit on the observation of microwave cyclotron resonance; τ_m should be larger than about 10^{-10} s. The high mobilities, and therefore large values of τ_m, achieved in $Ga_{1-x}Al_xAs/GaAs$ heterostructures allow cyclotron resonance to be observed at this wavelength.

For a simplified treatment of cyclotron resonance consider the equation of motion of a carrier, in an a.c. electric field and a static magnetic field B, not including an energy distribution of carriers

$$m\left[\frac{d}{dt}+\frac{1}{\tau_m}\right]v_d = e[E+[v_d \times B]]. \qquad 2.29$$

Introducing a Cartesian coordinate system and choosing the direction of B as the z-axis, the equations of motion are

$$m\left[\frac{d}{dt}+\frac{1}{\tau_m}\right]v_x = e[E_x + B_z v_y], \qquad 2.30$$

$$m\left[\frac{d}{dt}+\frac{1}{\tau_m}\right]v_y = e[E_y - B_z v_x], \qquad 2.31$$

$$m\left[\frac{d}{dt}+\frac{1}{\tau_m}\right]v_z = eE_z. \qquad 2.32$$

With

$$E \propto \exp(i\omega t) \qquad 2.33$$

equations 2.30 and 2.31 can be solved simultaneously to obtain

$$v_x = \frac{me[i\omega+\tau_m^{-1}]E_x + B_z e^2 E_y}{m^2[i\omega+\tau_m^{-1}]^2 + B_z^2 e^2}. \qquad 2.34$$

By substituting the conductivity tensor in an orthogonal system:

$$\sigma = \begin{pmatrix} \sigma_{xx} & \sigma_{xy} & 0 \\ \sigma_{yx} & \sigma_{yy} & 0 \\ 0 & 0 & \sigma_{zz} \end{pmatrix} \qquad 2.35$$

into

$$\sigma E = nev_d \qquad 2.36$$

the following is obtained

$$v_x = \frac{1}{ne}\sigma_{xx}E_x + \frac{1}{ne}\sigma_{xy}E_y. \qquad 2.37$$

Comparing equations 2.34 and 2.37

$$\sigma_{xx} = \sigma_{yy} = \sigma_0 \tau_m^{-1} \frac{\tau_m^{-1} + i\omega}{[\tau_m^{-1} + i\omega]^2 + \omega_c^2} \qquad 2.38$$

and

$$\sigma_{xy} = -\sigma_{yx} = \sigma_0 \tau_m^{-1} \frac{\omega_c}{[\tau_m^{-1} + i\omega]^2 + \omega_c^2} \qquad 2.39$$

where the d.c. Conductivity is given by

$$\sigma_0 = \frac{ne^2\tau_m}{m^*}. \qquad 2.40$$

Consider a right-hand polarized field where $E_y = -iE_x$ and introducing σ_+ by

$$\sigma_+ = \frac{j_x}{E_x} = \sigma_{xx} + \sigma_{xy}\frac{E_y}{E_x} \qquad 2.41$$

substituting in equations 2.38 and 2.39 it follows that

$$\sigma_+ = \sigma_0 \tau_m^{-1} \frac{\tau_m^{-1} + i\omega - i\omega_c}{[\tau_m^{-1} + i\omega]^2 + \omega_c^2} = \frac{\sigma_0 \tau_m^{-1}}{\tau_m^{-1} + i[\omega + \omega_c]} \qquad 2.42$$

Similarly, for a left-hand polarization we have

$$\sigma_- = \frac{\sigma_0 \tau_m^{-1}}{\tau_m^{-1} + i[\omega - \omega_c]} \qquad 2.43$$

Considering the Faraday convention [Sanders and Reed 1978], where a transverse electromagnetic wave E is perpendicular to the d.c. magnetic field B, the power absorbed by the carriers is given by

$$P(\omega)=\frac{1}{2}Re\{jE^{*}\} \qquad 2.44$$

where E^{*} is the complex conjugate of E. As

$$j=\sigma E \qquad 2.45$$

it follows that for either polarization we have

$$P_{\pm}=\frac{1}{2}E^{2}Re\left[\frac{\sigma_0\tau_m^{-1}}{\tau_m+[\omega\pm\omega_c]}\right]=\frac{1}{2}E^{2}\frac{\sigma_0\tau_m^{-2}}{\tau_m^{-2}+[\omega\pm\omega_c]^{2}}. \qquad 2.46$$

For a linear polarization which can be considered to be composed of two circular polarizations rotating in opposite directions,

$$P(\omega)=P_{+}+P_{-}=\frac{\sigma_0}{2}E^{2}\left[\frac{1}{1+[\omega+\omega_c]^{2}\tau_m^{2}}+\frac{1}{1+[\omega-\omega_c]^{2}\tau^{2}}\right]$$

$$=\sigma_0E^{2}\frac{1+[\omega^{2}+\omega_c^{2}]\tau_m^{2}}{[1+[\omega^{2}-\omega_c^{2}]\tau_m^{2}]^{2}+4\omega_c^{2}\tau_m^{2}}. \qquad 2.47$$

At cyclotron resonance $\omega=\omega_c$ and assuming $\omega_c\tau_m\gg 1$, this becomes simply

$$P(\omega_c) = \frac{1}{2}\sigma_0 E^{2.} \qquad 2.48$$

For this case the conductivity is equal to the dc conductivity σ_0, while outside the resonance it is smaller than σ_0. Figure 2.5 shows the absorbed microwave power P as a function of cyclotron resonance frequency / signal frequency.

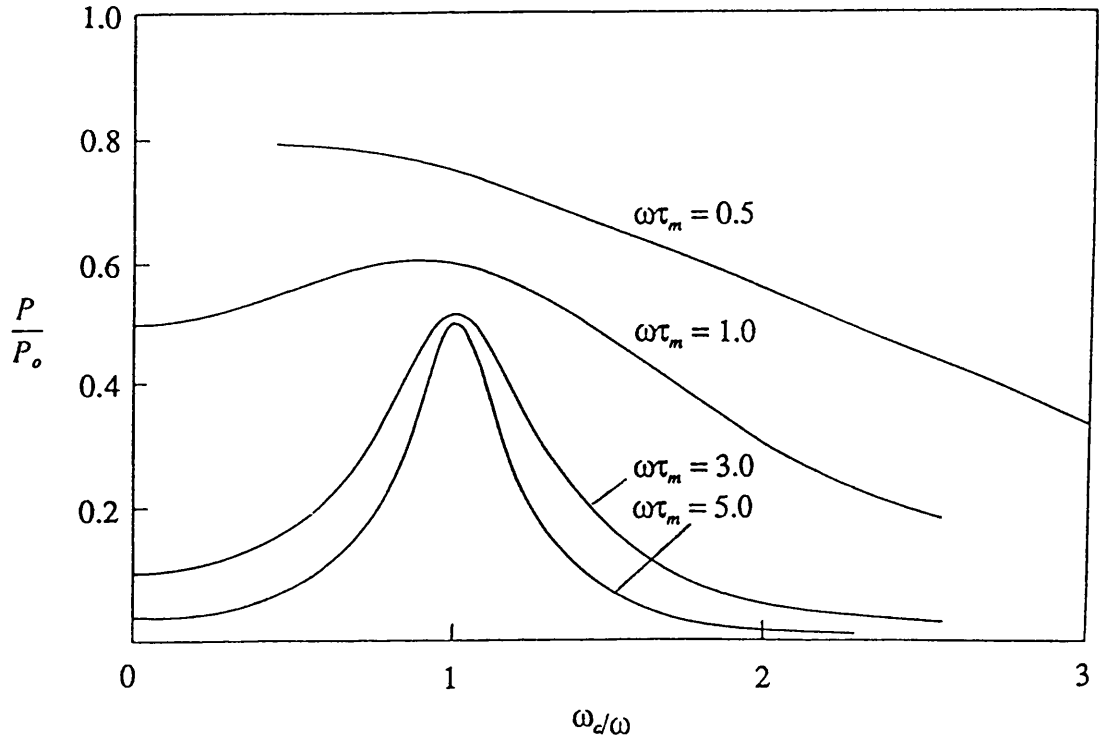

FIGURE 2.5 Absorbed microwave power P as a function of cyclotron resonance frequency / signal frequency.

Measurements of cyclotron resonance on two dimensional systems are carried out with the magnetic field applied normal to the two dimensional plane. The resulting change in the density of states only occurs in the plane normal to the direction of the magnetic field. Consequently the effect is much more pronounced in a two dimensional system as opposed to a three dimensional system, as in the latter the electron motion can still occur in the direction parallel to the magnetic field.

Advanced calculations of the cyclotron resonance lineshape for a two dimensional electron gas system were carried out by Ando [1975]. Figure 2.6 shows the theoretically determined cyclotron resonance line shape in the first Landau level, (a) when the Fermi level lies at the middle point of the first and second Landau level and (b) when it lies at the centre of the first Landau level. Γ is the Landau level width and α is the order of the scattering range divided by the cyclotron radius.

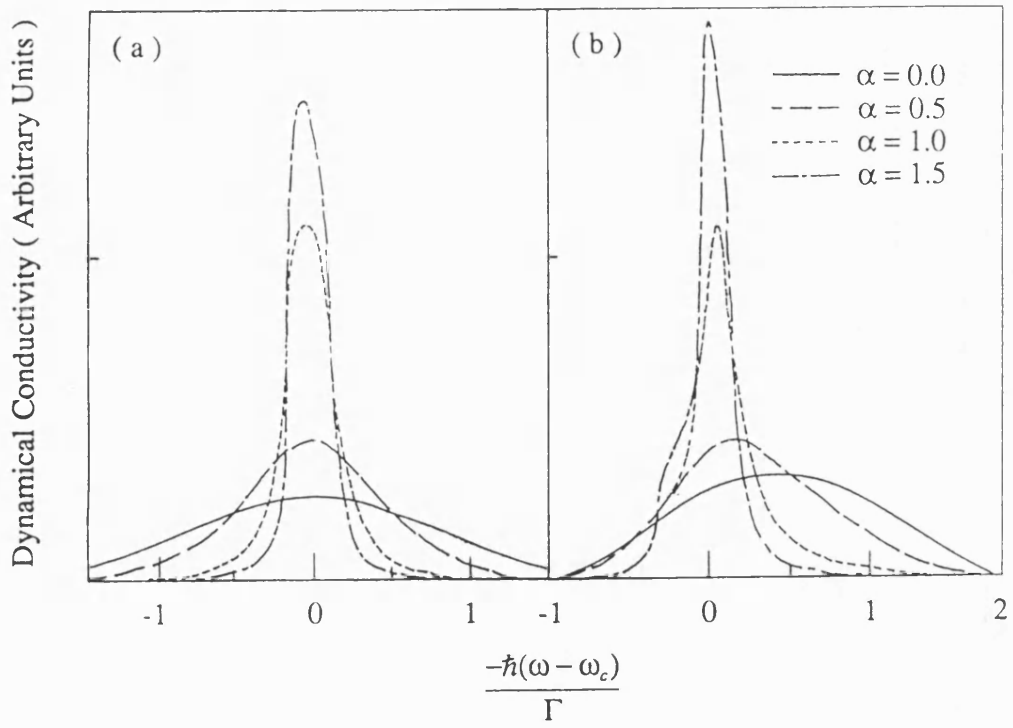

FIGURE 2.6 Dynamical conductivity at zero temperature. (a) The Fermi level lies at the middle point of the first and second Landau level. (b) The Fermi level lies at the centre of the first Landau level. Ando [1975].

When the Fermi level lies in the middle point of two adjacent Landau levels, the lineshape is symmetric around the cyclotron frequency. However, if the Fermi level lies in a certain broadened Landau level, the lineshape is asymmetric. In this situation, and with short-range scatterers, the resonance frequency is shifted to the high frequency side. The frequency shift of short-range scatterers can be

understood by considering the Pauli principle and that the transition between all adjacent states becomes allowed; also that the intensity is determined by the initial and the final density of states. Consider, the case when the Fermi levels lies in the N^{th} Landau level. In Ando's earlier work [Ando and Uemura 1974] he determined that, for scatterers with a finite range, the Landau level width Γ decreased with the increasing order of the Landau level. Therefore, since $\Gamma_{N-1} > \Gamma_N > \Gamma_{N+1}$, the lower frequency side is mainly determined by the transition between the $N - 1^{th}$ and the N^{th} levels, and the high frequency side by that between the N^{th} and the $N + 1^{th}$ levels. Therefore for a comparatively short scattering range the lineshapes due to these two different transitions differ from each other resulting in the appearance of structure in the resonance line.

Figure 2.7 shows the dynamical conductivity as a function of applied magnetic field in an n-channel inversion layer on silicon, for three different carrier concentrations. The solid lines are Ando's calculated results, whereas the broken ones are obtained by the classical formula, given in equation 2.47.

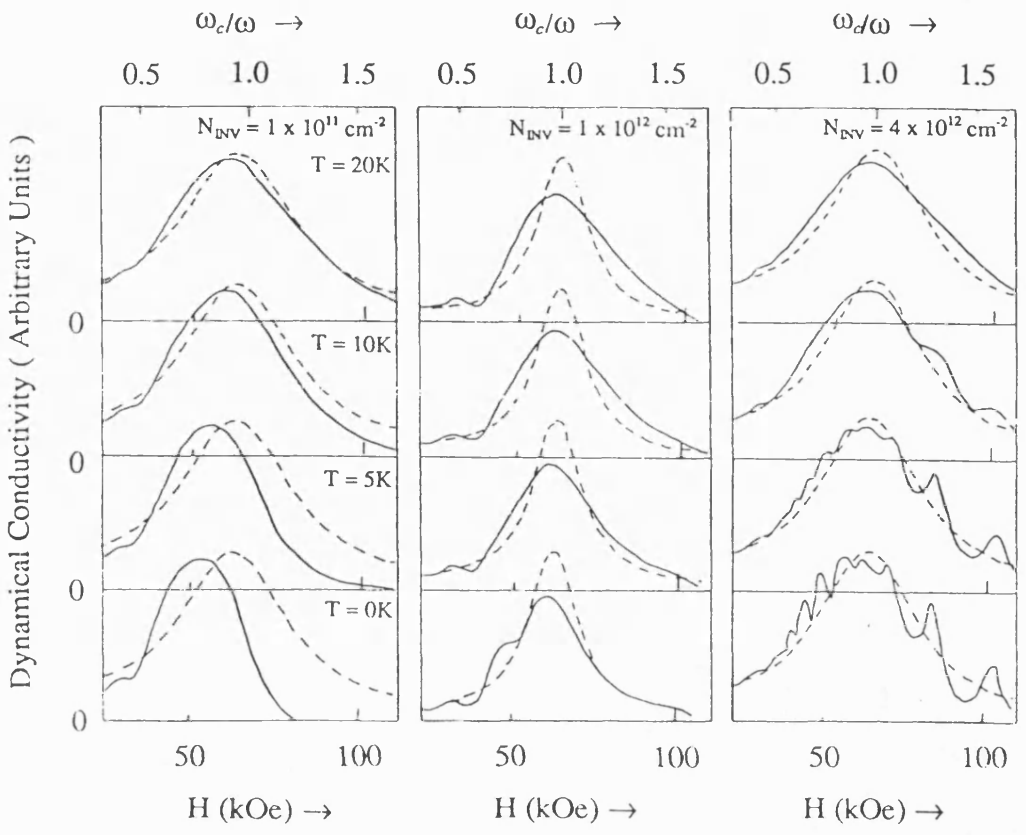

FIGURE 2.7 Dynamical conductivity as a function of applied magnetic field in an n-channal inversion layer on silicon, assuming short range scattering. Ando [1975].

In the case of very low carrier concentrations electrons occupy only the low energy part of the broadened ground Landau levels, and therefore the peak is shifted to the low field side at sufficiently low temperatures.

For higher carrier concentrations, the main features of the two dimensional version of cyclotron resonance are the existence of the oscillatory structure and asymmetry. The appearance of the oscillation is characteristic of the two dimensional system. In three dimensional systems, such oscillation is smeared out by the existence of motion along the magnetic field. These oscillations arise from the quantization of the electron orbits into Landau levels. The oscillation is due to a periodic modulation of resonance strength as the occupation of Landau levels near the Fermi energy varies with magnetic field. The Landau level width is roughly proportional to $B^{1/2}$ [Ando and Uemura 1974] and from figure 2.7 we see that the oscillation becomes larger with increasing level width. The oscillation disappears when k_BT (Boltzmann's constant multiplied by the temperature) becomes the order of the width of each Landau level. Since the level width is roughly proportional to $B^{1/2}$ the lineshape becomes asymmetric and has a larger tail in the high magnetic field side. Ando compared these calculations to experimentation by Abstreiter et al [1976] on surface resonance in silicon inversion layers. The theory gave a good account of the experimental observation as shown in figure 2.8.

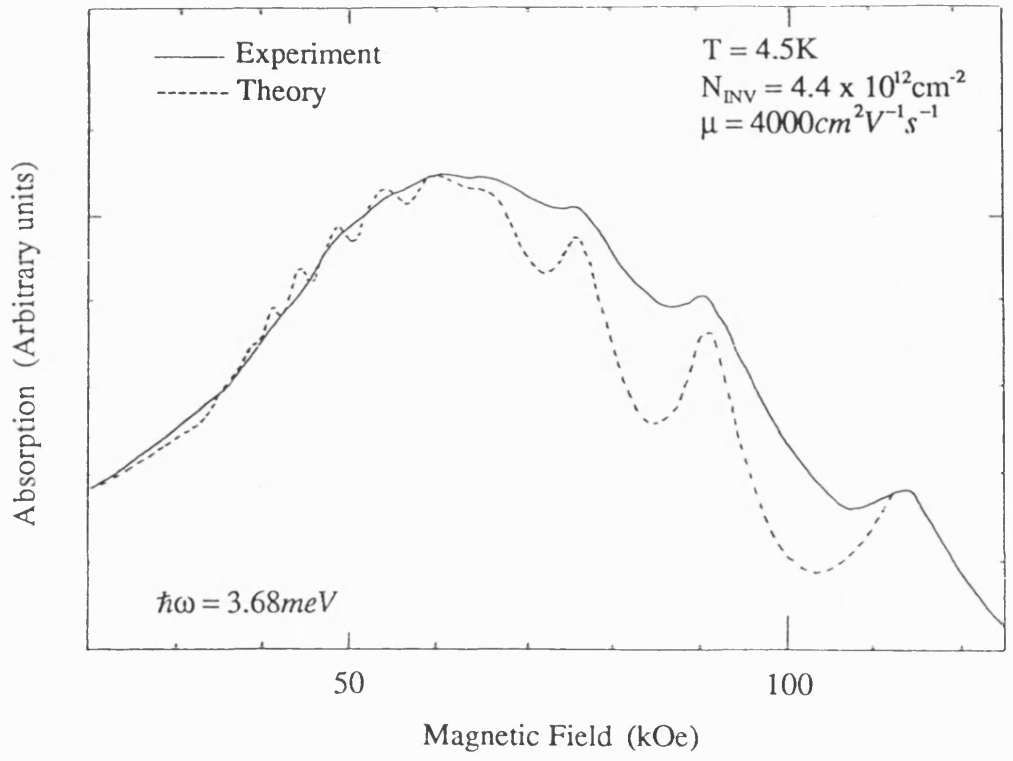

FIGURE 2.8 Cyclotron resonance observed by Abstreiter et al. [1976] (solid line) and theoretical lineshape calculated by Ando et al. [1975] (dashed line).

Koch [1975] also compared experimental results obtained from silicon inversion layers with both the classical lineshape given by equation 2.47 and Ando's theory as shown in figure 2.9.

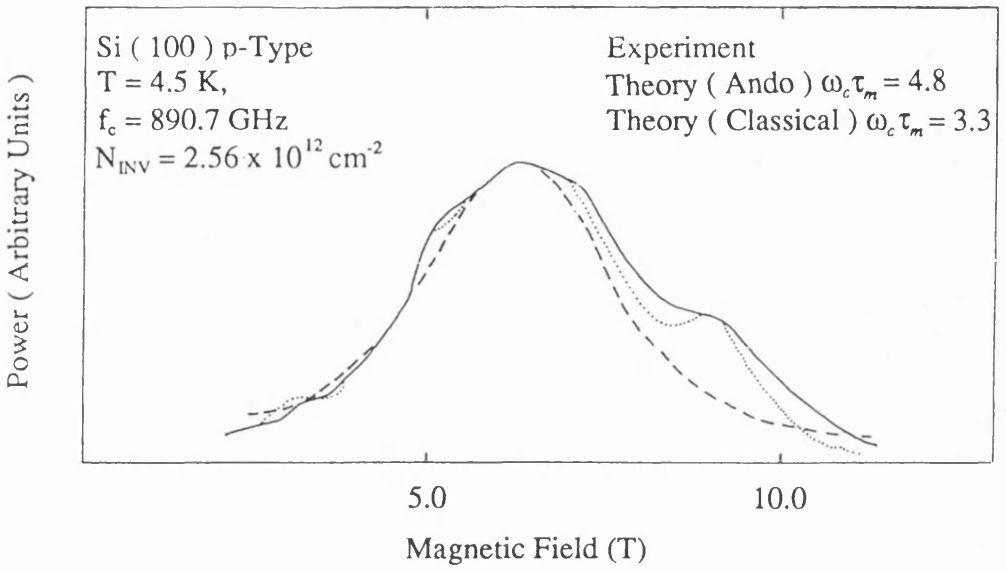

FIGURE 2.9 Cyclotron resonance lineshape observed in the surface inversion layer of silicon by Koch [1975], compared with the theoretical lineshape calculated by Ando et al. [1975] (dashed line). The classical lineshape has also been included.

Figure 2.9 shows the agreement obtained particularly in the asymmetry and oscillatory structure observed.

2.5 Cyclotron resonance measurement techniques

Cyclotron resonance measurements can be carried out using either optical transmission or photoconductivity.

2.5.1 Optical transmission measurements

The first measurements of cyclotron resonance in a $Ga_{1-x}Al_xAs/GaAs$ heterostructure were made by Stormer et al [1979] using optical transmission. An optically pumped laser was used to produce a 1840 GHz signal. The resulting power absorption in the sample was recorded using two photodetectors. The overall shape of the resonance was then fitted to the derivative of the classical expression given by equation 2.47, which yielded $\omega\tau_m = 2.4$. The authors also observed quantum oscillations at the high side of the field which had been predicted previously by Ando [1985] in silicon space charge layers and are unique to two dimensional systems.

2.5.2 Initial photoconductivity measurements

The first clear cyclotron resonance in the photoconductive response of a $Ga_{1-x}Al_xAs/GaAs$ heterostructure was reported by Maan et al. [1982]. The cyclotron resonance was seen in the far infra-red using a 96 μm laser signal and is shown in figure 2.10. Two effects were considered to explain the physical origins of the observed resonance. The first was the heating of the sample at resonance conditions in which case the signal simply reflected the temperature dependence of the resistance. However the sample was at liquid helium temperature and a more quantitative account

could not be given. The second is that of a change of resistance due to the redistribution of the carriers between Landau levels.

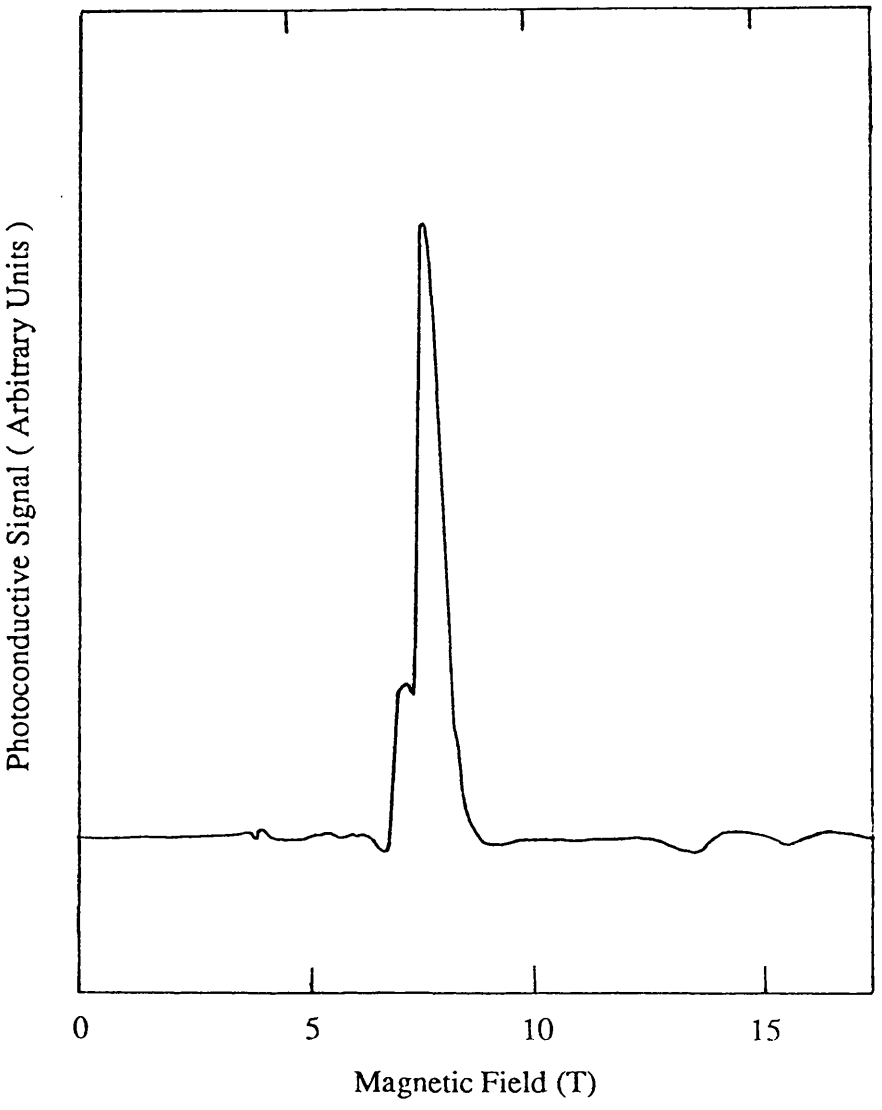

FIGURE 2.10 Photoresponse as a function of the magnetic field for $\lambda = 96\mu m$ at 4.2K with a 10 μA bias current. Maan et al. [1982].

The influence of a magnetic field upon the density of states of a two dimensional system is shown in figure 2.11.

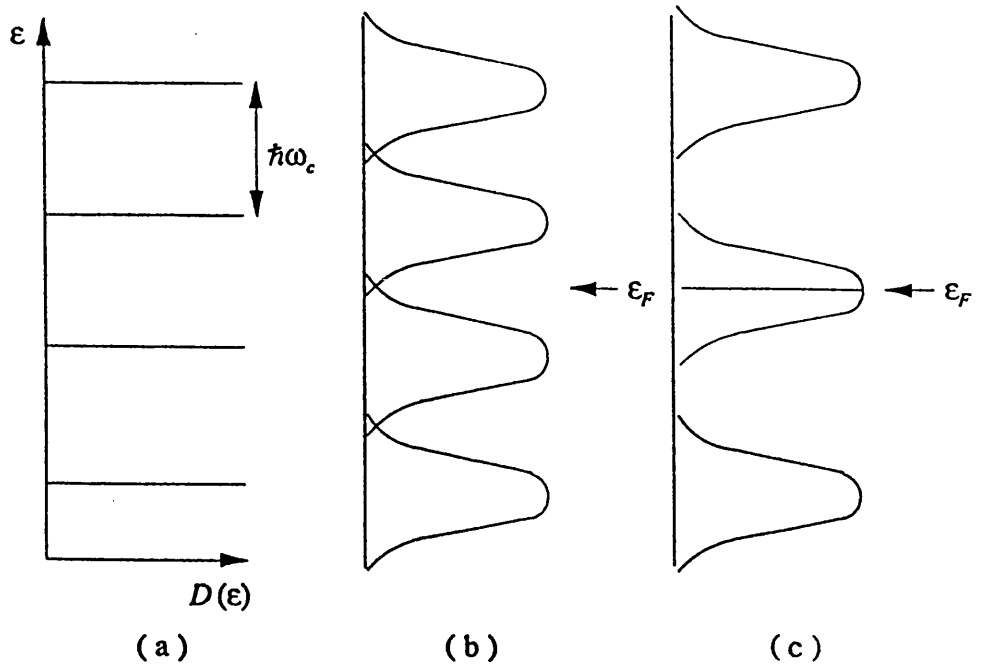

FIGURE 2.11 Landau levels (a) in a two dimensional system in the absence of scattering. (b) where a Landau level is just completely filled. (c) with a half filled uppermost Landau level.

Figure 2.11(a) shows the formation of the Landau level in the absence of scattering to be a set of delta functions. Figure 2.11(b) and figure 2.11(c) shows the Landau levels formed due to two different magnetic fields, including the broadening of the levels due to the scattering of the carriers. Figure 2.11(b) shows that for a certain magnetic

field, the situation arises where the Landau level becomes completely filled and the next higher one separated is completely empty. There is a vanishing of resistance due to the fact that no interlevel scattering is allowed in this situation. The presence of far infra-red radiation changes this situation drastically because both the photoexcited carriers in the higher Landau level and the empty states left behind in the lower Landau level increase scattering and a strong increase in the resistivity is expected. On increasing the magnetic field, the situation shown in figure 2.11(c) is reached, where the Fermi level lies in the middle of a Landau level. This level will be only half full of carriers and therefore a much weaker relative change of resistance may be expected.

Either mechanism, heating or carrier redistributions, qualitatively described the observed magnitude and sign of the photoconductive signal.

Figure 2.11 also explains the effect known as Shubnikov de Haas oscillations [Nicholas 1987]. It can be seen that changing the magnetic field sweeps the Landau levels through the Fermi level. It is this that causes the oscillations in magnetoresistance known as the Shubnikov de Haas effect. A vanishing of resistance occurs each time the Fermi level lies between the Landau levels, i.e. a Landau level is full. The effect may similarly be achieved by increasing the

carrier density, and consequently sweeping the Fermi level through the Landau levels. The period of these oscillations with increasing magnetic field can be used to calculate the carrier concentration. The degeneracy of the levels, per unit area, is given by

$$n_L = \frac{eB}{h} \qquad 2.49$$

Therefore if the carrier concentration is N_C, the oscillation will have a period of

$$N_c = N\frac{2eB_N}{h} \qquad 2.50$$

Where N is an integer, and a factor of two is included for the spin degeneracy.

2.5.3 Photoconductivity due to the hot electron effect

Horstman et al. [1984] carried out the first quantitative comparison between infrared transmission and photoconductivity cyclotron resonance measurements based on the assumption that the far-infrared absorption in the first order leads to a temperature increase of the electron gas. A set of measurements were made to verify this assumption. These are shown in figure 2.12.

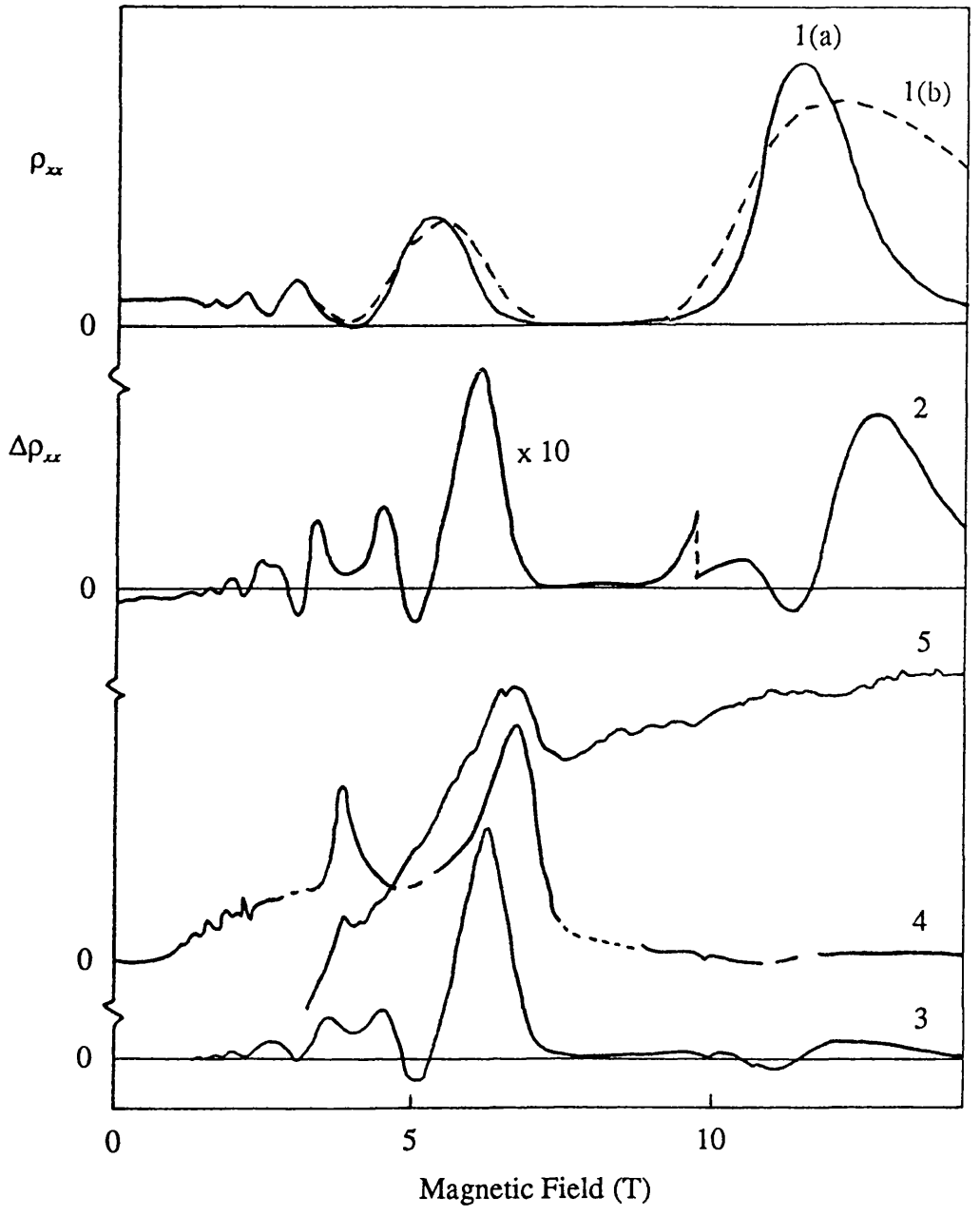

FIGURE 2.12 Experimental results to determine mechanism of photoconductive detection of cyclotron resonance. Horstman et al. [1984].

The following reasoning was given. When far-infrared radiation is absorbed by the electrons the equilibrium distribution is changed, since the electrons are excited from one Landau level to the next higher level. After some time the electrons relax either by photon or by phonon emission. The phonons can be absorbed and lead to an energy redistribution of the electrons. At excitation rates which are low in respect to the relaxation time of the electrons, the energy distribution is assumed to be approximated by a Fermi function at an increased temperature. The temperature increase results in a change in the conductivity.

Initially the temperature coefficient of the conductivity was obtained by measuring the magneto resistance ρ_{xx} at 1.5 K (trace 1a) and 4.2 K (trace 1b) as function of magnetic field. The difference in resistivity ρ_{xx} between the two traces is shown in trace 2. Next the far-infra red laser was switched on at the lowest of these bath temperatures and the resistance measured again. The data with and without the laser irradiation at that temperature was then subtracted from each other. Trace 3 shows the change in resistivity due to the far infrared radiation. This was then divided by the previously measured temperature coefficient (trace 2) to obtain trace 4 that represents the temperature increase of the sample due to the laser irradiation. Dotted parts of trace 4 indicate the regions where the analysis becomes less accurate ($\Delta\rho_{xx}$ close to zero) For $\Delta\rho_{xx} = 0$

the analysis is not carried out and the trace is interrupted. Finally trace 5 shows the absorbed infrared radiation obtained for the laser.

The cyclotron resonance line in the photoconductivity data as measured had quite a different shape and position compared to the cyclotron resonance observed in the transmitted light signal. After analyzing the photoconductivity data as described, both the cyclotron resonance lines in transmission and deduced from photoconductivity have the same position within experimental error, although the former of these had a slightly broader peak size. Therefore the assumption that far-infrared absorption in the first order leads to a temperature increase of the electron gas was taken to be correct. The difference in width was attributed to the difference in scattering time between localized and non-localised electrons as the former do not contribute to the conductivity.

The signal is attributed to a change in the samples resistivity, due to resonant absorption heating. With the absorption of energy, the electron temperature rises by ΔT_{el} relative to the lattice. In the coupled system of electrons and lattice there is also an increase ΔT_{lat} of the sample above the thermal bath.

Consider the detector and thermal background to consist of three coupled parts. The two dimensional electron gas, the GaAs lattice and the helium bath. Cyclotron resonance involves the absorption of power P. In a primary step the energy of perpendicular motion of electrons increases by $\hbar\omega_c$. A scattering process then takes place in which the excitation energy is transformed or transferred. The hot electron is expected to distribute its energy via electron-electron scattering processes. If the equilibrium among the electrons predominates over the direct losses to the lattice, the electrons can be considered to be heated to a temperature ΔT_{el} above the lattice. The hot electron distribution in turn will relax to the lattice temperature in a time τ_q. The energy flow to the lattice results in a temperature rise ΔT_{lat} of the lattice relative to the bath at T_0. ΔT_{lat} depends on the thermal coupling of the sample to its surrounding. The relaxation time for this energy transfer is define as τ_0. In a system in which the sample has good thermal coupling to its helium surroundings, so that $\tau_q >> \tau_0$, the electron temperature will rise above the lattice temperature which will remain approximately that of its surroundings.

The electrons gain energy from the absorption of electromagnetic radiation at the cyclotron resonance frequency. A steady state is reached where the rate of gain in electron

energy from the radiation is equal to the rate of energy loss by collisions. Therefore a power balance condition is satisfied in which

$$\frac{\epsilon(T_e)-\epsilon(T_L)}{\tau_q} \approx \frac{C_{el}(T_e-T_L)}{2\tau_q} = P_e \qquad 2.51$$

where C_{el} is the specific heat capacity of the electrons, T_L is the lattice temperature and P_e the input power per electron.

The electronic heat capacity of a two dimensional electron gas can be derived in the following way.

The increase U_e in the total energy of a system of N_e electrons when heated from 0 to T is

$$U_e = \int_0^{\infty} \epsilon D(\epsilon) f(\epsilon) d\epsilon - \int_0^{\epsilon_F} \epsilon D(\epsilon) d\epsilon \qquad 2.52$$

where $f(\epsilon)$ is the Fermi-Dirac function [Kittel 1976] which gives the probability that a state at energy ϵ will be occupied in thermal equilibrium. $D(\epsilon)$ is the number of states per unit energy range, called the density of states.

Multiplying the number of particles

$$N_e = \int_0^{\infty} D(\epsilon) f(\epsilon) d\epsilon \qquad 2.53$$

by the Fermi energy ϵ_F gives the expression

$$\epsilon_F N_e = \epsilon_F \int_0^\infty D(\epsilon) f(\epsilon) \qquad 2.54$$

which is independent of temperature. Differentiating equations 2.52 and 2.54 gives

$$C_{el} = \frac{\partial U_e}{\partial T} = \int_0^\infty \epsilon D(\epsilon) \frac{\partial f}{\partial T} d\epsilon \qquad 2.55$$

$$0 = \epsilon_F \frac{\partial N_e}{\partial T} = \int_0^\infty \epsilon_F D(\epsilon) \frac{\partial f}{\partial T} d\epsilon. \qquad 2.56$$

Subtracting the second line from the first gives the electronic heat capacity in the form

$$C_{el} = \int_0^\infty (\epsilon - \epsilon_F) D(\epsilon) \frac{\partial f}{\partial T} d\epsilon. \qquad 2.57$$

At low temperatures, $\left(\frac{k_B T}{\epsilon_F} < 0.01\right)$ the derivative $\frac{\partial f}{\partial T}$ is large only at energies near ϵ_F, so $D(\epsilon)$ can be evaluated at ϵ_F and be taken outside of the integrand:

$$C_{el} \approx D(\epsilon_F) \int_0^\infty (\epsilon - \epsilon_F) \frac{\partial f}{\partial T} d\epsilon. \qquad 2.58$$

The Fermi-Dirac distribution is given by

$$f(\epsilon) = \frac{1}{e^{\frac{(\epsilon-\mu)}{k_B T}} + 1}. \qquad 2.59$$

The quantity μ is called the chemical potential. It is a function of temperature chosen for a particular problem in such a way that the total number of particles in the system comes out to be N_e. At absolute zero μ is equal to the Fermi energy because in the limit $T \to 0$ the function changes discontinuously from the value 1 (filled) to the value 0 (empty) at $\epsilon = \epsilon_F = \mu$. Therefore by restricting the derivation to low temperatures the chemical potential can be replaced in equation 2.59 by the Fermi energy ϵ_F. Then

$$\frac{\partial f}{\partial T} = \frac{\epsilon - \epsilon_F}{k_B T^2} \cdot \frac{e^{\frac{(\epsilon-\epsilon_F)}{k_B T}}}{\left[e^{\frac{(\epsilon-\epsilon_F)}{k_B T}} + 1 \right]^2}. \qquad 2.60$$

Inserting this value into equation 2.58 and integrating gives

$$C_{el} = \frac{1}{3}\pi^2 D(\epsilon_F) k_B^2 T. \qquad 2.61$$

The density of states $D(\epsilon_F)$ at the Fermi energy for a two dimensional electron gas can be calculated in the following way.

In the ground state of a system of N_e electrons the occupied states may be represented as points inside a circle in k space. The energy at the edge of the circle is the Fermi energy. The wavevectors at the Fermi surface have a magnitude k_F such that

$$\epsilon_F = \frac{\hbar^2}{2m^*} k_F^2. \qquad 2.62$$

From solving Schrödinger's equation for a two dimensional electron gas confined to a square of edge L, it is deduced that components of the wavevector k must satisfy

$$k = 0; \pm\frac{2\pi}{L}; \pm\frac{4\pi}{L}. \qquad 2.63$$

That is, any component of k is of the form $2n\pi/L$, where n is a positive or negative integer. Therefore there is one allowed wavevector for a area element $(2\pi/L)^2$ of k space. Thus in a circle of area πk_F^2, the total number of states is

$$N_s = 2.\frac{\pi k_F^2}{\left(\frac{2\pi}{L}\right)^2} = \frac{k_F^2 A}{2\pi} \qquad 2.64$$

where the factor 2 comes from the two allowed values of the spin quantum number. The expression for the number of states at the Fermi energy, per unit area is given by

$$D(\epsilon_F) = \frac{dN_s}{d\epsilon} = \frac{m}{\hbar^2 \pi}. \qquad 2.65$$

Substituting this expression into equation 2.61 gives the electronic heat capacity of a two dimensional electron gas as

$$C_{el} = \frac{1}{3}\frac{\pi m^* k_B^2 T}{\hbar^2} \qquad 2.66$$

which can be expressed as

$$C_e = \frac{\pi^2 k_B^2 T}{3\epsilon_F}. \qquad 2.67$$

The power balance equation therefore becomes

$$\frac{\pi^2 k_B^2}{6\epsilon_F} \cdot \frac{T_e^2 - T_L^2}{\tau_q} = P_e. \qquad 2.68$$

The above equation indicates that the rise in the electron temperature is uniquely determined by the product $P_e \tau_q \epsilon_F$. Sakaki et al. [1984] measured the increase in electron temperature caused by an applied electric field for several $Ga_{1-x}Al_xAs/GaAs$ heterojunctions, within a low magnetic field range (< 3 T). The curve in figure 2.13, shows the measured value of the electron temperature as a function of the input power per electron plotted for these samples.

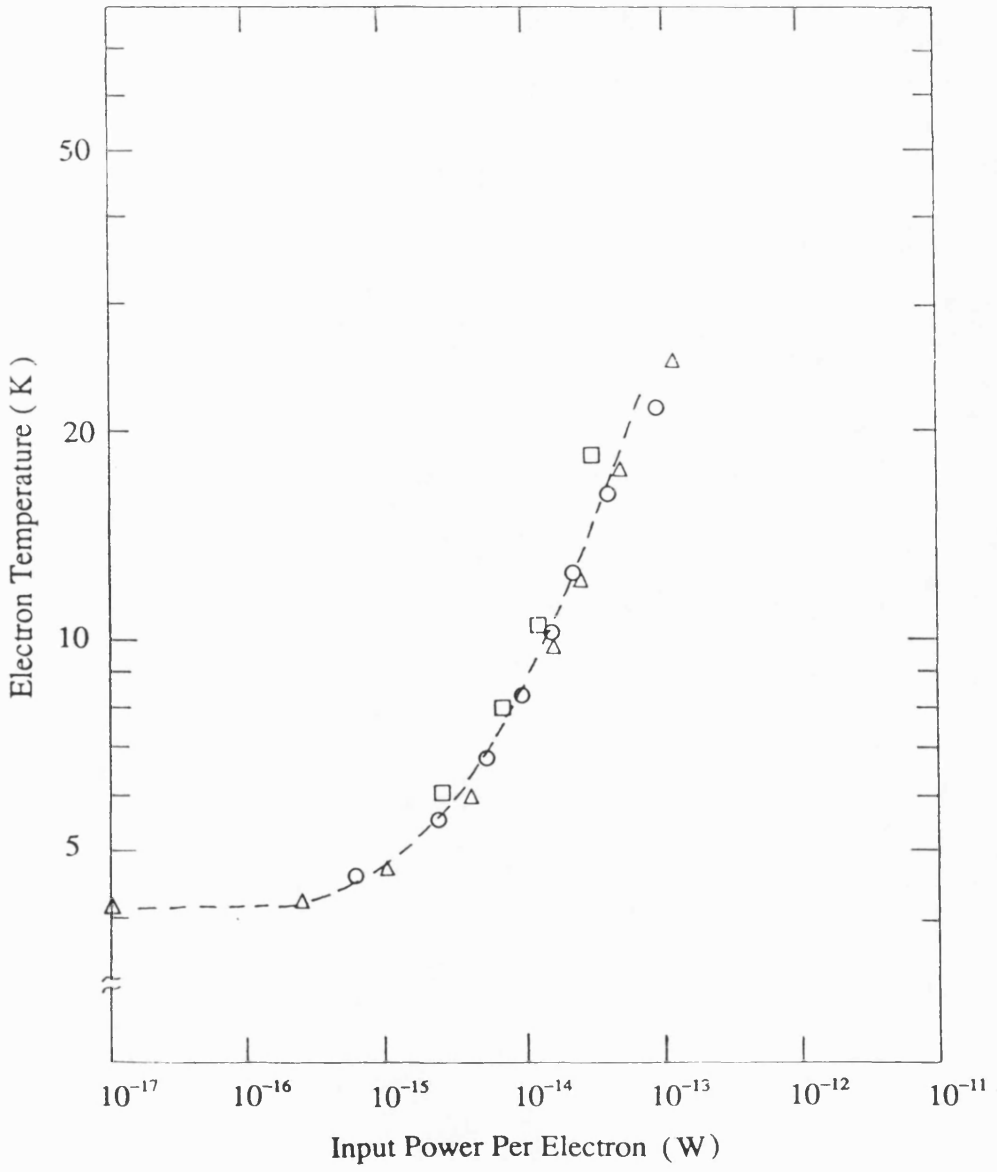

FIGURE 2.13 Electron temperatures determined for three different samples (indicated by different symbols) from the damping of Shubnikov de Haas oscillations. Sakaki et al. [1984].

When the two dimensional gas is heated appreciably by an applied electric field, the thermal equilibrium between the electron system and the phonon system collapses. The result of such heating can be approximately described by one parameter, the electron temperature. Since the increase in electron temperature leads to the damping of the Shubnikov de Haas oscillations, the electron temperature could be deduced from the field dependence of Shubnikov de Haas oscillations.

It was noted that the experimental data for the three samples studied fell on a single curve, although the electron concentrations and the mobilities differed widely from sample to sample. They concluded from this that a dominant cooling process is independent of the mobility and that the electron energy relaxation time is approximately proportional to the inverse of the Fermi energy and hence to the electron concentration.

For the three dimensional system, by contrast, Blussen et al. [1984] showed that the mechanism of photoconductivity originates from the change in carrier density due to cyclotron resonant absorption. In the absence of far infrared radiation equilibrium exists between electrons in donor states and electrons in the N = 0 Landau level, assuming that carriers present in the N = 1 Landau level due to thermal excitation can be neglected. The far infrared absorption creates

carriers in N = 1, at the expense of carriers in N = 0. However thermal re-equilibrium will tend to replenish the population of carriers in the N=0 level. A steady-state distribution among Landau and donor levels develops resulting in an increase in the carrier density. The mobility was found to be independent of the Landau level.

2.5.4 Photoconductivity due to thermal and electronic processes

Two effects are now thought to contribute to the photo-conductive cyclotron resonance signal obtained from $Ga_{1-x}Al_xAs$/GaAs heterojunctions. Firstly a slow bolometric effect and secondly a faster response due to an electronic process.

The existence of fast and slow temporal components in the cyclotron resonance photoresponse was first identified by Stein et al. [1984]. The signal with a time constant of more than 10 ms was attributed to a modulation of the lattice temperature, and therefore basically a bolometric response. The fast response was taken to originate from an electronic process which leads to a change in the electron distribution function.

Chou et al. [1987] have investigated the photoconductivity of high mobility two dimensional electron gases in $Ga_{1-x}Al_xAs$/GaAs heterostructures, at high and low magnetic

fields. When the cyclotron resonance was observed in the integral quantum Hall regime, i.e. B > 3 T, a sharp resonance was observed with no background oscillations. The signal had a fast component with a decay time < 10 μs and a slow component with a decay time of around 1 ms. These were separated by pulse measurements. The slow component could be explained in terms of a simple heating model, whereas the fast component could not be satisfactorily accounted for by the change in resistivity ρ_{xx} due to an increase in the electron temperature above the lattice in the entire range of magnetic field. Chou concluded that the cyclotron resonance corresponded to an increase in the resistivity ρ_{xx}, which would not be expected from a simple heating model. This is in contradiction to the previous findings of Horstmann et al. [1985] for low mobility material.

Figure 2.14 shows the photoresponse of the cyclotron resonance observed in the classical magneto-transport regime < 2 T. Once again the slow component can be well described by the lattice heating. The fast component shows an enhancement of the heat induced quantum oscillations at the cyclotron resonance superimposed on a background which is the cyclotron resonance.

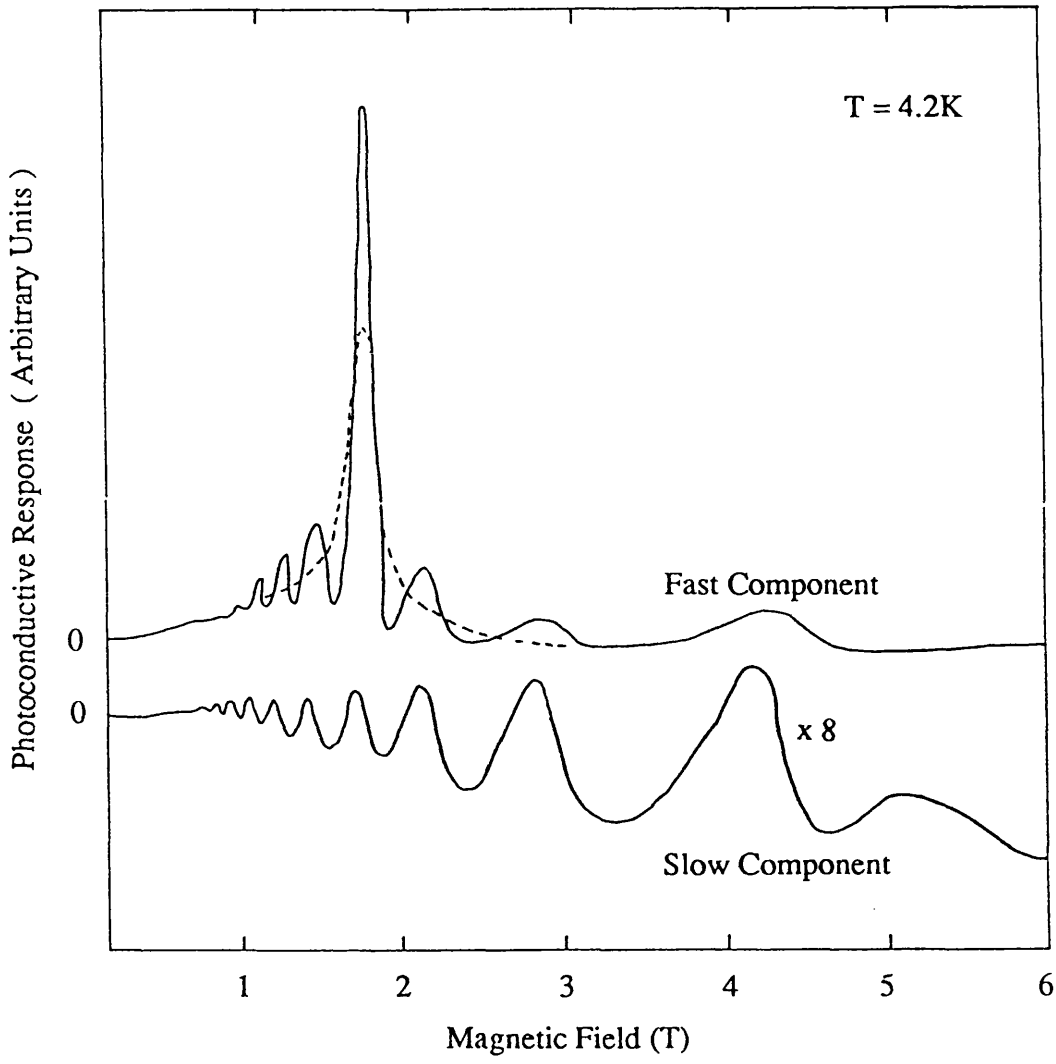

FIGURE 2.14 Photoresponse at magnetic fields < 2T. The upper and lower traces are the fast and slow components respectively. The dashed curve is the background drawn through the half way points of the oscillations. Chou et al. [1987].

Recently Rikken et al. [1988] confirmed that, in addition to the slow bolometric response observed in low mobility samples as found by Horstmann et al, a fast cyclotron resonance photoconductive response can be found in high mobility heterojunctions. The fast response was visible as an increase in the resistivity. This response was attributed to the presence, under photoexcitation, of filled states far above the Fermi level and empty states below it. Both of these provide extra, dissipative scattering channels which manifest themselves as an increase in the resistivity.

2.6 Inter-Landau level lifetimes

Both transmission and photoconductivity measurements have recently been carried out to try to determine the inter-Landau level lifetime in $Ga_{1-x}Al_xAs/GaAs$ heterostructures.

Transmission measurements are being carried out by investigating the intensity dependence of pulsed cyclotron resonance. Helm et al. [1985] performed cyclotron resonance absorption saturation measurements, using a quasi continuous wave far infrared laser, which were then described using a three level model. By comparison with the experimental data the inter-Landau level lifetime could be deduced. Lifetimes were found to vary from 0.18 ns to 1.2 ns for samples of different electron concentration, thus indicating the influence of electron-electron scattering in the relaxation time.

Rikken et al. [1988] carried out a comparison between the time resolved decay of a photosignal from the $Ga_{1-x}Al_xAs/GaAs$ heterostructure sample and from a detector measuring its transmission cyclotron resonance, after the cessation of a far infrared laser pulse.

Figure 2.15 shows the time resolved decay of the germanium detector signal, when measuring the transmission cyclotron resonance.

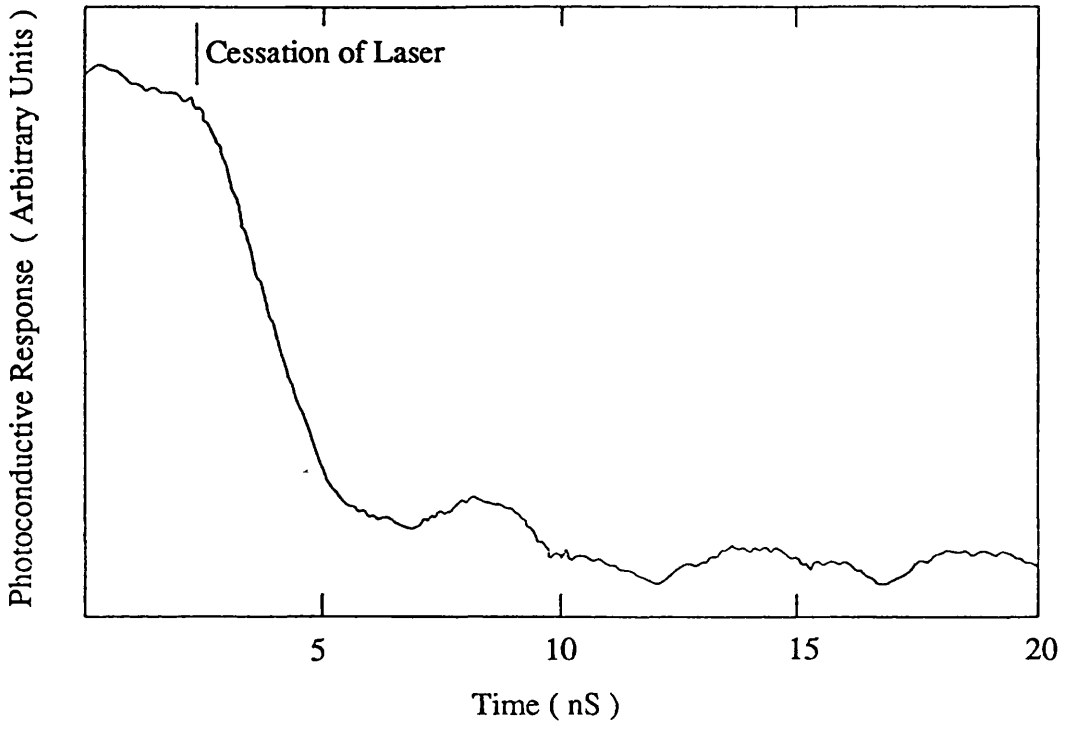

FIGURE 2.15 Time resolved decay of the transmission cyclotron resonance signal for sample at 2 K. Rikken et al. [1988].

The time constant found was that of the detector itself. This was taken to imply that the decay of the photo-excited electron distribution was faster than 3ns. Figure 2.16 shows the time resolved decay of the cyclotron resonance signal after the cessation of the laser pulse.

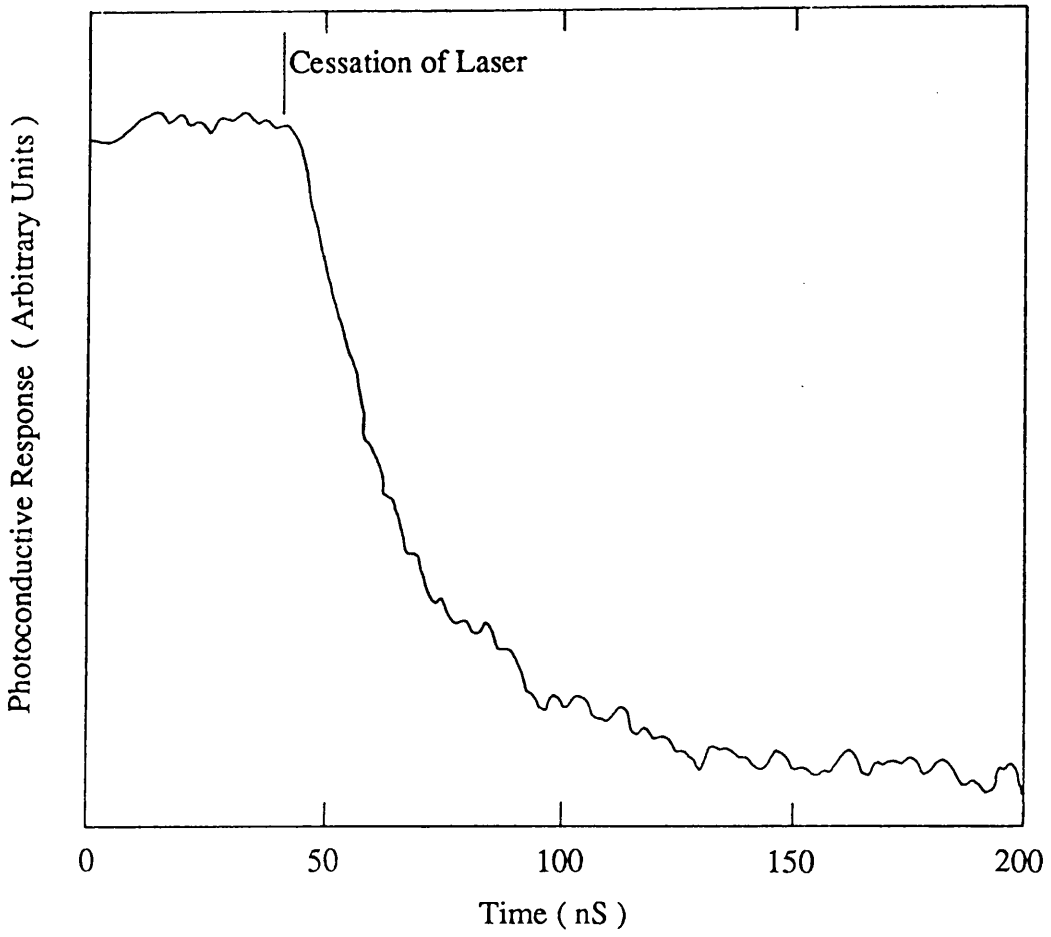

FIGURE 2.16 Time resolved decay of the photoconductive cyclotron resonance signal for sample at 2 K. Rikken et al. [1988].

This data was taken under the same experimental conditions as those in the previous figure. The resulting curve is approximately exponential with a characteristic time of 20ns.

Sarma et al. [1985] have noted that the relaxation time observed in transmission cyclotron resonance measurements should be smaller than that observed when measuring conductivity. This is due to the relative magnitudes of the two different characteristic times involved in transport theory; these are the classical momentum scattering lifetime τ_m and the quantum scattering lifetime τ_q.

The momentum scattering time is derived from classical transport expressions assuming the relaxation time approximation.

When the simplified Boltzmann equation is solved in the relaxation-time approximation, the mean time between collisions is weighted by a factor of $(1-\cos\theta)$ as in the equation

$$\frac{1}{\tau_m} = \int dk' W_{k',k}(1-\cos\theta) \qquad 2.69$$

where $W_{k',k}$ is the probability of scattering from one state k to k' and θ is the scattering angle.

The relaxation-time approximation favours large angle scattering over small angle scattering due to the weighting factor $(1-\cos\theta)$ in equation 2.69. Thus, if the relaxation time is assumed in systems where small angle scattering dominates, the transport scattering time represents only a fraction of the actual number of collisions.

The d.c. Conductivity is related directly to the momentum scattering time by

$$\sigma = \frac{ne\tau_m^2}{m^*} \qquad 2.70$$

Various methods, including magnetoresistance and magneto-conductance measurements, exist to obtain the momentum scattering time τ_m from transport in a magnetic field.

The quantum scattering time parameter, τ_q, is the measure of the broadening of the Landau levels from collisions. It is related to collision broadening in Landau levels by

$$\Gamma = \frac{\hbar}{2\tau_q}. \qquad 2.71$$

The relaxation time parameter in this expression effectively measures the entire collision cross section. Small and large angle scattering events are counted equally, replacing the $(1-\cos\theta)$ term in equation 2.69 with the term (1).

The Shubnikov de Haas oscillatory conductivity reflects the shape of the collision broadened Landau levels, and can thus be used to measure the value of τ_q [Fang 1988].

The momentum and quantum scattering time are equal for short range scattering, for which the scattering cross section is independent of angle and for which the average value of $\cos\theta$ vanishes. However, if the scattering is strongly peaked in the forward direction, τ_m can be considerably greater than τ_q.

Sarma showed that although the quantitative difference between these two times is very small for low mobility heterojunctions, it becomes substantially greater for high mobility heterojunctions. For heterojunctions, where the electrons are confined to a plane and the scatterers lie in a plane parallel to that of the electrons, the distance between the two, z, is an additional parameter characterising the scattering. Figure 2.17 shows the calculated ratio of the momentum scattering time τ_m to the quantum scattering time τ_q in a two dimensional electron gas, with six different values of separation z between the electron layer and the impurity layer.

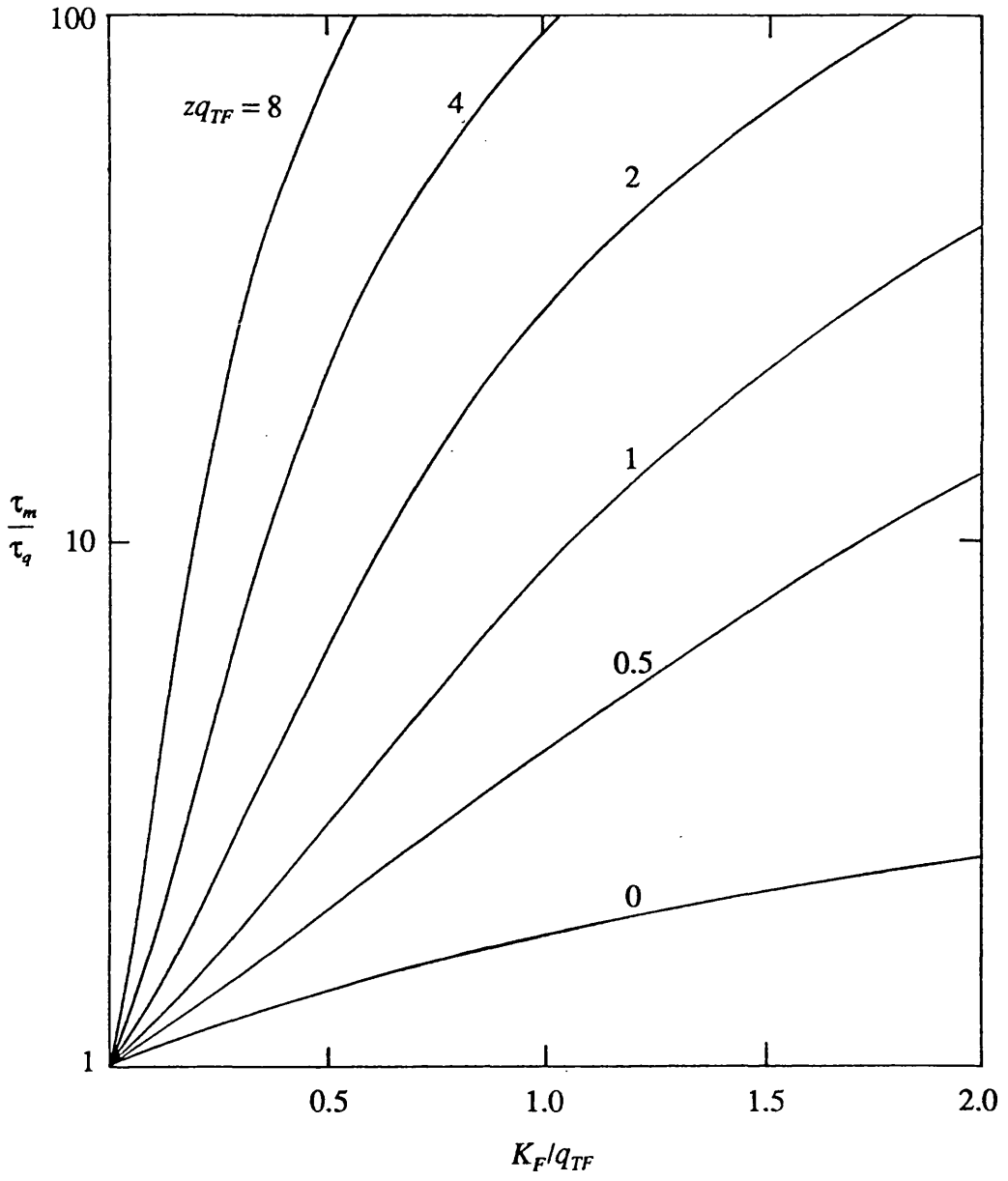

FIGURE 2.17 Calculated ratio of the momentum scattering time τ_m to the quantum scattering time τ_q, for an ideal two dimensional gas with six different values of the separation z between the electron layer and the impurity layer. Sarma et al. [1985].

The Thomas-Fermi screening parameter q_{TF} for the $Ga_{1-x}Al_xAs/GaAs$ heterostructure is given by

$$\frac{2m^*e^2}{\kappa\hbar^2} \qquad 2.72$$

where κ is the background dielectric constant. For a two dimensional gas in GaAs q_{TF} equates to 2.0×10^6 cm^{-1}.

The value of the Fermi wavevector k_F is given by

$$2\pi N_c^{\frac{1}{2}} \qquad 2.73$$

All the values converge to τ_m/τ_q equals one as k_F/q_{TF} tends to zero because for two dimensional systems the screening is independent of the wavevector for the entire accessible range of scattering wavevectors, in an electron gas with isotropic effective mass at absolute zero. For large values k_F/q_{TF} the scattering becomes increasingly peaked in the forward direction, especially for large values of z, and τ_m increases rapidly while τ_q is affected much less.

Figure 2.18 shows the calculated values of τ_m and τ_q for $Ga_{1-x}Al_xAs/GaAs$ heterojunctions, with two different acceptor levels in the GaAs as a function of spacer thickness, d, which determines the electron channel density. Sarma et al. [1985].

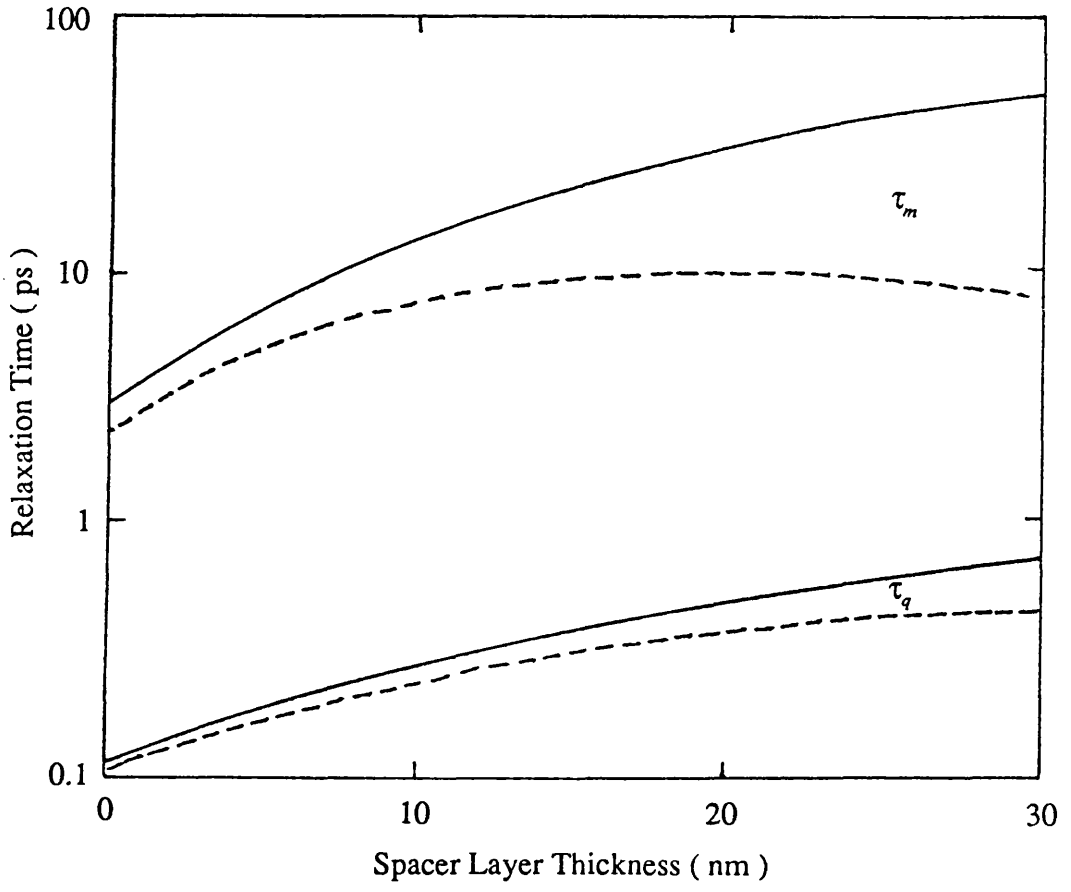

FIGURE 2.18 shows the calculated values of τ_m and τ_q as a function of spacer thickness, d, for $Ga_{1-x}Al_xAs/GaAs$ heterojunctions with GaAs acceptor levels of 10^{14} cm^{-3} (full curve) and 10^{15} cm^{-3} (dashed curve).

It is clear from figures 2.17 and 2.18 that τ_m is substantially larger than τ_q for high mobility heterojunctions. For lower

mobility heterojunctions, for which the scattering may arise from impurities closer to the channel, the difference between the two characteristic times becomes smaller.

Rikken decided that in his measurements the ratio between the two time constants was too great to be explained by Sarma's calculations. He therefore concluded that although the energy relaxation by the photo-excited electrons is very rapid, the electron gas as a whole loses energy rather slowly by phonon emission. The de-excitation of the photo-excited electrons via electron-electron scattering was considered unlikely. This would have lead to an electron gas characterised by an effective temperature, which in turn would cause the photoconductive response to be bolometric. However as this was not observed for high mobility heterostructures, in the quantum limit, phonon emission seemed to be the dominate de-excitation process. In order to explain the long decay times observed, Rikken suggested that a phonon scattering and reabsorption process takes place over the length scale characteristic of the layer dimensions.

2.7 Detection

The change in resistance of a semiconductor at the cyclotron resonance frequency has lead to several investigations into its possible application as a detector. The first of these

was in 1961 when Goodwin and Jones [1961], assessed the performance of n-type Germanium in a magnetic field of 0.18 T to detect radiation at a frequency of 34 GHz.

N-type indium antimonide has been the most common material to use as a cyclotron resonance detector in the submillimetre wavelength region [Brown and Kimmit 1963, Kimmit 1970]. The primary reason for this is its small electronic effective mass, which has enabled cyclotron resonance to be induced at relatively low magnetic fields. The mechanism of detection for this material combines a classical cyclotron resonance response described earlier with a slightly modified version of it. In the second case, the transitions responsible for the absorption are between impurity levels associated with the Landau levels rather than between the Landau levels themselves. Figure 2.19 shows the different mechanisms involved. The first of these mechanisms has been explained in the previous sections. In the second case the bound carrier absorbs energy and is energized to a bound state associated with the second Landau level. It is then scattered by interaction with the thermal vibrations of the crystal lattice into the lowest Landau level, in which it is free to contribute to conductivity. This results in a change in the detector resistance. The impurity resonance occurs at a slightly higher energy than the true cyclotron resonance.

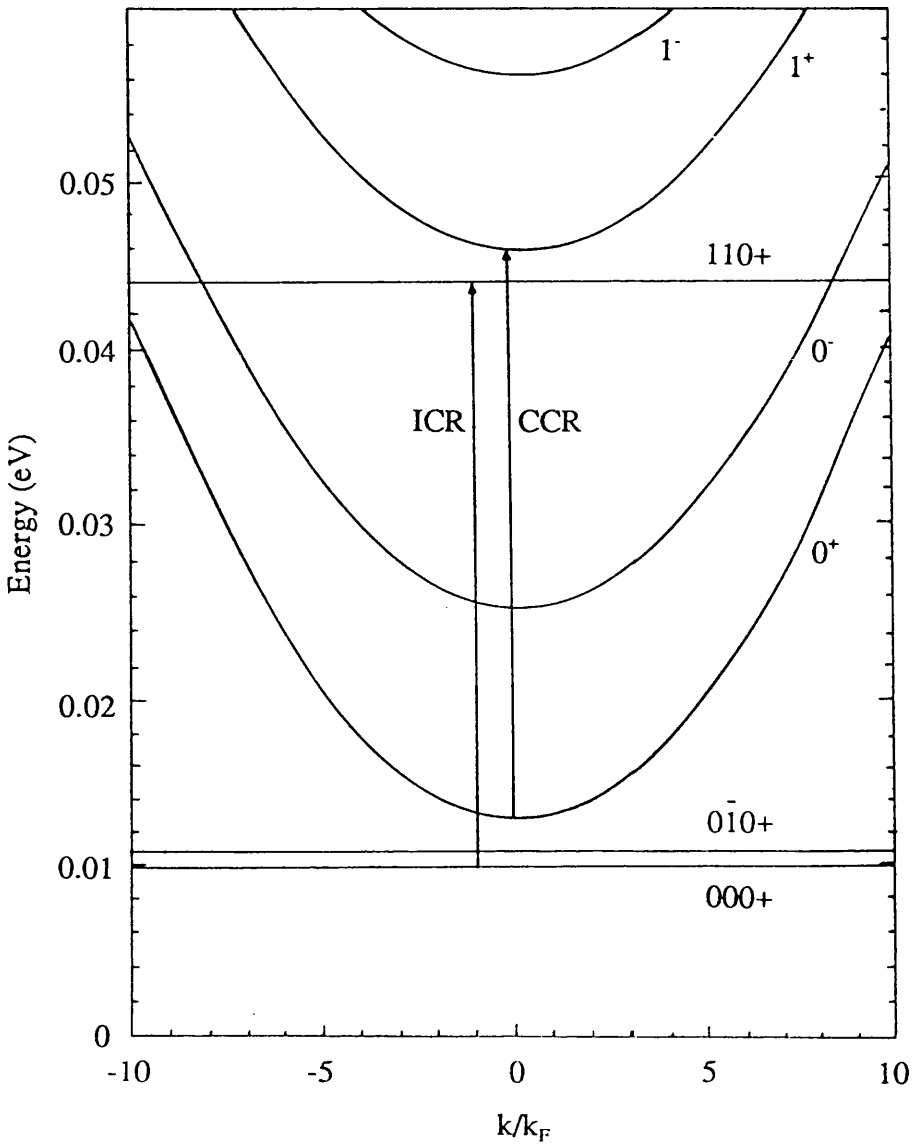

FIGURE 2.19 Lowest two Landau levels, important bound states and dominant cyclotron resonance transitions for electrons in a 5 T magnetic field.

Recent work on the indium antimonide cyclotron resonance detector has been carried out by Brown et al. [1985a]. Figure 2.20 shows the responsivity spectra for a n-type indium antimonide direct detector at 4.2 K and at various magnetic fields.

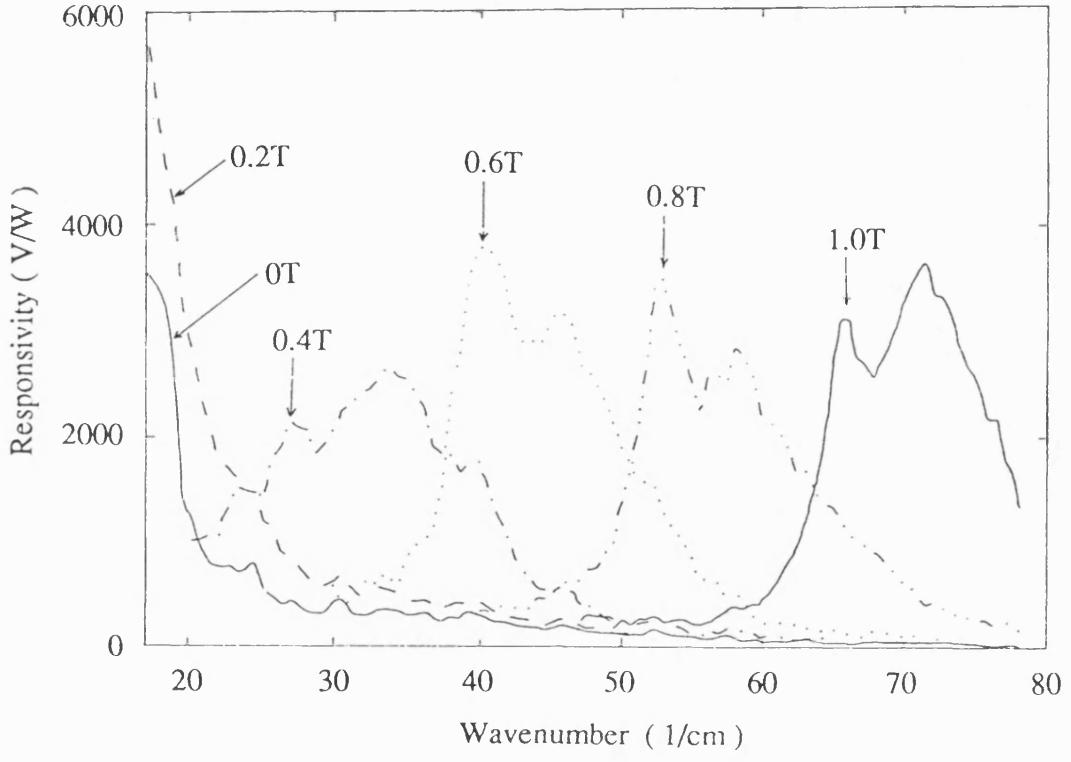

FIGURE 2.20 Responsivity spectra for n type indium antimonide direct detector at 4.2K in various magnetic fields. Brown et al. [1985a].

The vertical arrows are located at the conduction electron cyclotron resonance for each magnetic field. For magnetic

fields of equal or greater than 0.4T, the peak that occurs at a slightly higher energy is associated with the impurity electron cyclotron resonance. As well as investigating the direct detection properties of the detector he has also incorporated it into a heterodyne receiver system [Brown et al. 1985b].

2.8 The new detector

Utilization of the photoconductive cyclotron resonance signal as a detection mechanism has so far been restricted to three dimensional systems. The potential of photoconductive cyclotron resonance in two dimensional systems as a detective mechanism has not been investigated. Work carried out on two dimensional systems shows that they should have several advantages over three dimensional systems when used as detectors.

In three dimensional systems under strong magnetic fields, electrons are quantized into discrete Landau levels, but are still able to move freely in the direction of the magnetic field. The situation is different in the case of a two dimensional system, such as a $Ga_{1-x}Al_xAs/GaAs$ heterojunction. For a two dimensional system the electron motion parallel to the magnetic field is restricted by the electric field at the junction interface. There is a complete

quantization of the orbital motion. Photoconductive cyclotron resonance signals should therefore be more pronounced in a two dimension system.

The spatial separation of the parent donors from the conducting electrons means that the two dimensional gas is practically free from ionised-impurity scattering, the limiting factor for the low temperature mobility. High mobility detectors are formed, with narrow Landau level widths, resulting in sharply defined cyclotron resonance peaks.

A $Ga_{1-x}Al_xAs/GaAs$ heterojunction detector will also have several other significant advantages. Since the mobile carriers in the well originate from donors outside of the well, they are unable to recombine as the temperature is reduced. Hence the detector will remain conducting even at the lowest temperatures.

The carrier concentration can be varied and therefore optimised by illumination with visible light. It was noted by Stormer et al in 1979 that the material demonstrated a persistent photoeffect, allowing its electron density within the well to be increased by exposure to light. The effect has a time constant of several days and is reversible by heating the sample to 100 K or more. The existence of this persistent photoconductivity [Nelson 1977] is thought

to be due to deep traps in the $Ga_{1-x}Al_xAs$, associated either with the satellite valleys at the X and L points of the Brillouin zone, or defect centres.

A number of heterojunctions can be grown in parallel to form a superlattice structure [Dohler 1983]. It may be possible to increase the sensitivity of the detector by detecting the signal with several heterojunctions at once, using such a structure.

The fast component of the response time of the photoconductive cyclotron resonance signal was found by Rikken et al to be approximately exponential with a characteristic time of 20ns. This compares favourably with the time constant of approximately 10^{-6} s associated with indium antimonide detectors.

These attributes lead to the present investigation into the use of photoconductive cyclotron resonance in a $Ga_{1-x}Al_xAs$/GaAs heterojunction as a detecting mechanism for sub-millimetre radiation.

CHAPTER 3 INITIAL DETECTOR SYSTEM

Initial experiments were conducted at Oxford University. In these two $Ga_{1-x}Al_xAs/GaAs$ heterojunction detectors were used to detect signals from a 119 μm (2.5 THz) optically pumped laser, a 98 GHz Gunn oscillator and a multi-frequency Impatt oscillator.

3.1 Measurement system

Figure 3.1 shows the measurement system used. Signals from the sources were modulated by a variable speed chopper, and then guided along a light pipe to the detector. The signal had to travel through a right angle due to the design of the cryostat. This was achieved by using a mirror to reflect the signal through the right angle and along the cryostat light pipe. For the preliminary experiments involving detector A, the detector was simply mounted on a washer system. For experiments involving detector B the detector was mounted inside a specially designed detector block. The detector was situated within the cryostat at the centre of an electromagnet. The detector was constant current biased and the output voltage amplified and phase-sensitively detected. The input power level was adjusted using a variable attenuator.

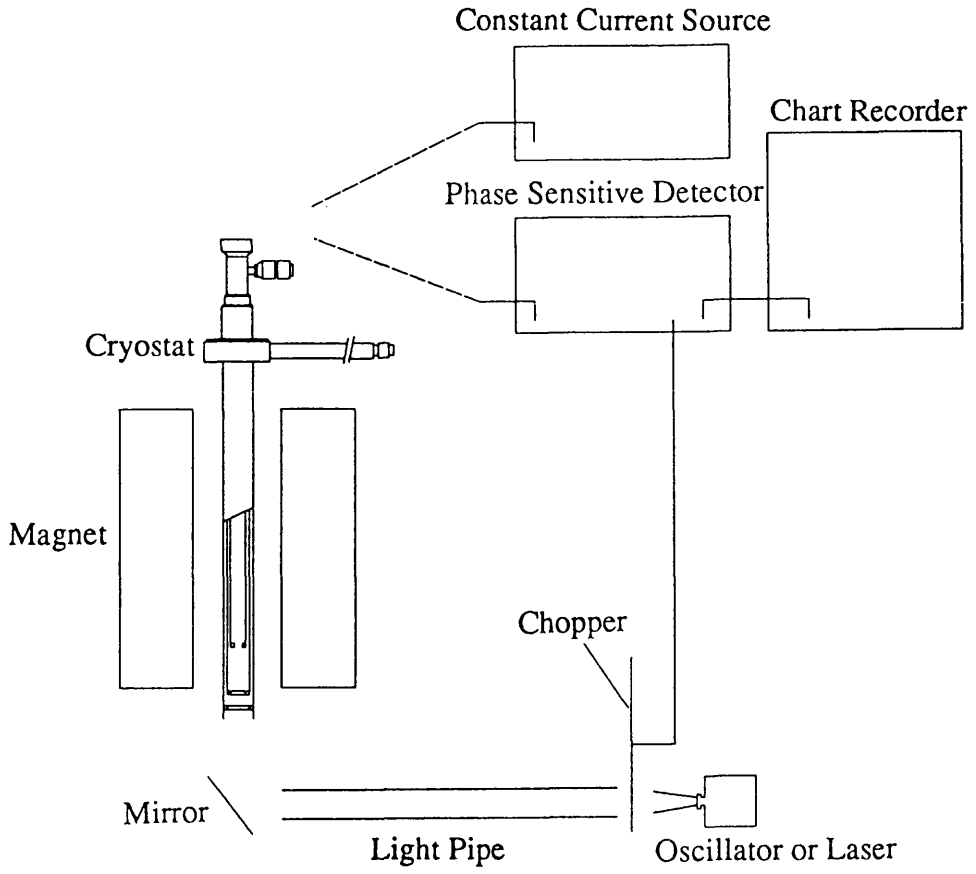

FIGURE 3.1 Oxford measurement system.

3.2 Detectors

All of the detectors used in this project were prepared using molecular beam epitaxy at the Philips Research Laboratories, Redhill. Ohmic contacts were prepared on the detectors by the rapid alloying of a Au:Ge:Ni metalization. The two detectors that were studied at Oxford are shown in figure 3.2.

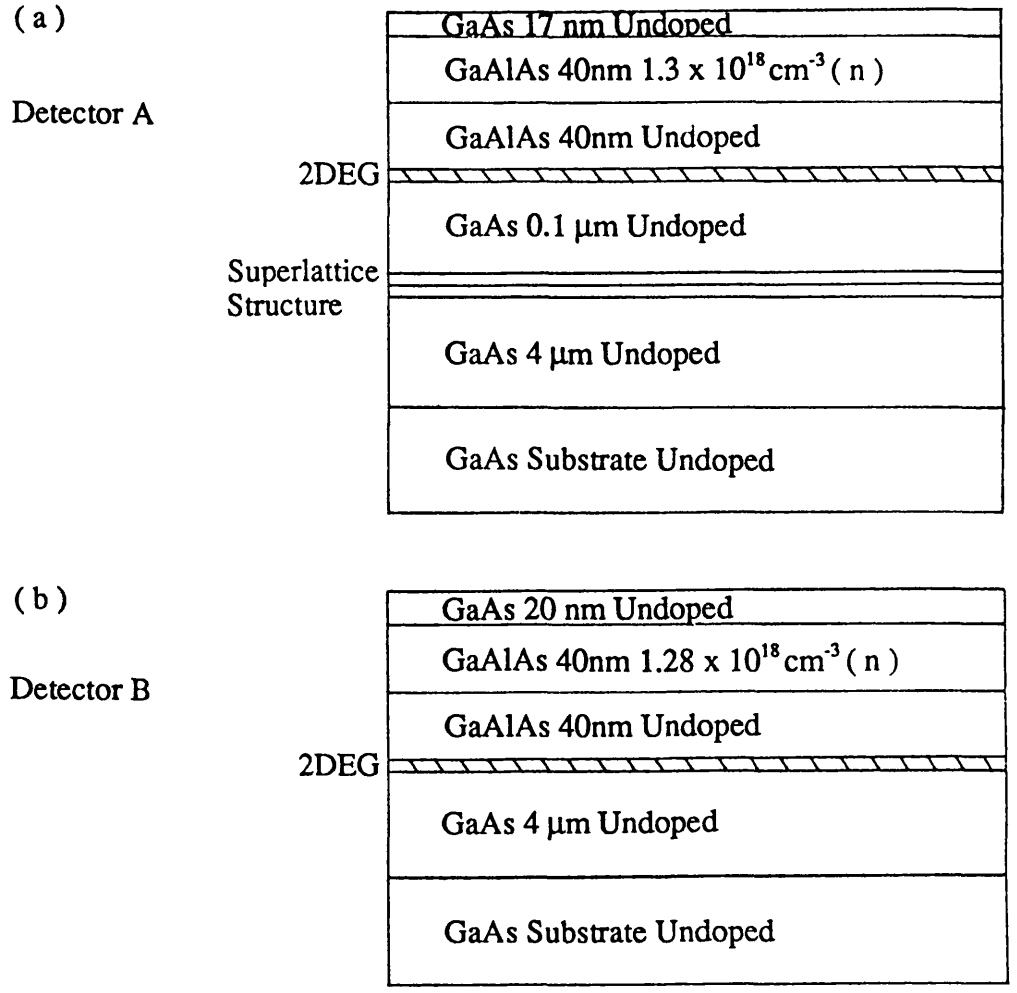

FIGURE 3.2 Sequence of layers grown for the detectors.

Although detector A shows a superlattice structure contacts were only made to the two dimensional electron gas shown. For the two detectors, at 4.2 K in the dark, the electron concentrations in the two-dimensional gas were approximately 2.1 x 10^{11} cm^{-2} and 1.5 x 10^{11} cm^{-2}, with mobilities of approximately 8 x 10^5 $cm^2V^{-1}s^{-1}$ and 5 x 10^5 $cm^2V^{-1}s^{-1}$

respectively. The carrier density could be increased to approximately 4 x 10^{11} cm^{-2} by using the persistent photoconductivity effect. The background residual donor and acceptor concentrations of both these detectors were approximately 2 x 10^{14} cm^{-3} [Foxon and Harris 1986]. Therefore from the results of calculations carried out by Stern and Das Sarma shown in section 2.2.2, the lowest confined state occurs at 25 meV above the bottom of the well. The Fermi level lies 7 meV above this and the second confined level, which is 20 meV above the lowest, is therefore unoccupied and remains so over the whole carrier density.

Figure 3.3 shows the $Ga_{1-x}Al_xAs$/GaAs heterojunction detector geometry used for the majority of experiments. Detector A was different from the other detectors used in this project, as it was in the form of a Hall bar.

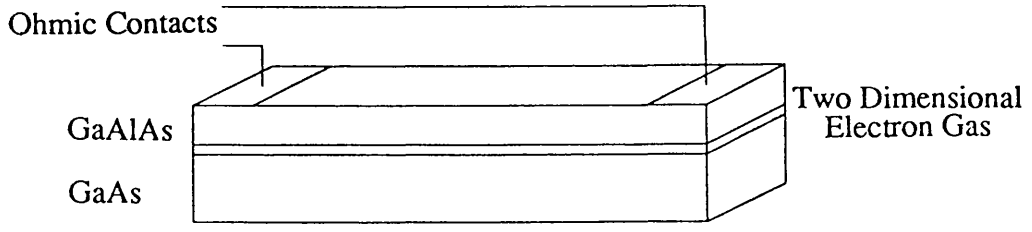

FIGURE 3.3 A $Ga_{1-x}Al_xAs$/GaAs heterojunction detector.

3.3 Detector mount design

A detector mount was designed for use with the Oxford measurement system. The mount is shown in figure 3.4.

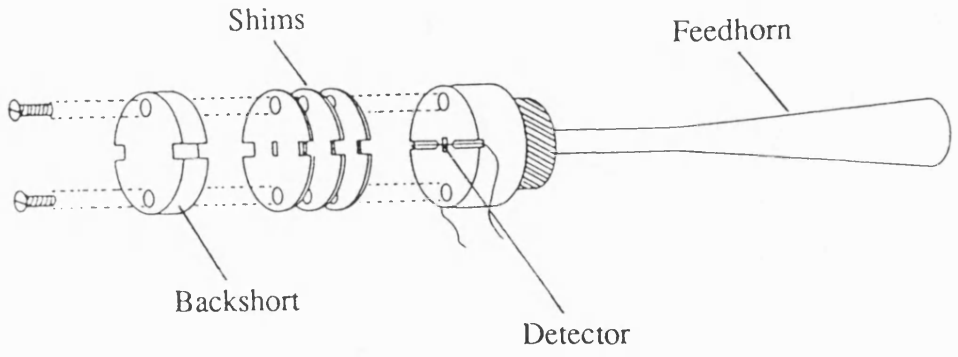

FIGURE 3.4 Detector mount used with Oxford system.

The mount was designed so that detector B was positioned within a slot across a circular waveguide. A smooth walled conical feedhorn was attached to the opposite side of the waveguide using a phosphor bronze washer and spring system. A feedhorn was used to match the essentially free space waves from a large aperture to the circular waveguide. A phosphor bronze washer was used as it was imperative that the detector mount was completely non-magnetic, as it was to be placed in a high magnetic field. The waveguide was then built up behind the detector using shims. A backshort was attached at a distance of approximately one quarter of a guide wavelength from the detector for a free space frequency of 98 GHz. One quarter of a guide wavelength is

approximately the distance required to ensure maximum absorption of power to the detector, (see appendix A). Black polyethylene and fluorogold were attached to the receiving end of the feedhorn for experiments involving both the Gunn and Impatt oscillator. These ensured that no visible or infrared light could enter the system. Two slots were cut in the shims and the backshort for the contact wires from the detector to run up to the output connections in the Oxford cryostat. A photograph of the detector mount is shown in figure 3.5.

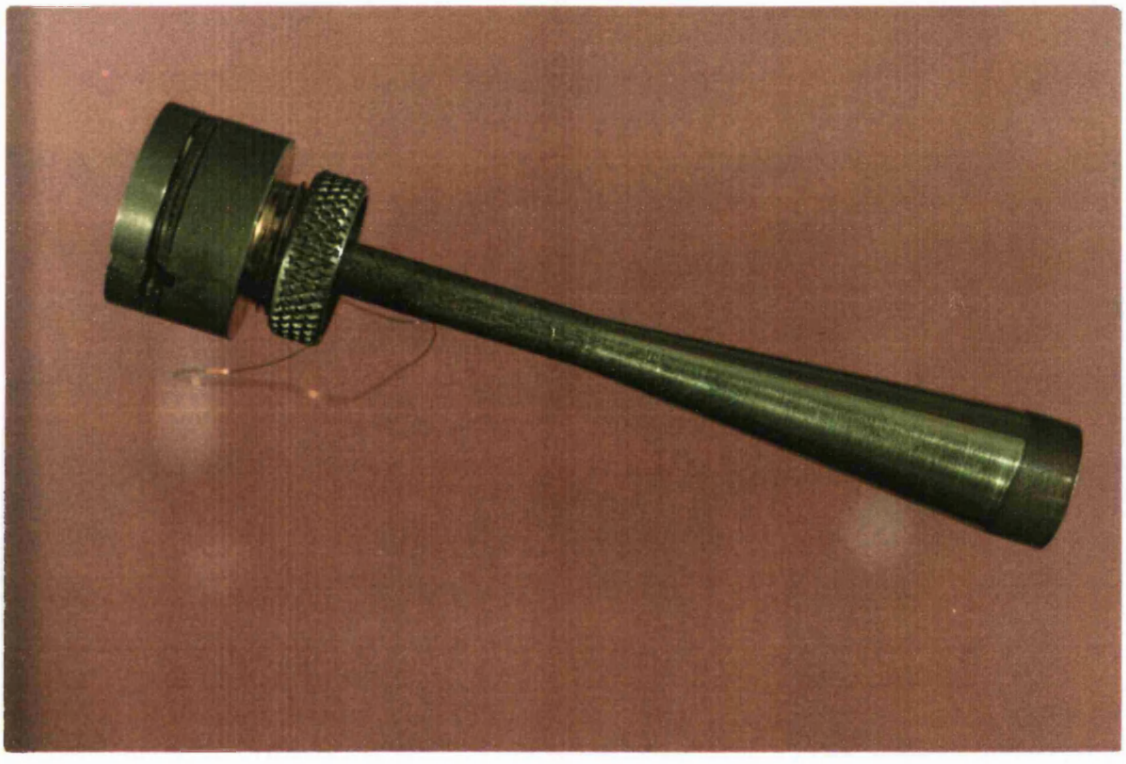

FIGURE 3.5 Photograph of detector mount used with Oxford system.

3.4 Mounting of detector

Wires were bonded to detector B using silver epoxy applied onto the Au:Ge:Ni contacts. This was then cured for 30 minutes at 150^{o}C. Figure 3.6 shows the mounted sample.

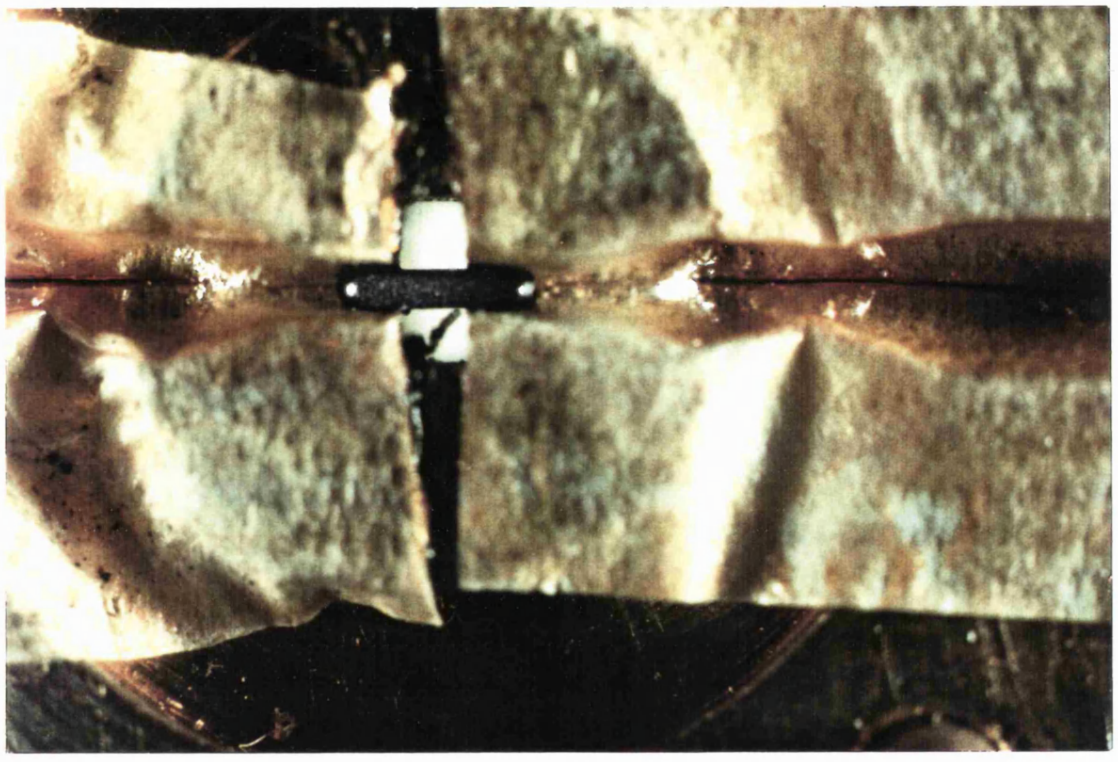

FIGURE 3.6 Photograph of the mounted detector.

It was important that a short circuit was not developed across the detector mount. After experimentation, it was found that one way to achieve this was to insulate the connection wires from the mount using thin paper soaked in

general electrical varnish. The saturated paper was placed upon the detector mount and allowed to dry. After checking that this had formed an insulated layer, the detector was placed across the waveguide, and the connection wires glued into place. Gold plated pins were then soldered to the ends of the connection wires.

3.5 Cryogenic apparatus

The cryostat used to cool the detector operated on the principle of a controlled continuous transfer of liquid helium from the storage vessel to the heat exchanger which surrounded the sample space. The main parts of the cryostat are shown in figure 3.7. The detector was top-loaded and cooled to 4.2 K by a static column of exchange gas which thermally linked the detector to the heat exchanger. It was a standard design modified to have windows in the heat exchanger, radiation shield and case to allow bottom-access optical experiments. The bottom had an inside thread which took a 12 mm diameter light pipe. The inside diameter of the sample space was nominally 20 mm.

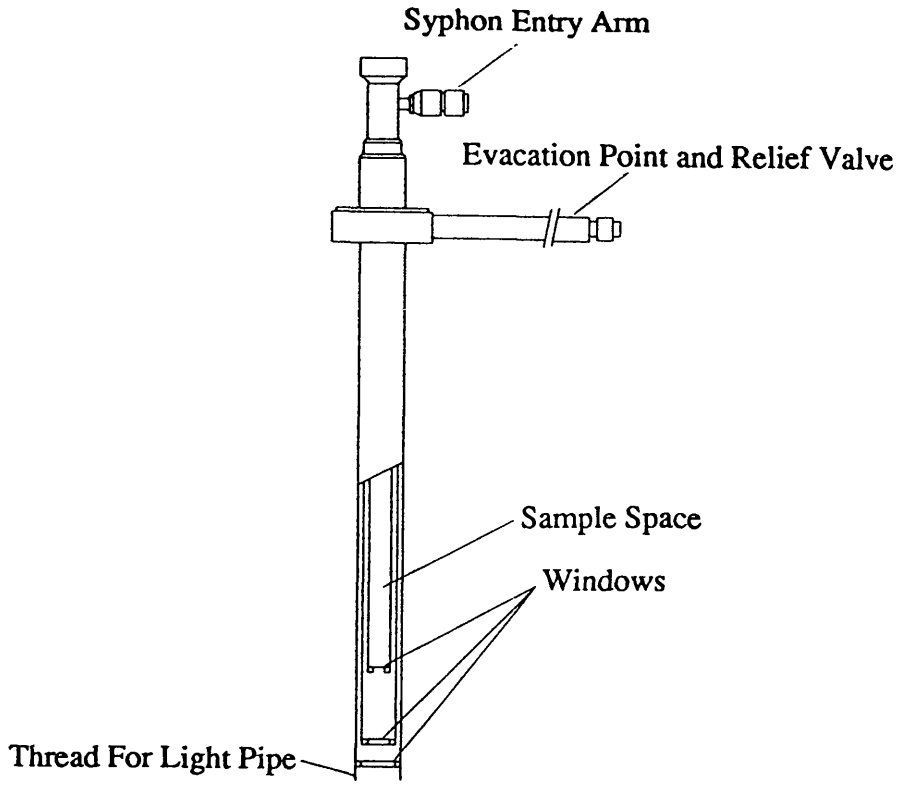

FIGURE 3.7 Oxford cryostat.

An insert was placed within the sample space. Figure 3.8 shows the bottom of the insert as it was used. The 12 mm diameter light pipe carried transmitted light up to a separate sample cryostat and was enclosed in a 19.2 mm diameter tube forming the main body of the insert. The light pipe continued about 50 mm beyond the end of the main body and carried a P.T.F.E. connector block around it. The block held seven gold-plated sockets connected to wires which ran to a plug at the top of the insert. On the end of the light pipe was

a brass block to which the detector mount was fixed. The outside of the brass block was threaded to take a cone which screws over the sample. Four slots were cut in the brass block for wires from the detector to run up to the connection ring.

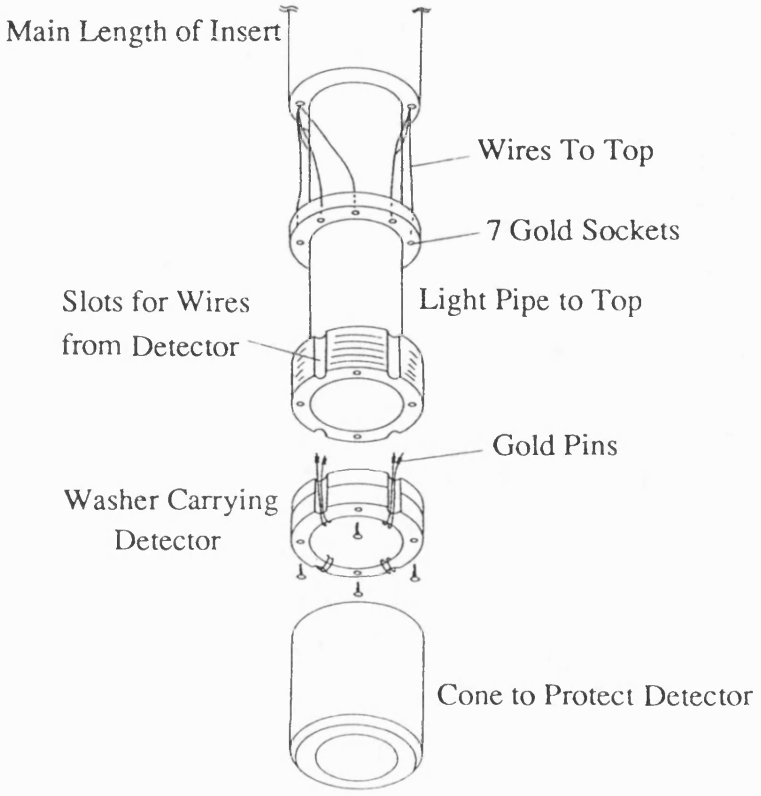

FIGURE 3.8 Cryostat insert.

3.6 Results

3.6.1 Detection of 119 μm laser

Detector A was initially used to detect radiation of wavelength 119 μm, (2.5 THz) from an optically pumped infra-red laser. For this part of the experiment the resistance of the detector was measured directly, without the use of the phase sensitive detector and chopper. Figure 3.9 shows the variation of the detector's resistance with applied magnetic field.

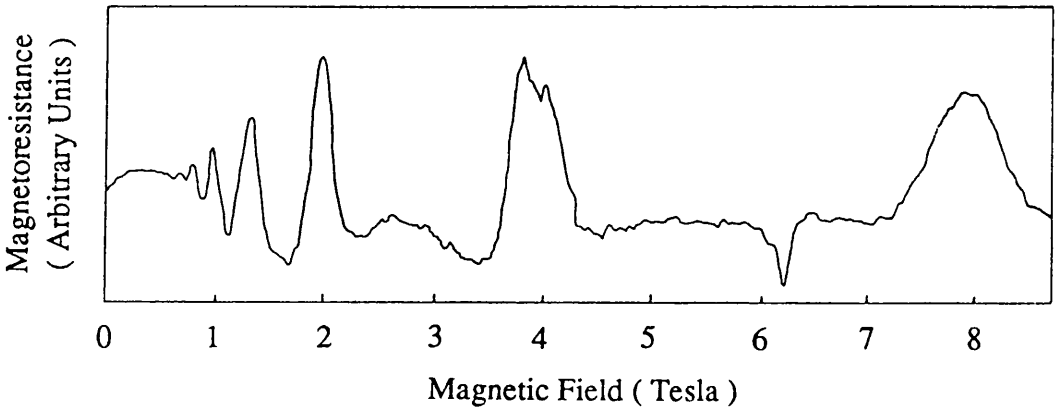

FIGURE 3.9 Magnetoresistance of detector as a function of magnetic field.

The photoconductive cyclotron resonance can be observed on a background of Shubnikov de Haas oscillations. The cyclotron resonance occurs at a magnetic field strength of 6.2T. Using equation 2.10:-

$$\omega_c = \frac{eB}{m^*} \qquad 2.10$$

gives the conducting electrons an effective mass m^* of $0.0695m_o$.

Resistivity minima in the Shubnikov de Haas oscillation occurs whenever the Fermi level lies between two Landau levels. In this situation one Landau level is completely full with the next one completely empty. The flat minimum at approximately 3 T corresponds to complete filling of the N=0 Landau level. The broad minimum in the region of 4-7 T corresponds to the spin splitting of the N=0 Landau level. From the period of the Shubnikov de Haas oscillations the carrier concentration of the 2DEG can be determined using equation 2.50:-

$$N_c = N\frac{2eB_N}{h} \qquad 2.50$$

A plot of the reciprocal magnetic field against oscillation minima number, and hence Landau level number is shown in figure 3.10.

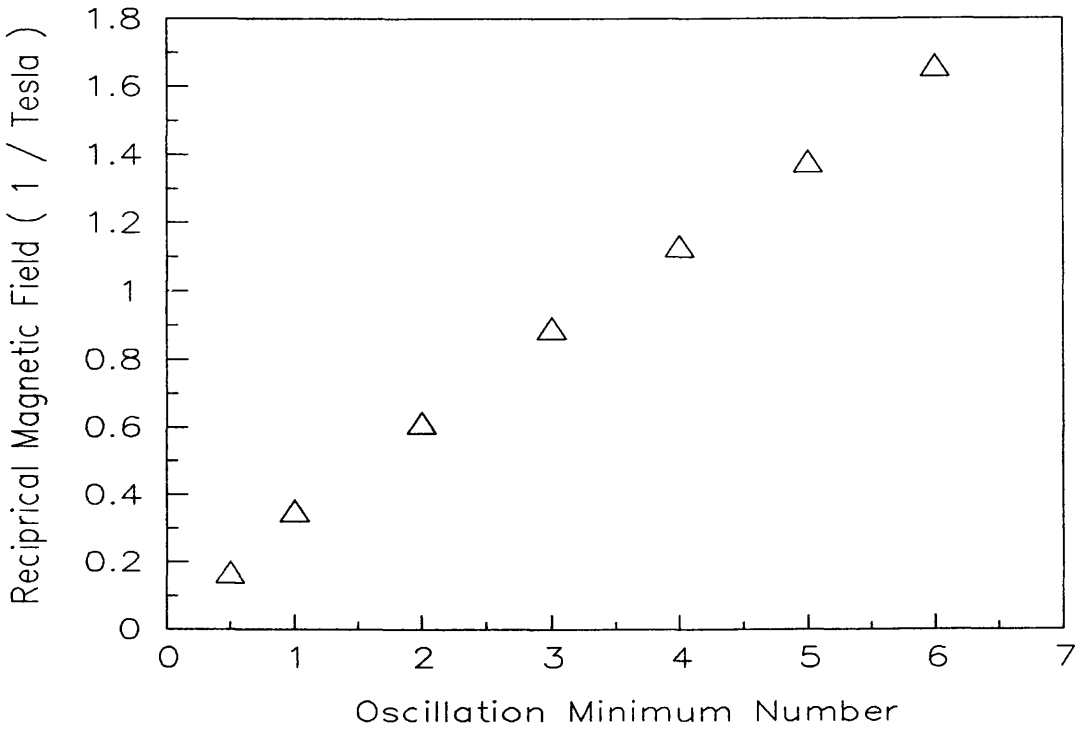

FIGURE 3.10 Plot of reciprocal magnetic field against oscillation minima number.

From figure 3.10 a value for the two dimensional gas electron concentration of 1.82 x 10^{11} cm^{-2} was deduced.

No conclusions about the responsivity of the detector could be drawn for the 119 μm signal, since the incident power level could not be assessed.

3.6.2 Detection of a 98 GHz Gunn oscillator

Radiation was phase sensitively detected from a 98 GHz Gunn oscillator using both detectors. The signals observed for detector A and B are shown in figures 3.11 and 3.12

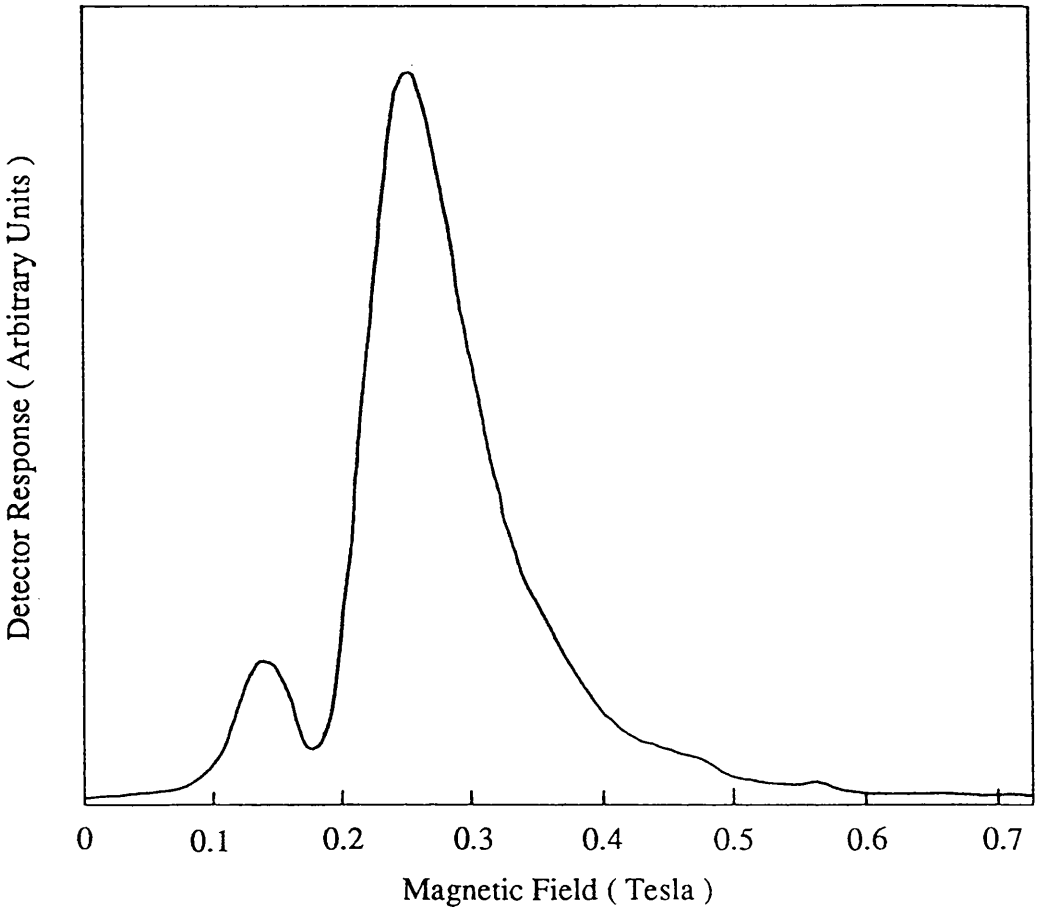

FIGURE 3.11 Photoconductive cyclotron resonance signal produced by a 98 GHz Gunn oscillator for detector A.

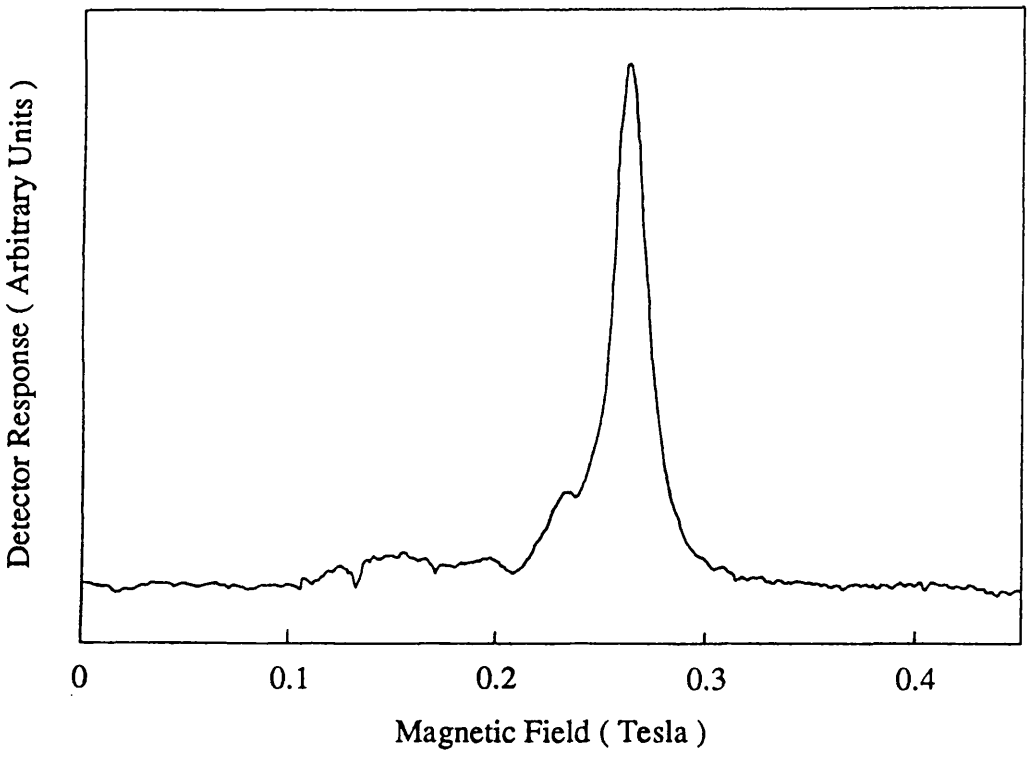

FIGURE 3.12 Photoconductive cyclotron resonance signal produced by a 98 GHz Gunn oscillator for detector B.

The chopper frequency for all results was 1 KHz unless otherwise stated. The photoconductive cyclotron resonance signal observed for each of the detectors was essentially the same shape, although detector B's signal had a narrower linewidth. Concentrating on the photoconductive cyclotron resonance signal produced by a 98 GHz Gunn oscillator for detector B shown in figure 3.12, there is a strong detection of the 98 GHz signal at a magnetic field of 0.259 T. The lineshape observed appears asymmetric, with the resonance

frequency shifted to the high frequency side. From equation 2.10 the resonance peak for a cyclotron frequency of 98 GHz would be at a magnetic field of 0.239 T. This can be explained by Ando's theory for the case of short range scatterers as described in section 2.4. Ando also stated that for low carrier concentrations, the cyclotron resonance frequency would shift to the low frequency side. However, the sample discussed had a carrier density of 1×10^{11} cm^{-2}. The Fermi energy for such a sample would only be 3.5 meV above the first electron energy level. The energy gap $\hbar\omega_c$ between Landau levels was 3.68 meV for the stated cyclotron resonance frequency. Therefore only the low energy part of the broadened ground Landau level would be occupied. For this detector, however, the Fermi energy lies 7 meV above first electron energy level. The energy gap between the Landau levels for a cyclotron frequency of 98 GHz is 0.41 meV. Therefore several Landau levels will be full and the shift of the cyclotron resonance peak to lower energies is not observed.

The linewidth for detector B is approximately 0.05 T or less which indicates the high quality of the detector and suggests that sharp tunability of the detection is possible. As the cyclotron resonance peak is formed by the transition of electrons from one Landau level to the next it follows that the width of the peak will depend upon the width of the adjacent Landau levels concerned. The width of the Landau

levels depend upon the amount of scattering taking place within them. The Landau level width is given by equation 2.71:-

$$\Gamma = \frac{\hbar}{2\tau_q}. \qquad 2.71$$

The sharpness of the observed cyclotron resonance peak is therefore due to the long scattering time constant attainable within these high quality $Ga_{1-x}Al_xAs/GaAs$ heterojunctions. Therefore the difference in the linewidths observed between detectors A and B could have been caused by a difference in their scattering time constants.

An expanded view of the cyclotron resonance lineshape for detector A is shown in figure 3.13. Quantum oscillations can be observed which are characteristic of the two dimensional system. As stated in section 2.4, such oscillations in a three dimensional system would be smeared out by the existence of the motion along the direction of the magnetic field. These oscillations are caused by the Fermi level passing through many different Landau levels successively. Consequently, as the conductivity depends strongly on the position of the Fermi level relative to the Landau levels, an oscillatory behaviour occurs.

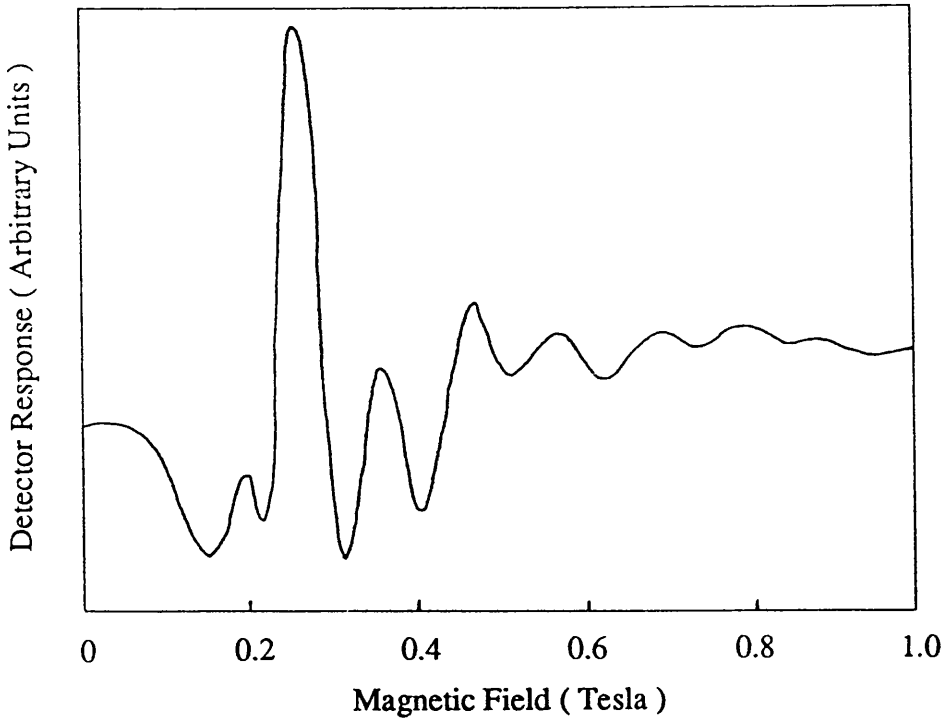

FIGURE 3.13 Quantum oscillations observed in photoconductive cyclotron resonance peak.

The variation of the detector response for detector A with d.c. bias is shown in figure 3.14. The output is seen to increase with bias current until it reaches a plateau at around 80 μA. Large signals were sometimes obtained under zero bias conditions. These signals could be explained by the detector producing its own electronic current. Thermoelectric power caused by a temperature gradient across a $Ga_{1-x}Al_xAs/GaAs$ heterojunction has been shown to produce

such a current [Okuyama and Tokuda 1990]. This effect will not be discussed any further in this thesis, but may be important in the future development of the detector.

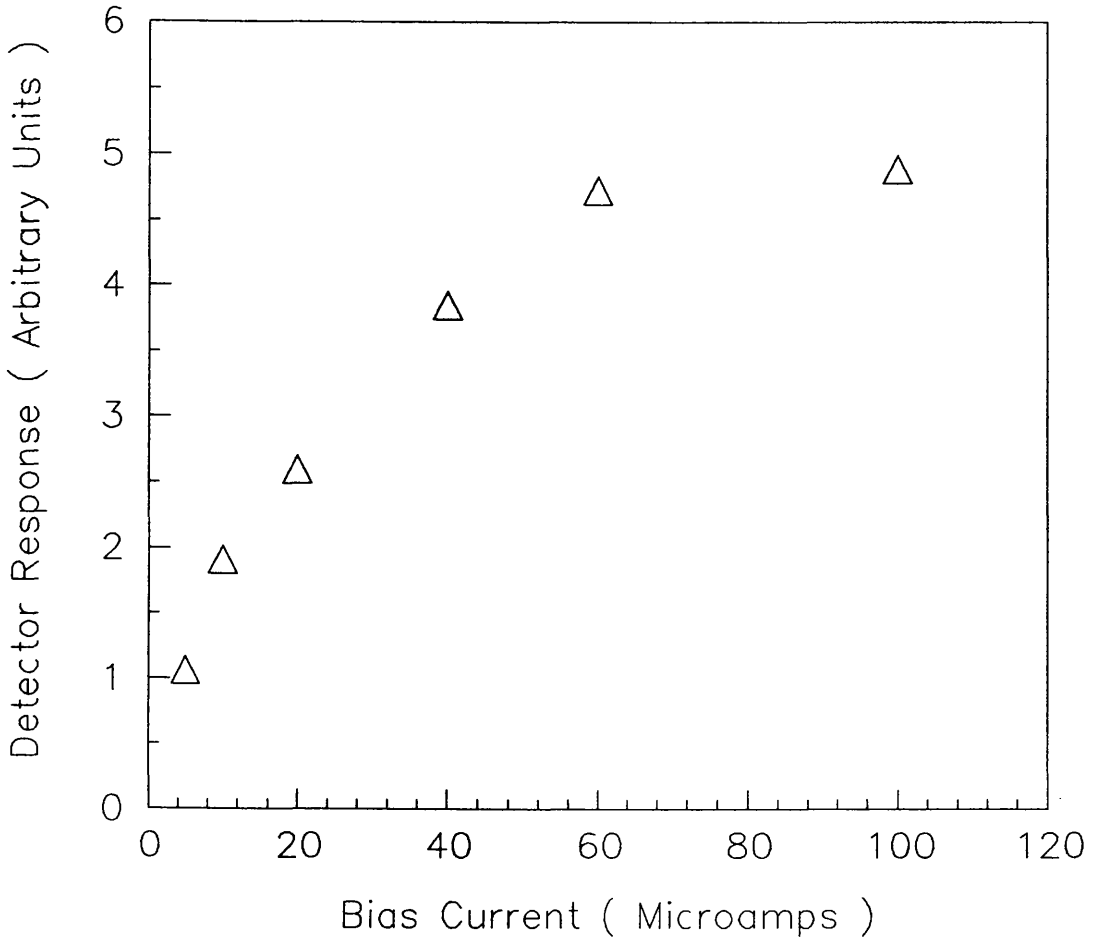

FIGURE 3.14 Plot of the variation of detector response with d.c. bias current.

By measuring the amplitude of the noise fluctuations seen on the output trace, and comparing it to the cyclotron resonance signal amplitude, a rough estimate of the N.E.P. was made. For detector A a N.E.P. of 4 x 10^{-12} W $Hz^{-1/2}$ was estimated. The estimate took into account the 11dB power loss down the initial piece of light pipe. The estimate also took into account the fact that the actual area of the detector which was contributing to the change in resistance was only a fraction of the total area irradiated. Detector B was mounted in a specially designed mount incorporating a backshort to maximise the electric field strength at the two dimensional electron gas. Therefore an area correction is not valid for this system. For detector B a N.E.P. of 8 x 10^{-10} W $Hz^{-1/2}$ was estimated. This implies that the backshort in the detector mount may not have been located in the optimum position behind the detector. A more satisfactory detector mount would have a movable backshort, which could be adjusted to optimise the power absorbed by the two dimensional electron gas.

The variation of the detector response for detector B with the chopping frequency is shown in figure 3.15.

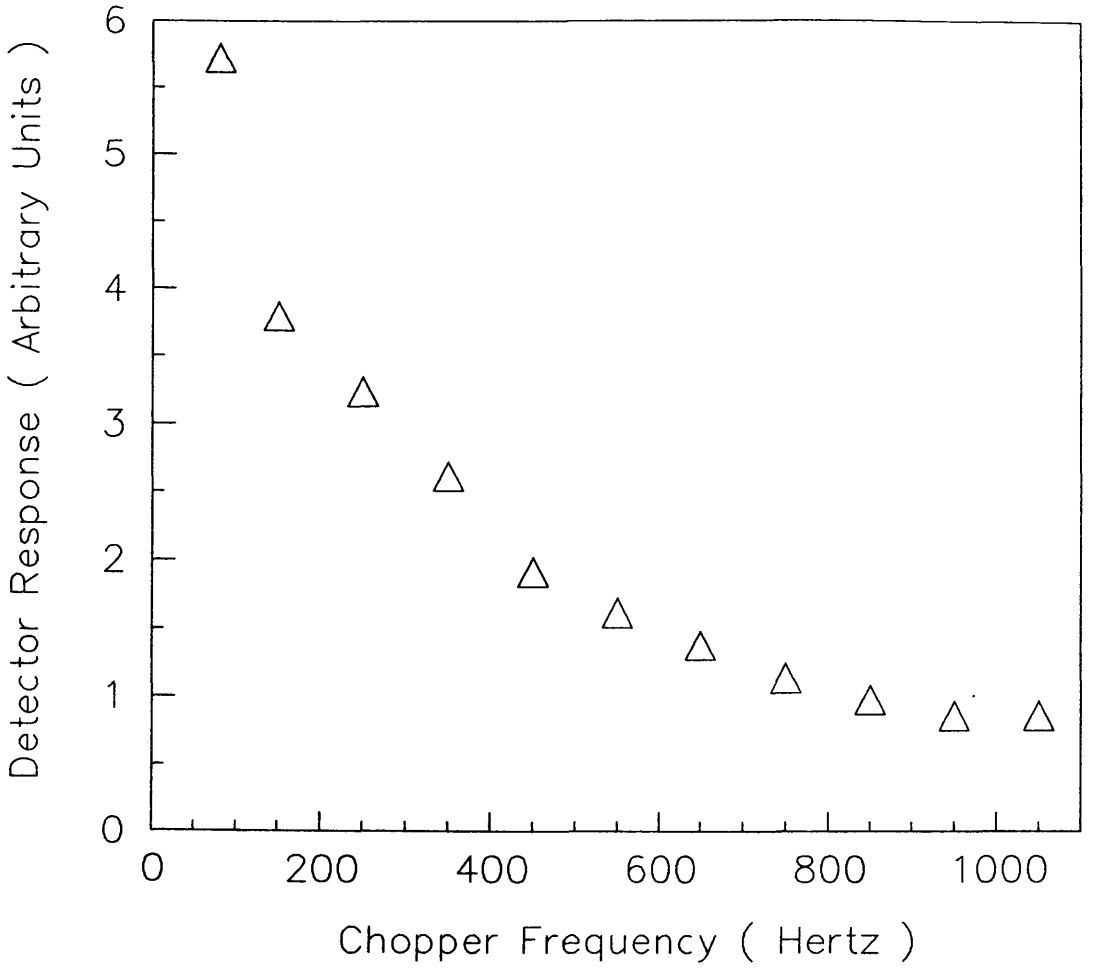

FIGURE 3.15 Plot of the variation of detector response with chopping frequency.

It can be seen that the response falls by a factor of approximately six between the frequencies of 100 Hz and 1 KHz. The signal appears to be dominated initially by the lattice temperature and at higher frequencies by the electronic processes which lead to a change in the electron distribution, (and in the simplest case to a variation in electron temperature). At the high chopping speed used during

these experiments, only the modulation of the resistivity due to electronic processes will be seen. Any modulation due to the change in the lattice temperature will have too long a time constant to be observed.

3.6.3 Harmonics of an Impatt oscillator

Detector B was finally used to detect the radiation from an Impatt oscillator tuned to give harmonics at 90 and 180 GHz. The variation of the detector response with magnetic field is shown in figure 3.16. Two strong cyclotron resonance peaks can be observed illustrating the potential of the device as a low resolution scanning spectrometer. A weaker peak of the third harmonic can also be seen.

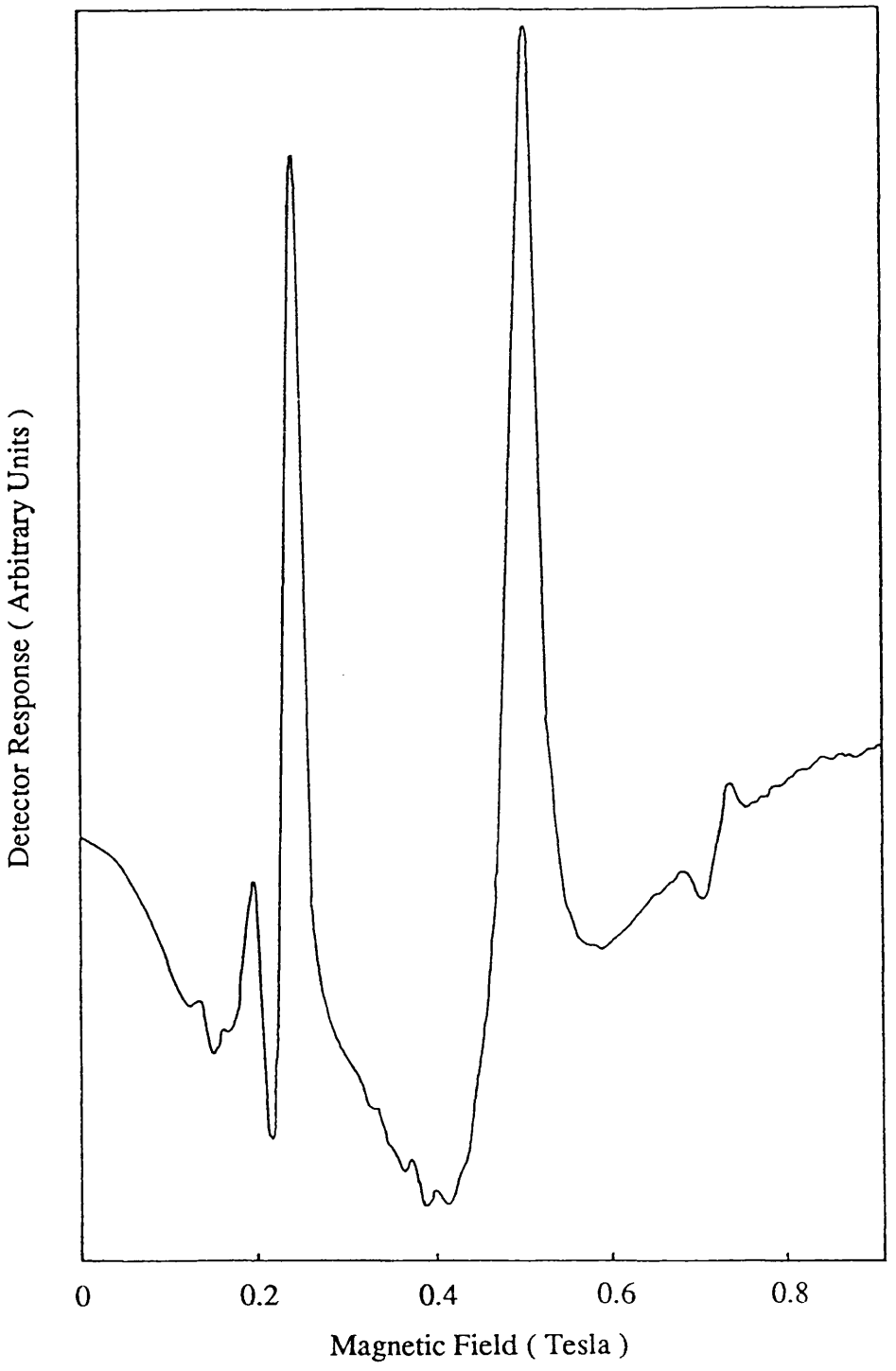

FIGURE 3.16 Photoconductive cyclotron resonance peaks produced by harmonics from an Impatt oscillator.

CHAPTER 4 INITIAL BATH DETECTOR SYSTEM

4.1 Measurement system

Figure 4.1 shows the measurement system used.

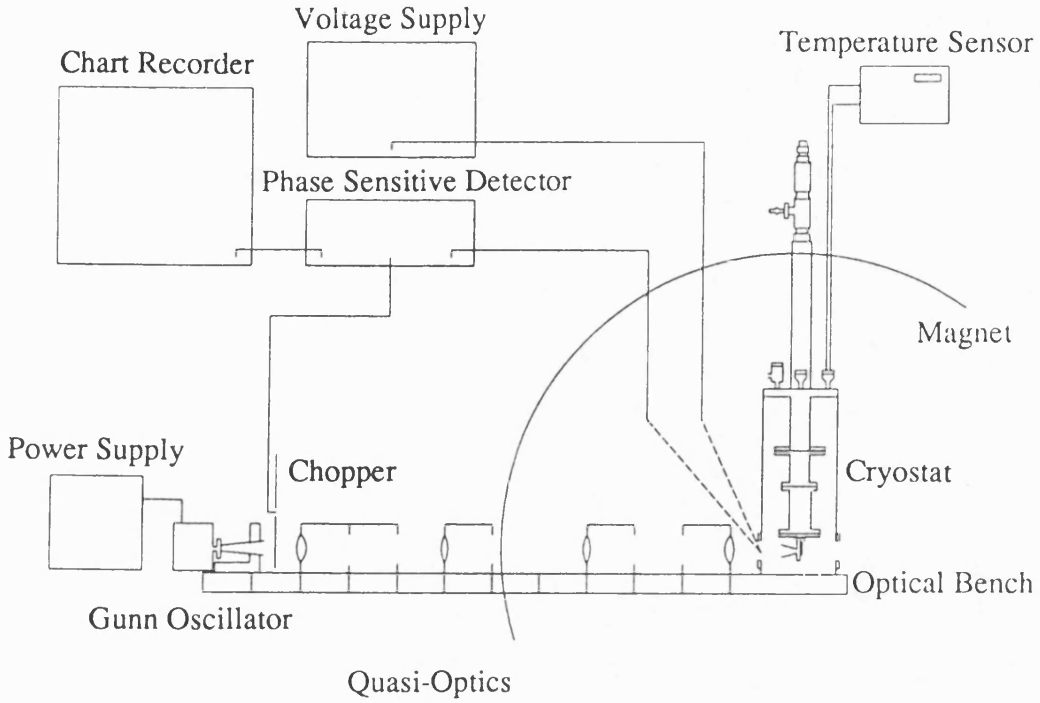

FIGURE 4.1 Initial Bath measurement system.

The detector was mounted in a specially designed mount inside an Oxford Instruments CF104 continuous flow cryostat. The cryostat was situated at the centre of an electromagnet capable of being adjusted up to a magnetic field of two tesla. Signals from a Gunn oscillator were modulated by a variable speed chopper and then directed via quasi-optics onto the detector. The detector was constant current biased

with a variable voltage supply and cooled resistor. The output voltage was amplified and then phase-sensitively detected with an Ithaco Dynatrac amplifier. The input signal level was adjusted using a variable attenuator.

4.2 Detector

For these experiments detector B, as shown in figure 3.2(b), was used. As stated in section 3.2, at 4.2 K in the dark, the electron concentration in the two-dimensional gas was approximately 1.5 x 10^{11} cm^{-2}, with a mobility of approximately 5 x 10^5 $cm^2V^{-1}s^{-1}$. The carrier density could be increased to approximately 4 x 10^{11} cm^{-2} by using the persistent photoconductivity effect.

4.3 Detector mount design

A new detector mount was designed for use with this system. The mount is shown in figures 4.2 and 4.3.

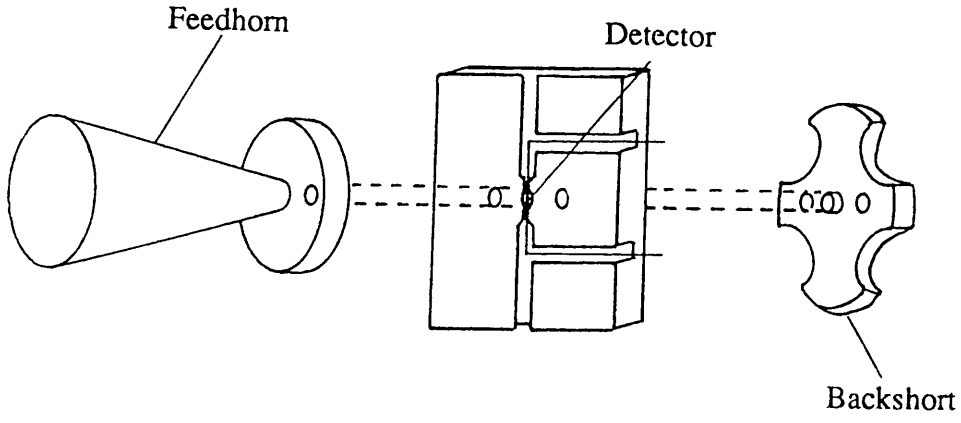

FIGURE 4.2 Detector mount.

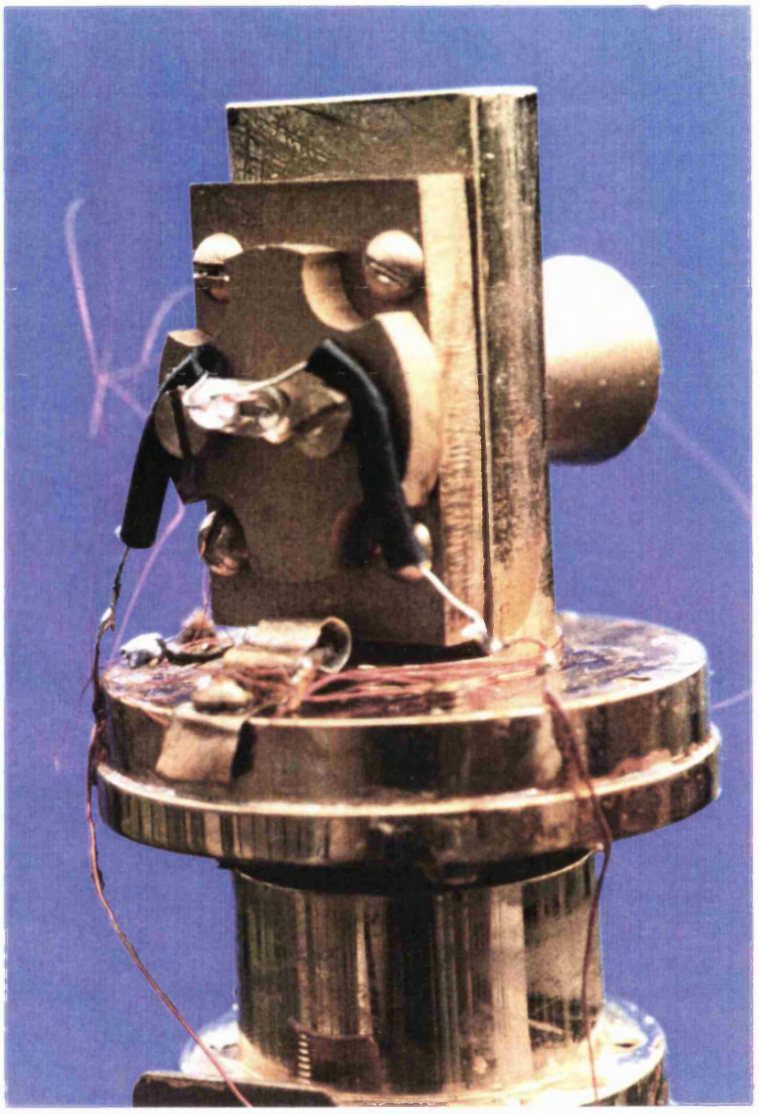

FIGURE 4.3 Photograph of detector mount.

The detector was once again mounted within a slot across a circular waveguide. A 2 cm long smooth walled conical feedhorn was mounted directly onto this. Black polyethylene and

fluorogold were attached to the front of the feedhorn to ensure that no visible or infrared light could enter the system. A backshort was then attached on to the opposite end of the waveguide. In this design the backshort was machined so that once the system was fitted together it would be approximately one quarter of a guide wavelength behind the detector, for a frequency of 98 GHz, thus avoiding any need for shims. A small hole was drilled through the backshort, and a small electric light bulb was attached to the back of it. This allowed the sample to be illuminated while it was at 4.2 K. The mount was designed so that it would fit directly onto the sample holder in the cryostat.

4.4 Mounting of detector

Wires were bonded to the detector using silver epoxy applied onto the Au:Ge:Ni contacts. The detector was then cured for 30 minutes at 150^{o}C. The detector mount was painted with general electrical varnish to ensure that it was electrically insulated from the detector and its connection wires. After checking that an insulating layer had been formed, the detector was placed across the waveguide and the connection wires glued into place.

4.5 Cryogenic apparatus

The cryostat used to cool the detector operated on the principle of a controlled continuous transfer of liquid

helium from a storage vessel to a heat exchanger connected to the sample space. The main parts of the cryostat are shown in figure 4.4.

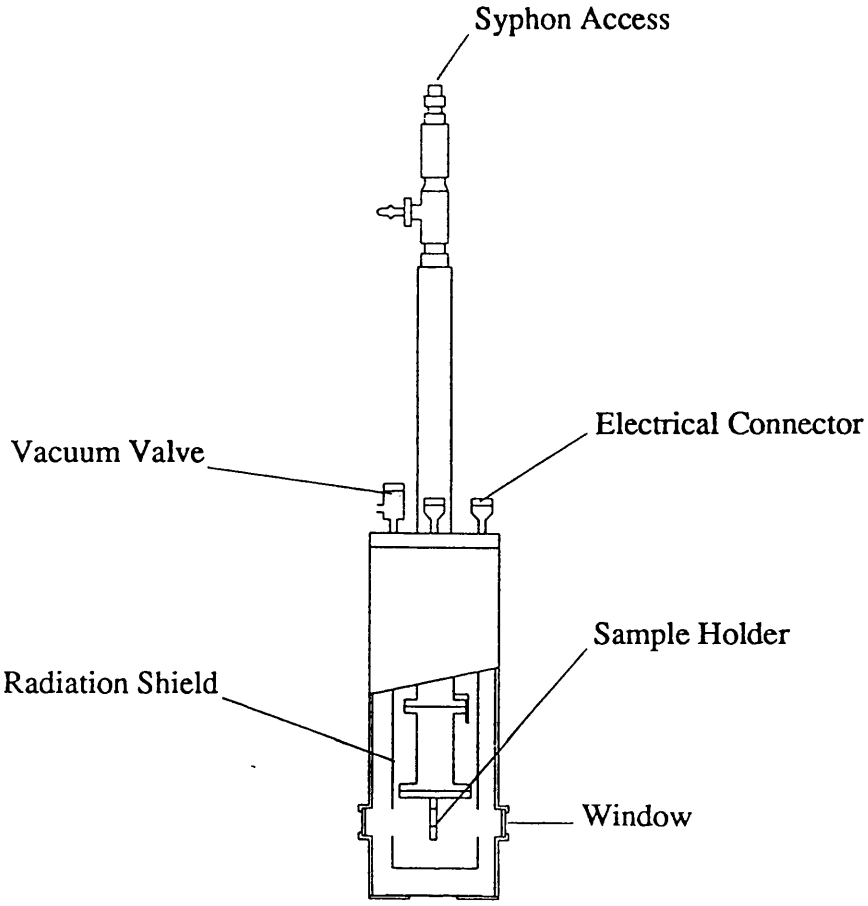

FIGURE 4.4 Continuous flow cryostat.

The detector mount was attached to a gold plated copper sample holder which was in turn bolted to the heat exchanger. An indium seal between the heat exchanger and the detector holder ensured that there was a good thermal link across

the joint. The detector was in a vacuum environment and was surrounded by a gold-plated copper radiation shield and an outer vacuum case.

The cryostat could be fitted with up to five windows, four radial and one axial. During these experiments only one radial window was used. One of the other window spaces was used to mount electrical connections through to the detector, and the others blanked off. The temperature of the detector was monitored with a cryogenic linear temperature sensor (C.L.T.S.).

4.6 Biasing circuit

The d.c. biasing circuit used within the cryostat is shown in figure 4.5.

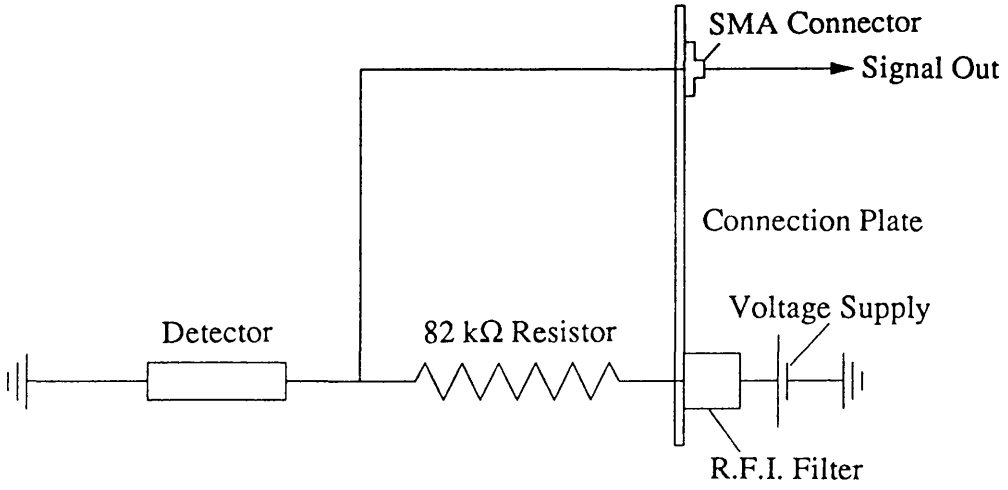

FIGURE 4.5 Biasing circuit and connection plate.

The resistor was placed inside the cryostat to form a cooled constant current source for biasing the detector. External connections were made to the detector and bias resistor via a single structure called the connection plate, shown in figure 4.5. The detector signal passes through a SMA flange mounted onto the connection plate. The d.c. bias voltage enters through an ERIE series 1200 RFI suppression filter which is screwed into the connection plate and bonded into position using epoxy adhesive.

The connection wires from the electric light bulb used to illuminate the detector were heat sunk onto the central tube, before being attached to a multi-pin electrical connector on the centre tube of the cryostat. The leads were then heat sunk on to the upper part of the centre tube before being connected to one of the feedthroughs on the top plate of the cryostat.

4.7 Quasi-Optical design

A quasi-optical system was designed to guide the radiation beam from the oscillator and focus it into the detector feedhorn. The quasi-optical system used is shown in figure 4.6. The system consisted of two types of high density polytetrafluoroethylene (P.T.F.E) lens.

The first type of lens, where both faces have an equal radius of curvature, was used to guide the radiation. The lens

focused the beam, to a beam waist at one focal length in front of it. Each guiding lens was positioned two focal lengths from the previous one.

The second type of lens had a face with a smaller radius of curvature. The lens was used to focus the beam to a smaller beam waist just inside the detector waveguide. The beam waist diameter required was 0.6 that of the feedhorn diameter.

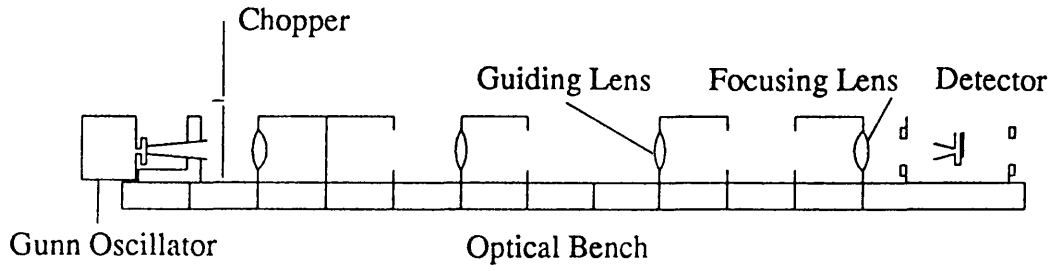

FIGURE 4.6 Quasi-optical system.

The lenses were mounted in brass blocks which had location pins, designed for use on a grid system. The optical bench was designed to give the option of adding another radiation beam for heterodyne experiments should it be required.

4.8 Results

4.8.1 Cyclotron resonance response

Radiation was detected from a 98 GHz Gunn oscillator. Figure 4.7 shows the trace taken of the detector response against

time, as the magnet current was adjusted to locate the cyclotron resonance peak.

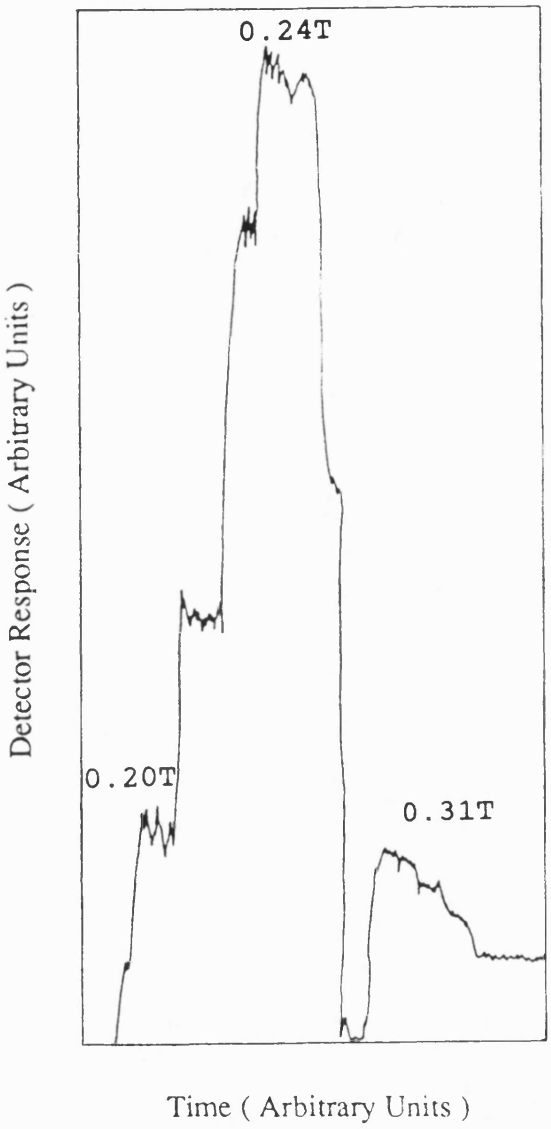

FIGURE 4.7 Detector response at various magnetic field strengths.

Figure 4.8 shows the corresponding plot of the variation of detector response with magnetic field strength.

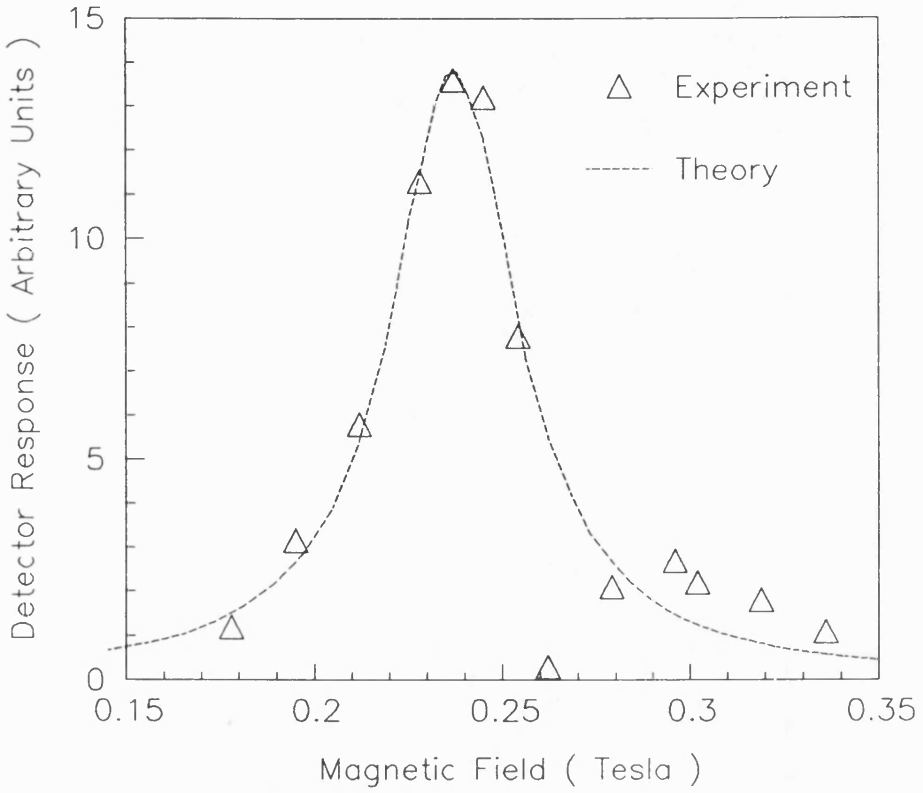

FIGURE 4.8 Photoconductive cyclotron resonance signal produced by a 98 GHz Gunn oscillator.

There is a strong detection of the 98 GHz signal at a magnetic field of 0.241 T, corresponding to the expected value of 0.239T. The photoconductive cyclotron resonance signal was fitted to the classical equation:-

$$\sigma = \frac{1 + [\omega^2 + \omega_c^2]\tau_m^2}{[1 + [\omega^2 - \omega_c^2]\tau_m^2]^2 + 4\omega_c^2\tau_m^2} \qquad 2.47$$

The dashed curve in figure 4.8 shows the curve deduced using the fitting parameter τ_m= 1.9 x 10^{-11} s and normalising to the maximum peak value. Once again the observed lineshape observed appears asymmetric, with the resonance frequency shifted to the high frequency side.

Figure 4.9 shows the change in the detector's resistance as it was cooled from room temperature to 4.2K in the dark.

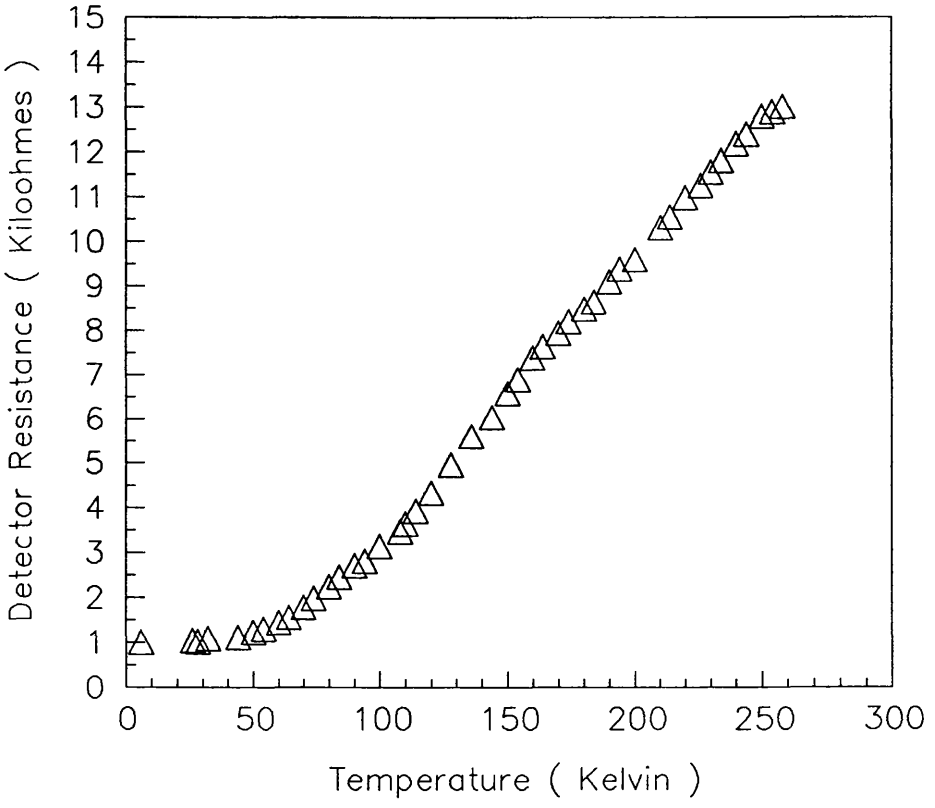

FIGURE 4.9 Variation of detector resistance as a function of temperature.

4.8.2 Variation of detector response with temperature

Figure 4.10 shows the trace taken of the detector response against time as the detector was allowed to warm up from 4.2 K to room temperature, while tuned to detect the 98 GHz signal.

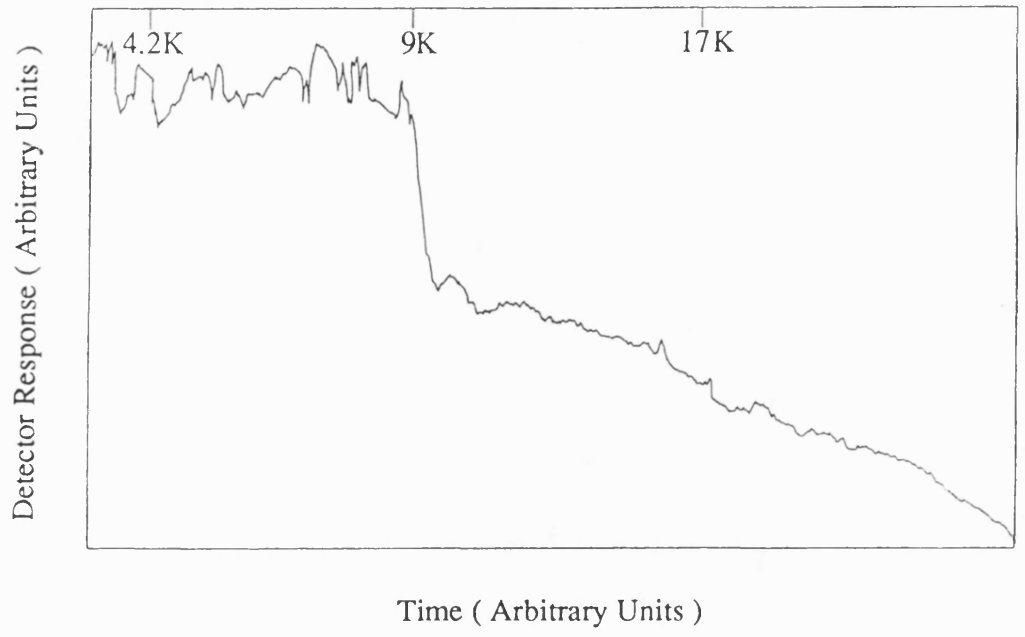

FIGURE 4.10 Detector response as detector allowed to warm up.

Figure 4.11 shows the corresponding plot of the variation of detector response with temperature.

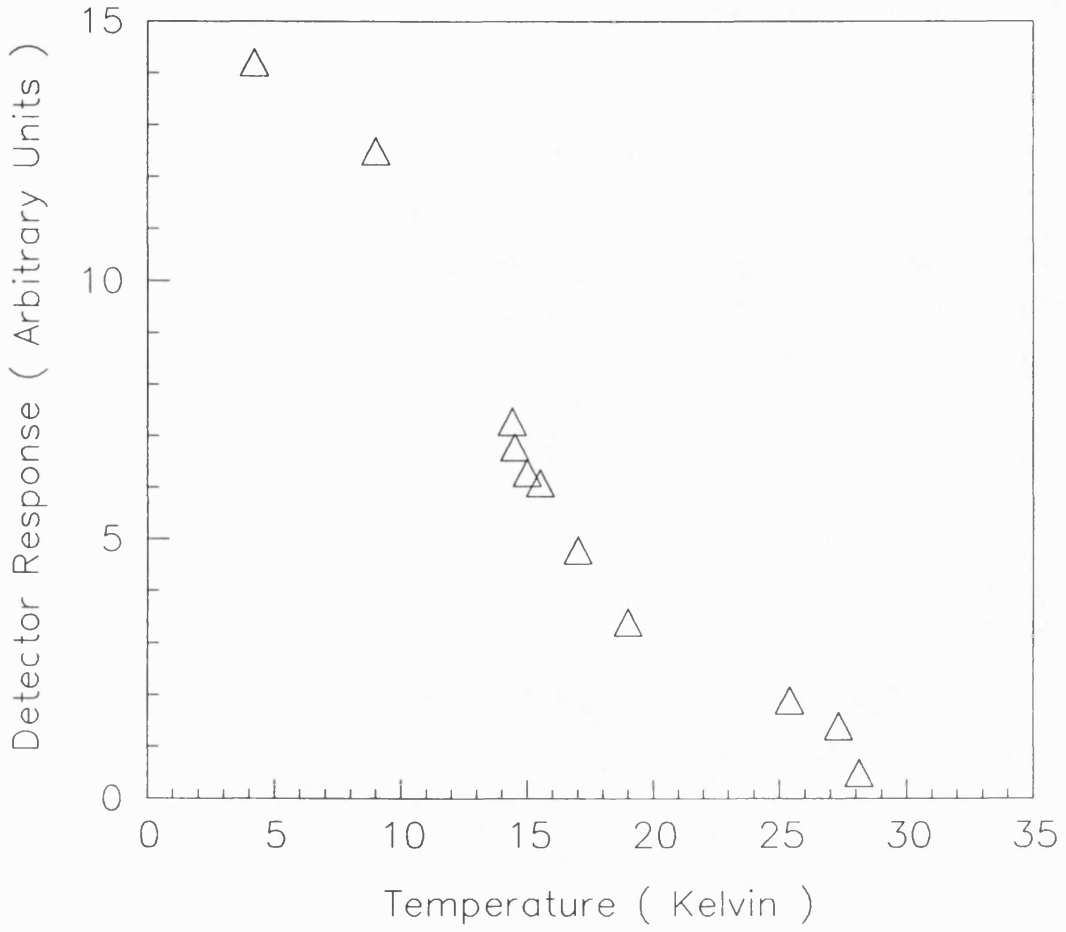

FIGURE 4.11 Detector response as a function of detector temperature.

The detector response can be seen to fall slowly for temperatures up to approximately 9 K and then fall rapidly, disappearing at approximately 30 K. The Landau levels have an energy separation of 0.41 meV for a cyclotron resonance frequency of 98 GHz. Therefore once the detector has reached

a temperature of 4.7 K some of the electrons within the system will have enough thermal energy to make the transition from one Landau level to the next. Once this occurs the signal intensity will start to disappear within the noise of the system.

4.8.3 Variation of detector response with light

The detector was exposed to visible light while at 4.2 K, using the light bulb attached to the detector mount. The two dimensional electron gas carrier concentration was therefore increased by virtue of the persistent photoeffect.

The detector was tuned to detect the 98 GHz signal. The variation of the detector response as it was also irradiated with visible light is shown in figure 4.12. The output first rose, then fell to approximately zero, and then rose again. This could be explained by reference to figure 2.11. As the detector is exposed to a pulse of light, the two dimensional electron gas carrier concentration increases, and therefore the Fermi level rises. The Fermi level will sweep through the Landau levels causing an oscillation in the detector resistance, as in the Shubnikov de Haas oscillations described in section 2.5.2. Further work is required to verify this.

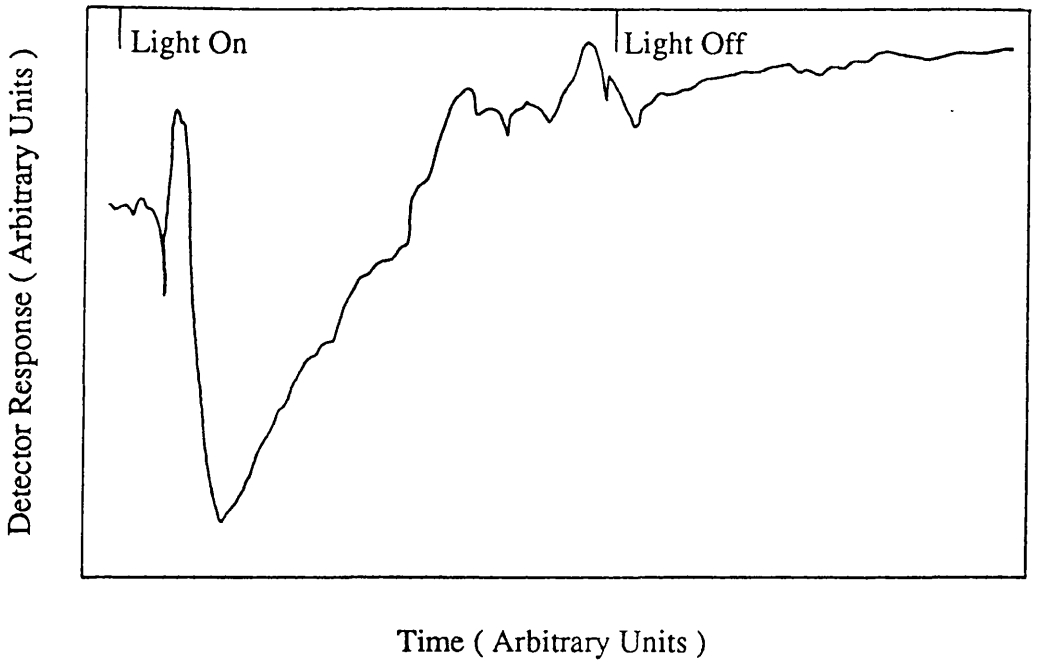

FIGURE 4.12 Variation of detector response while irradiated with visible light.

The variation of detector response with Gunn oscillator output power was measured both before and after irradiation with visible light. Figure 4.13 shows that the detector response approximately doubled after exposure to light.

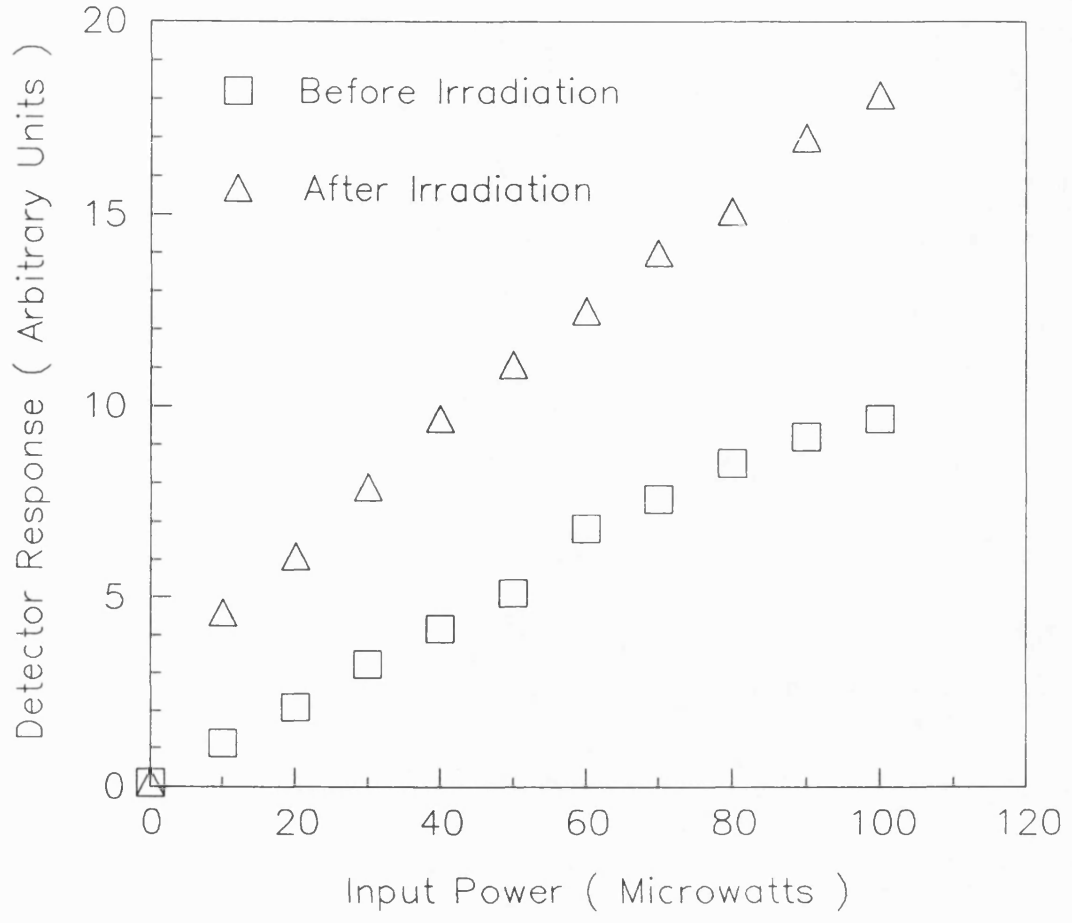

FIGURE 4.13 Variation of detector response as a function of the Gunn oscillator power before and after irradiation with visible light.

The illumination of the detector would have caused an increase in the two dimensional electron density. The observed effect may be due to the Fermi level moving from a position within

a Landau level to one between Landau levels. From figure 2.11(b) it can be seen that when the Fermi level lies between Landau levels, one Landau level is completely filled, while the next higher one is empty. There is a vanishing of resistance due to the fact that no interlevel scattering can occur in this situation. Irradiation by electromagnetic waves of the cyclotron frequency photoexcites carriers to the higher Landau level. The photoexcited carriers along with the empty states left behind in the lower Landau level increase the scattering and therefore a strong increase in resistivity is observed. When the Fermi level lies within a Landau level however, as shown in figure 2.11(c), the Landau level is only half filled. In this situation a weaker relative change in resistivity will be observed. The Fermi level may have moved from the second situation to the first. This could mean that detectors can be optimised for a certain frequency if so desired by varying the two dimensional gas concentration by controlled irradiation with light.

4.8.4 Variation of detector response with d.c. bias

One difference that was found between the results taken at Oxford and those taken at Bath occurred in the variation of detector response with d.c. bias. Figure 4.14 shows the plot of detector response as a function of d.c. bias for the Bath results.

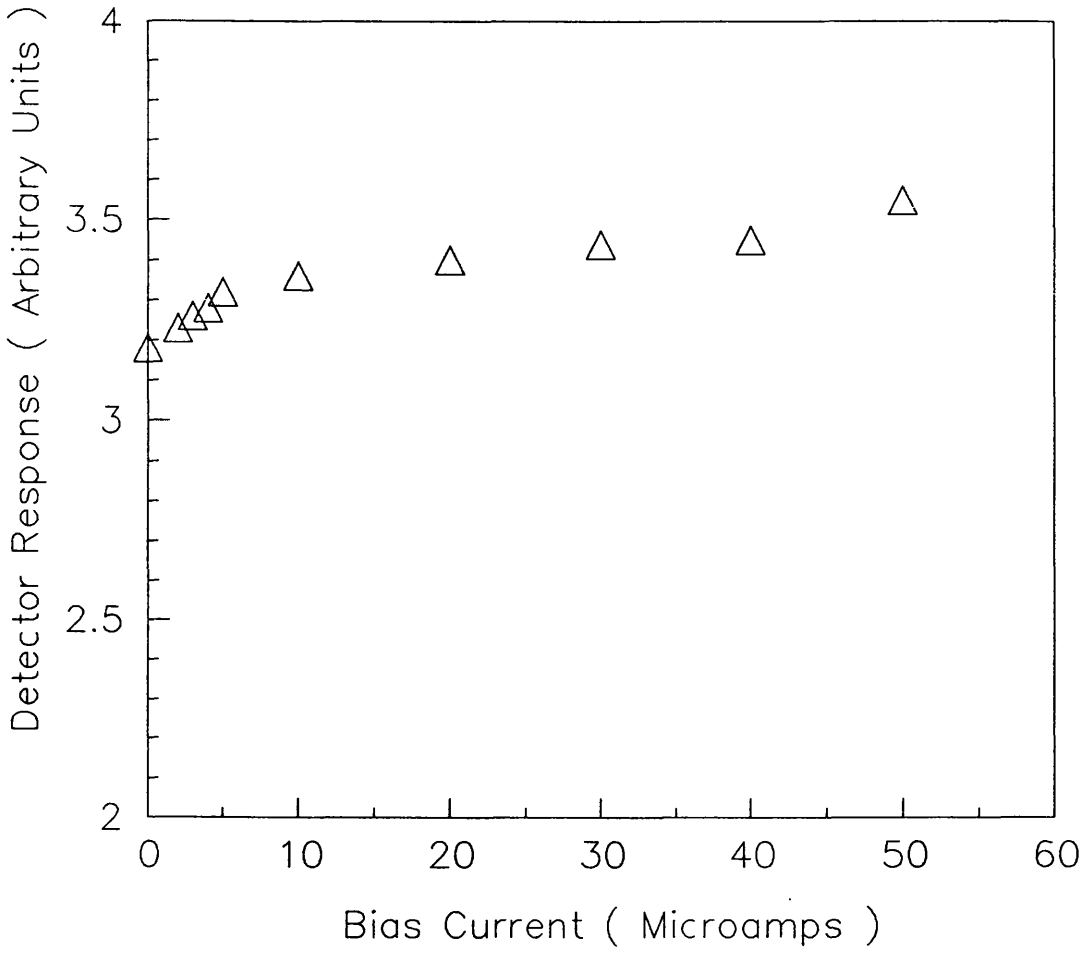

FIGURE 4.14 Detector response as a function of d.c. bias.

It can be seen that these results differ from the corresponding Oxford results, shown in figure 3.14. Two explanations could be used to explain this difference. It could be the contacts to the detectors that were actually causing the change. The other possibility was that the thermal gradient across the detector in this system was greater than

in the Oxford one. An internal bias current may therefore already be present taking the detector to its previously reached saturation point, without the need for an additional external bias current.

CHAPTER 5 BATH COMPACT DETECTOR SYSTEM

5.1 Measurement system

Having achieved a working system at Bath, a need for a more compact detector system was recognized. The new detector system incorporated two small permanent magnets, with the detector lying between them. Variation of the magnetic field strength applied to the detector was achieved be adjusting the distance between the magnets. The new detector system also contained a variable backshort, to optimise power absorption by the detector. The detector itself was mounted across stripline filters. The whole detector system was fitted into a standard Infrared Laboratories HD3 cryostat, the type of which are frequently used with current detectors.

5.2 Detector

The detector that was studied with this system is shown in figure 5.1. For the detector, at 4.2 K in the dark, the electron concentration in the two-dimensional gas was approximately 1.5×10^{11} cm^{-2}, with a mobility of 1×10^{6} $cm^{2}v^{-1}s^{-1}$. The carrier density could be increased to approximately 3×10^{11} cm^{-2} by using the persistent photoconductivity effect. As with detectors A and B the second confined level remains unoccupied over the whole carrier density.

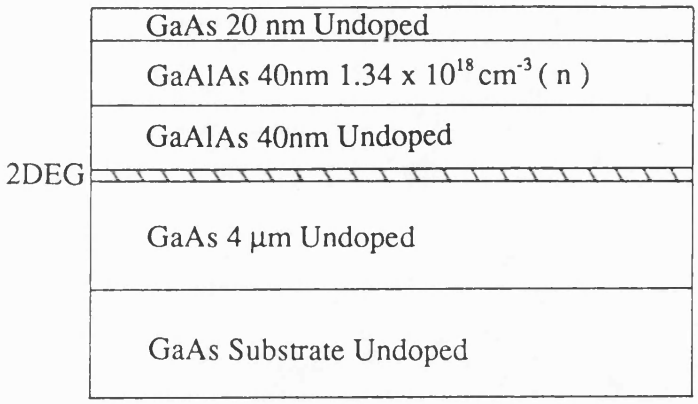

FIGURE 5.1 Sequence of layers grown for the detector.

5.3 Detector mount design

The detector mount was designed to incorporate both a movable backshort and the two magnets. Figure 5.2 shows a diagrammatic representation of the detector mount.

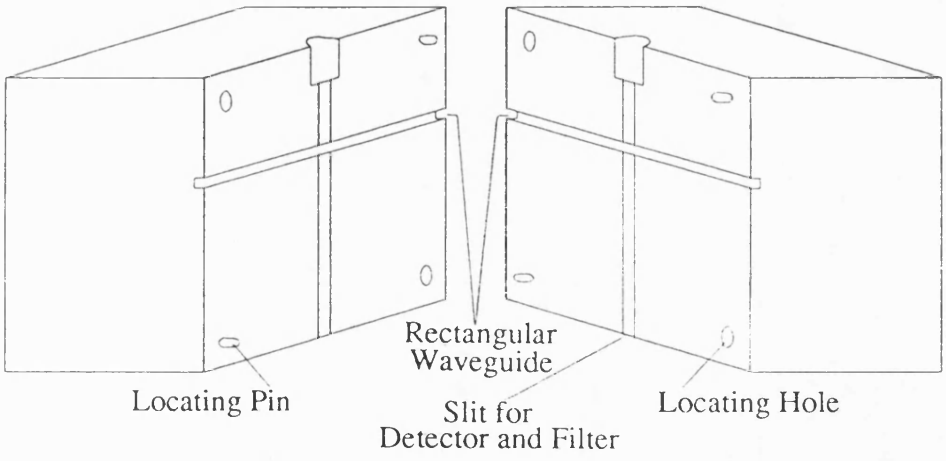

FIGURE 5.2 Detector mount.

A stripline channel ran down across a rectangular waveguide, with an insert for a SMA connector. The block fitted together using locating pins and connection screws. The scalar feedhorn and backshort pin located onto the front and back of the mount respectively. Two threaded holes were located on the sides of the detector mount, centralised on the detector position. These can be seen in figure 5.3.

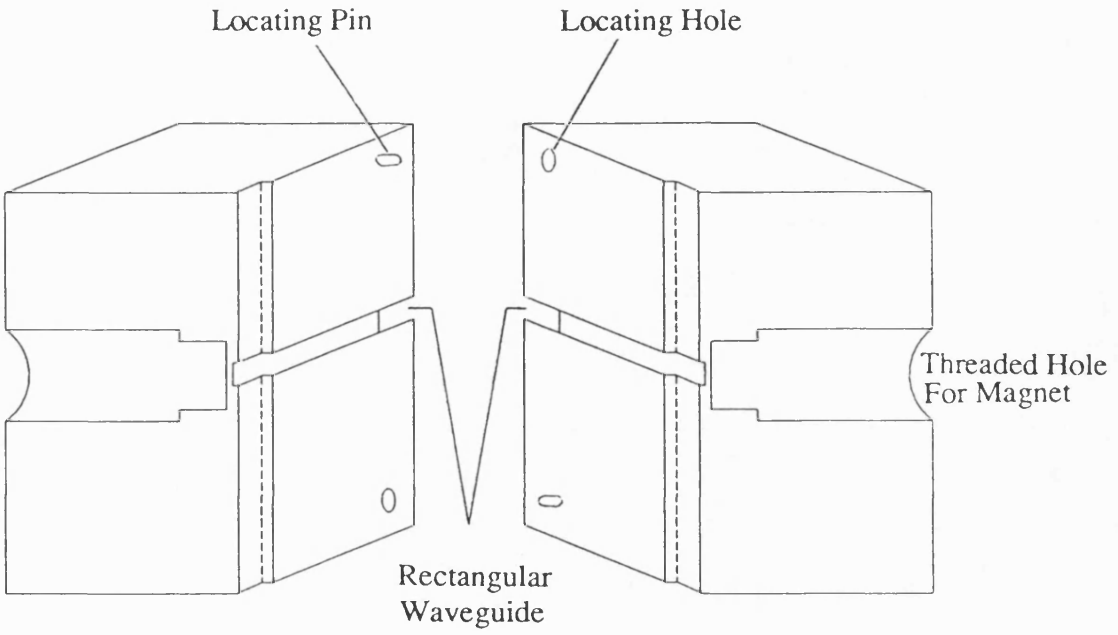

FIGURE 5.3 Cross sectional view of detector mount.

The threaded holes were used to guide the magnets, in their holders, towards the detector and thus vary the magnetic field exerted onto it.

5.3.1 Magnetic tuning

Two samarium cobalt (SmCo) magnets were used to tune the magnetic field. Each of these were mounted in a specially designed holder, as shown in figure 5.4, and bonded into position using an epoxy adhesive.

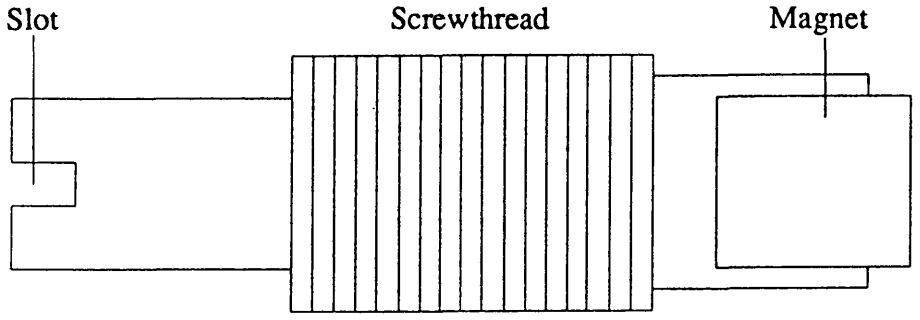

FIGURE 5.4 Magnet holder.

The main barrel of the holder was finely threaded to match that of the locating holes on the side of the detector mount. The holders could then be screwed into the detector mount with high precision. The holders were designed so that even when they have been fully screwed in, the magnets remained 0.1 mm from the end of the locating holes, so as not to crush them.

5.3.2 Adjustable backshort

The adjustable backshort was designed for use with the detector mount. It consisted basically of a Johanson

microwave tuning element enclosed in a mount, with a flange fitting soldered to it. The tuning element had 64 threads per inch and therefore allowed for very accurate positioning of the backshort.

5.3.3 Tuning

To enable both the magnets and the backstop to be tuned while the detector was at 4.2 K, three rotary shaft feed-throughs were mounted to the cryostat. These are shown in figures 5.5 and 5.6.

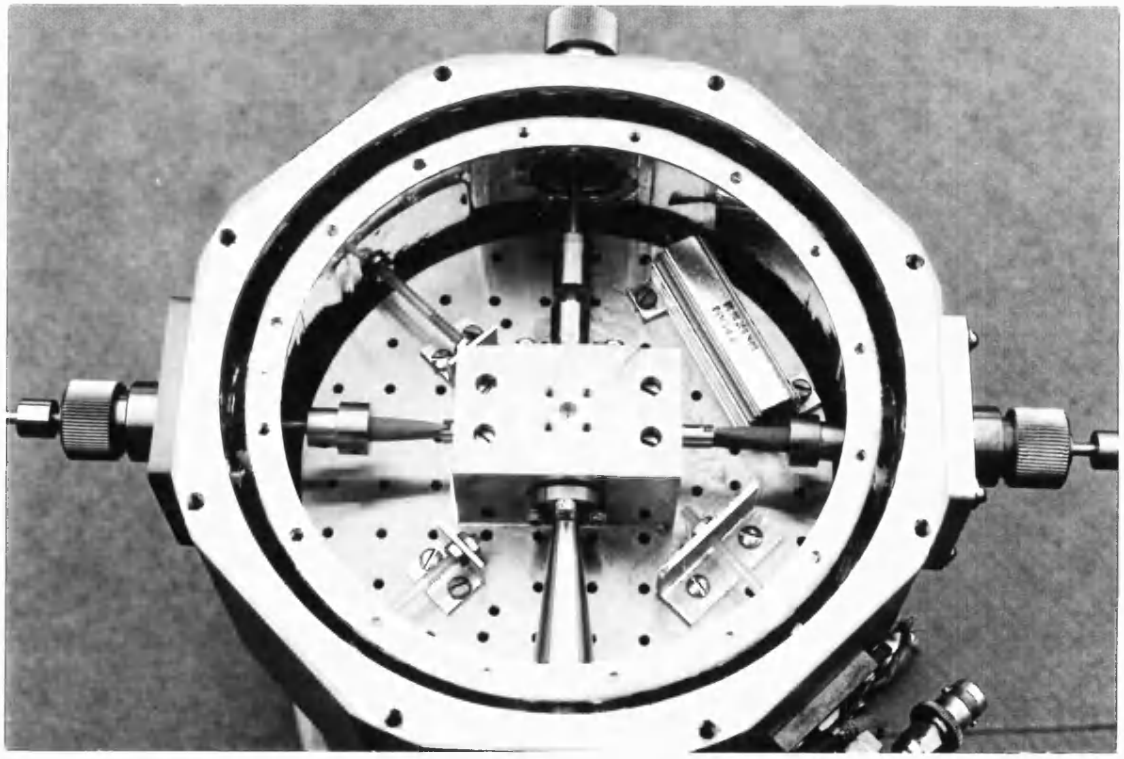

FIGURE 5.5 Tuning system.

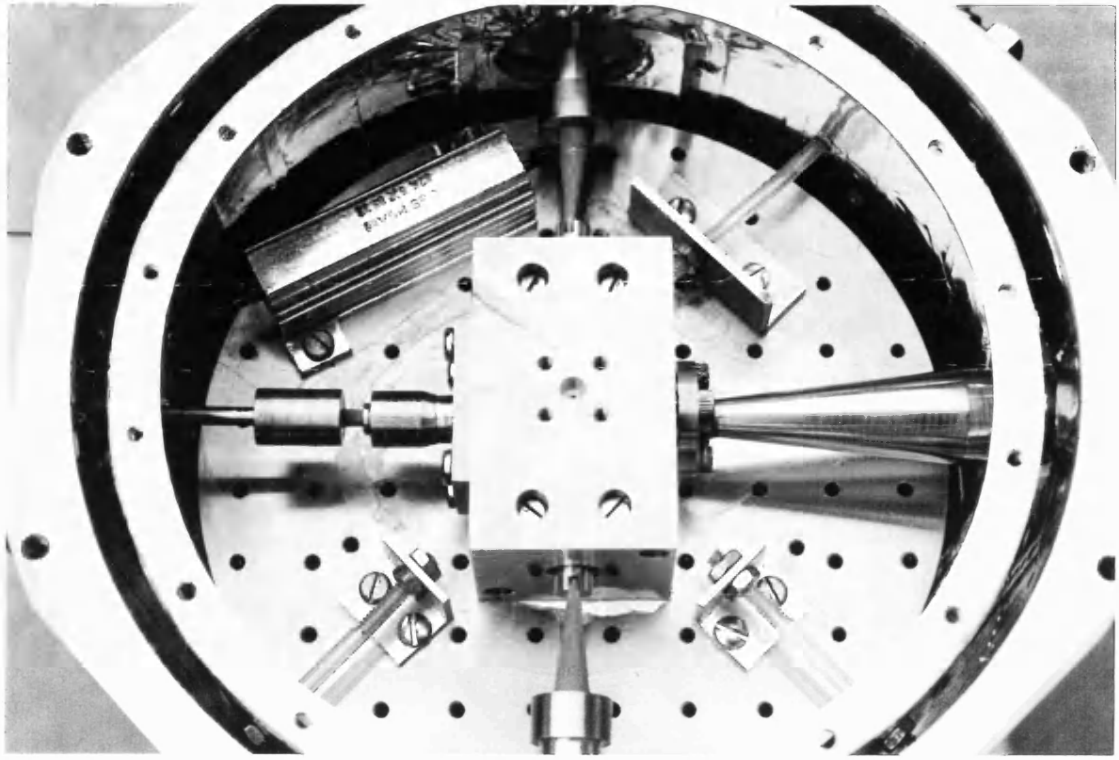

FIGURE 5.6 Close up of tuning system.

Tufnol screwdriver heads were attached to the feedthroughs inside the cryostat using a clamping system, shown in figure 5.7. Tufnol was used because of its low thermal conductivity. Once any necessary tuning had been carried out the feedthroughs were drawn away from the detector mount to avoid heat loading the system.

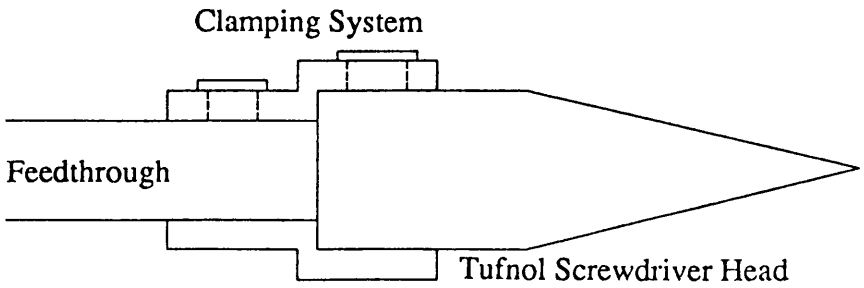

FIGURE 5.7. Adjustment screwdriver heads

5.3.4 Filter design

The detector was mounted across a low pass filter. The filter allowed a d.c. bias to be applied to the detector, without allowing any of the radiation incident along the waveguide to escape along the filter. The suspended stripline low-pass filter was based upon a design by Lidholm [1978], and was scaled to produce a cutoff frequency of around 80 GHz. A short was achieved at the ends of the filter by terminating the stripline at a calculated distance (see appendix A). The basic filter configuration is shown in figure 5.8, with low impedance sections constituting shunt capacitances to ground and high impedance sections constituting series inductances (see appendix A).

The filters were fabricated at British Aerospace. Essentially, a layer of chrome and then gold is evaporated on to

a fused quartz substrate. The actual filter configuration is then etched using photolithographical processing. Finally the filters are plated with a layer of gold.

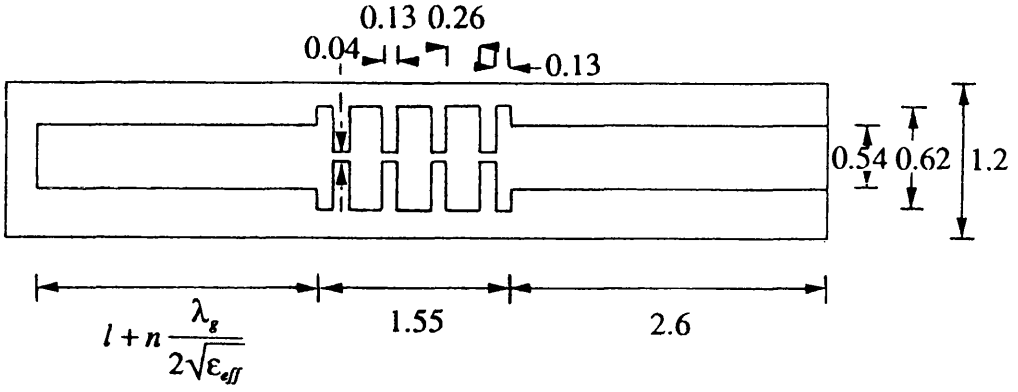

Figure 5.8 Low pass stripline filter (all measurements are in mm).

5.4 Mounting of the detector

Initially the detector had to be etched down from a thickness of 0.25mm so as to lie flush within the stripline channel of depth 0.225mm. It was important that only the GaAs substrate at the back of the detector was etched so that the heterojunction itself was not damaged. To achieve this the top of the detector was masked off using black wax. A small piece of black wax was placed onto a glass slide, this was then heated carefully until the wax began to melt. The wax was spread a little and allowed to cool. The detector was then gently pressed onto the wax. The slide was heated

once more, and as the wax melted it was pressed up the sides of the sample until only the bottom remained visible. After the wax had cooled the slide was submerged in a GaAs etch consisting of 50% ammonium hydroxide (NH_4OH) and 50% hydrogen peroxide (H_2O_2). The thickness of the detector was checked at intervals by dissolving the wax with 1.1.1. trichloroethane and measuring under a microscope. The process was then repeated until the detector had reached its required size.

Gold connecting wires were contacted to one end of each of the two filters. A small piece of low melting point indium solder was placed with some flux at the required position. The filter was than carefully heated on a hot plate. As soon as the solder had melted the filter was dropped into distiled water. The top part of the indium was then cut away to achieve a flat surface. A groove was then cut and a piece of gold wire laid in it. A small amount of flux was added and the filter was heated again. Once the solder had melted the filter was dropped into distiled water.

The detector was mounted onto the filters using silver epoxy applied to the Au:Ge:Ni contacts. As low melting point indium solder had been used for the connection of gold wires to the filters, the usual curing temperature of 150^{o}C could

not be used. However it was found that satisfactory results could be achieved by curing at a temperature of 80°C for 18 hours.

The detector and filters were then placed in the stripline channel as shown in figure 5.9.

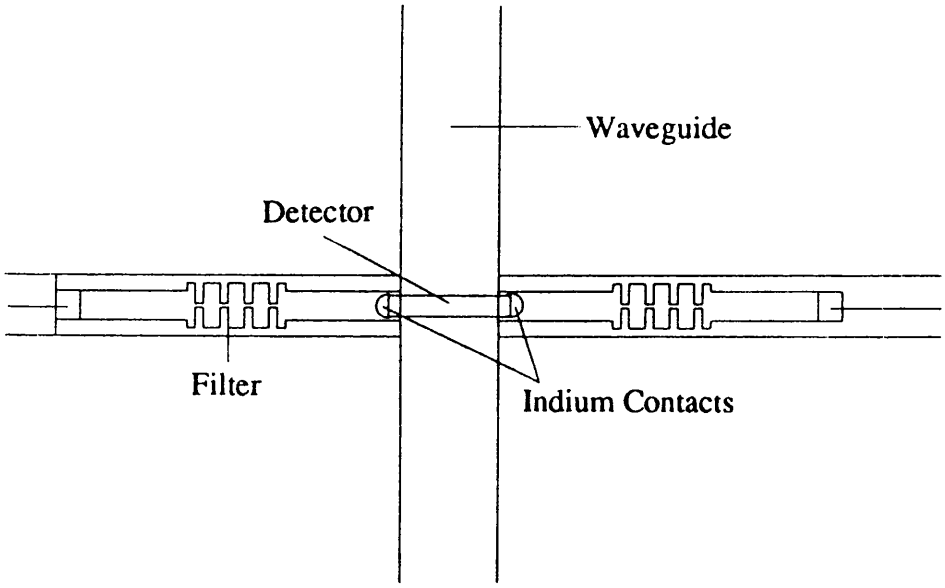

FIGURE 5.9 The mounted detector.

The gold wire from one filter was earthed at a distance of half a wavelength from the end of the filter using indium solder. The wire from the other filter was glued into place, care being taken that a short was not made to the detector mount. A photograph of the mounted detector is shown in figure 5.10.

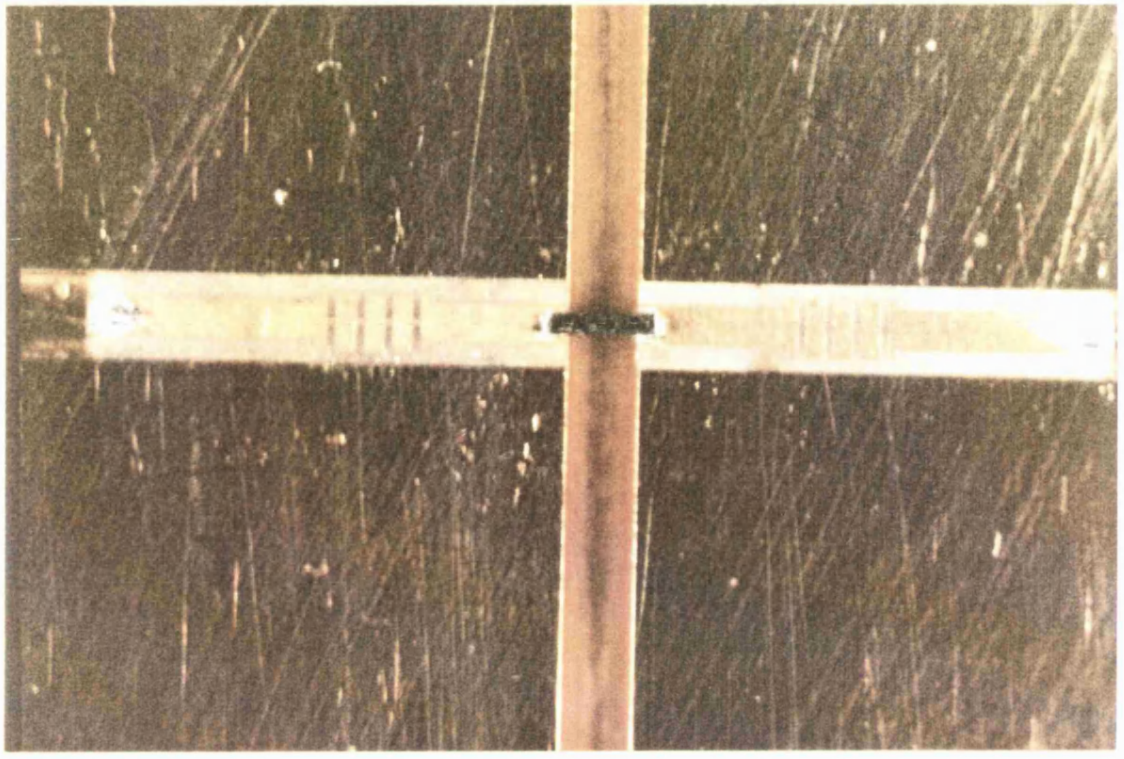

FIGURE 5.10 Photograph of the mounted detector.

5.5 Cryogenic apparatus

The cryostat used to cool the detector is shown in figure 5.11. It was an Infrared Laboratories HD3 cryostat which essentially consisted of a reservoir of liquid helium and a reservoir of liquid nitrogen. The sample space was situated directly above the helium reservoir and was much larger than in the previous cryostats used. The helium hold times were enhanced by the use of super-insulation. The whole system was evacuated.

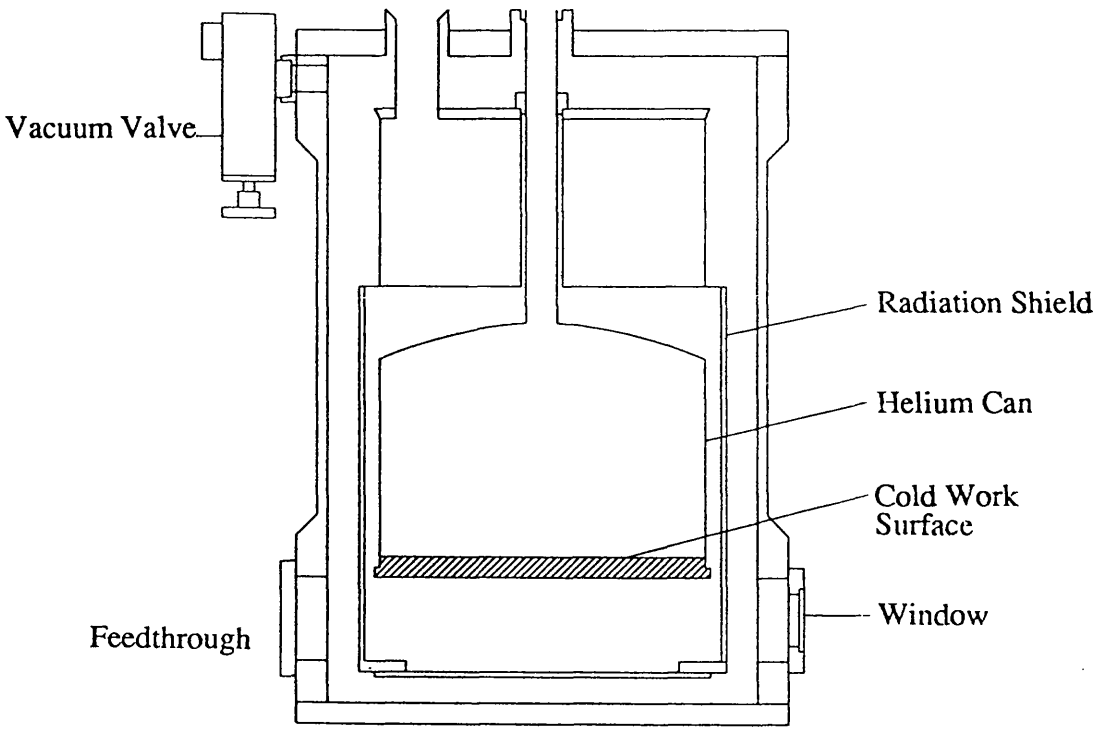

FIGURE 5.11 Infrared Laboratories HD3 cryostat.

5.6 Biasing circuit

The same d.c. biasing circuit was used in this system as in the previous system. This is shown in figure 4.5.

5.7 Quasi-optical design

The same quasi-optical arrangement was used in this system as in the previous system. This is shown in figure 4.6.

5.8 Results

5.8.1 Detection of a 98 GHz Gunn oscillator

Radiation was detected from a 98 GHz Gunn oscillator and a 113 GHz klystron oscillator. The photoconductive cyclotron resonance signals observed are shown in figure 5.12.

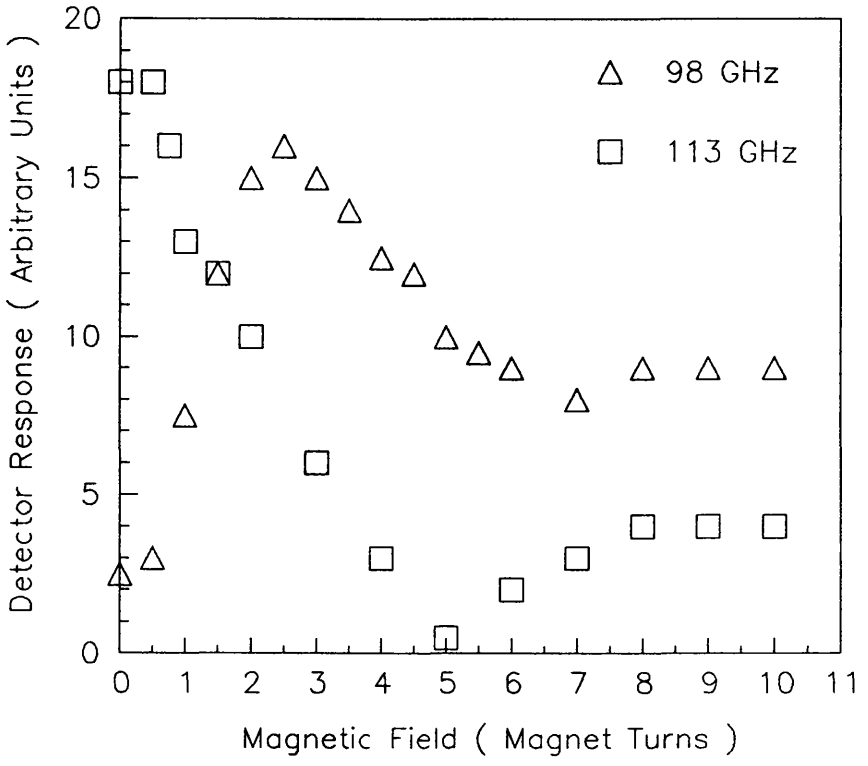

FIGURE 5.12 Photoconductive cyclotron resonance signal produced by a 98 GHz Gunn oscillator and a 113 GHz klystron oscillator (magnetic field decreases with increasing number of magnet turns).

The 98 GHz resonance peak is clearly seen. The maximum magnetic field strength achievable, at this time, was not high enough to give a clear cyclotron resonance peak for the 113 GHz signal. All results were taken with the magnetic field tuned to the cyclotron resonance, with the backshort adjusted for maximum output, unless otherwise stated.

The detector response at the 98 GHz cyclotron resonance frequency peak, for three different d.c. bias currents is shown in figure 5.13. It can be seen that there is a large signal obtained under zero bias conditions, reaffirming previous results. The current-voltage characteristics of the detector were investigated on a curve tracer. The observed characteristics were linear. Any non-linearity observed would have implied that non-ohmic contacts had been produced. The linearity of the characteristics made it unlikely that the contacting process might be responsible for the zero bias signal. It is more probable that the detector was producing its own electronic current as discussed previously.

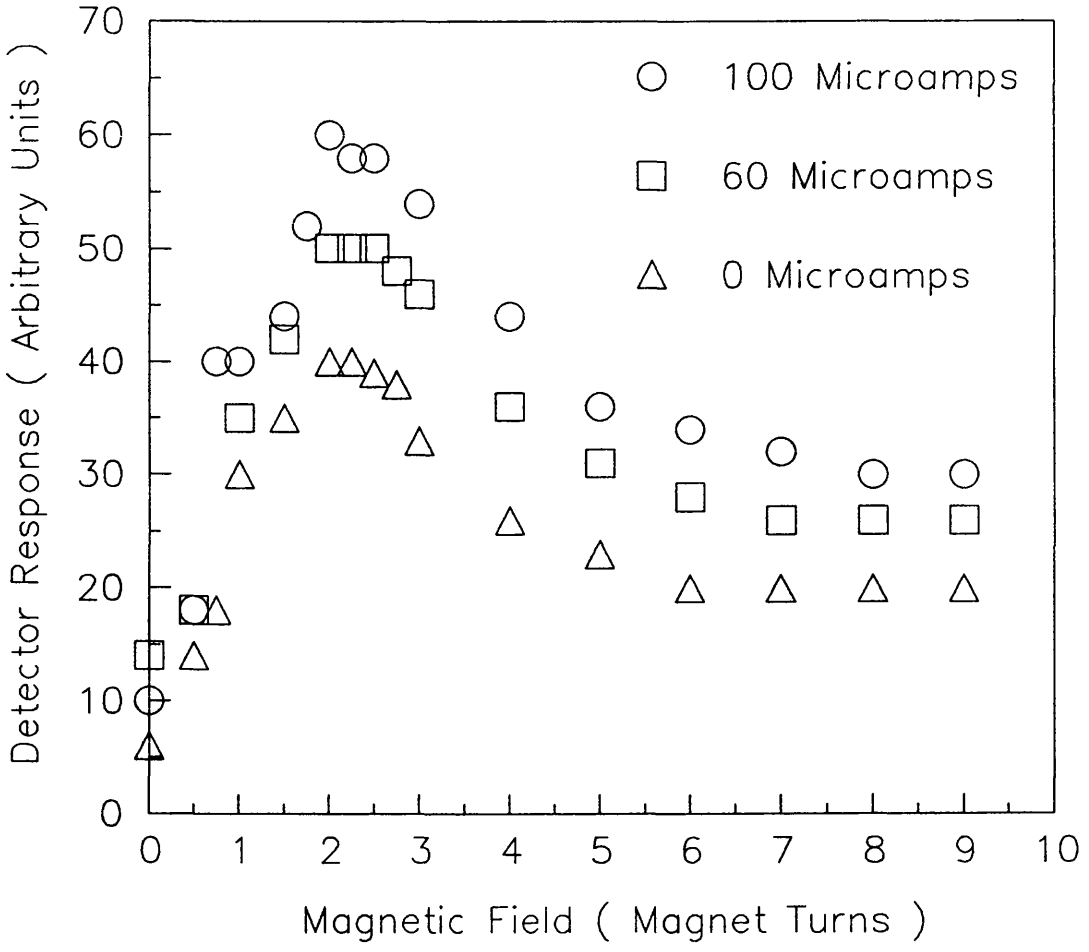

FIGURE 5.13 Photoconductive cyclotron resonance signal produced by a 98 GHz Gunn oscillator for three bias currents (magnetic field decreases with increasing number of magnet turns).

The variation of the detector response with the d.c. bias current is shown in figure 5.14.

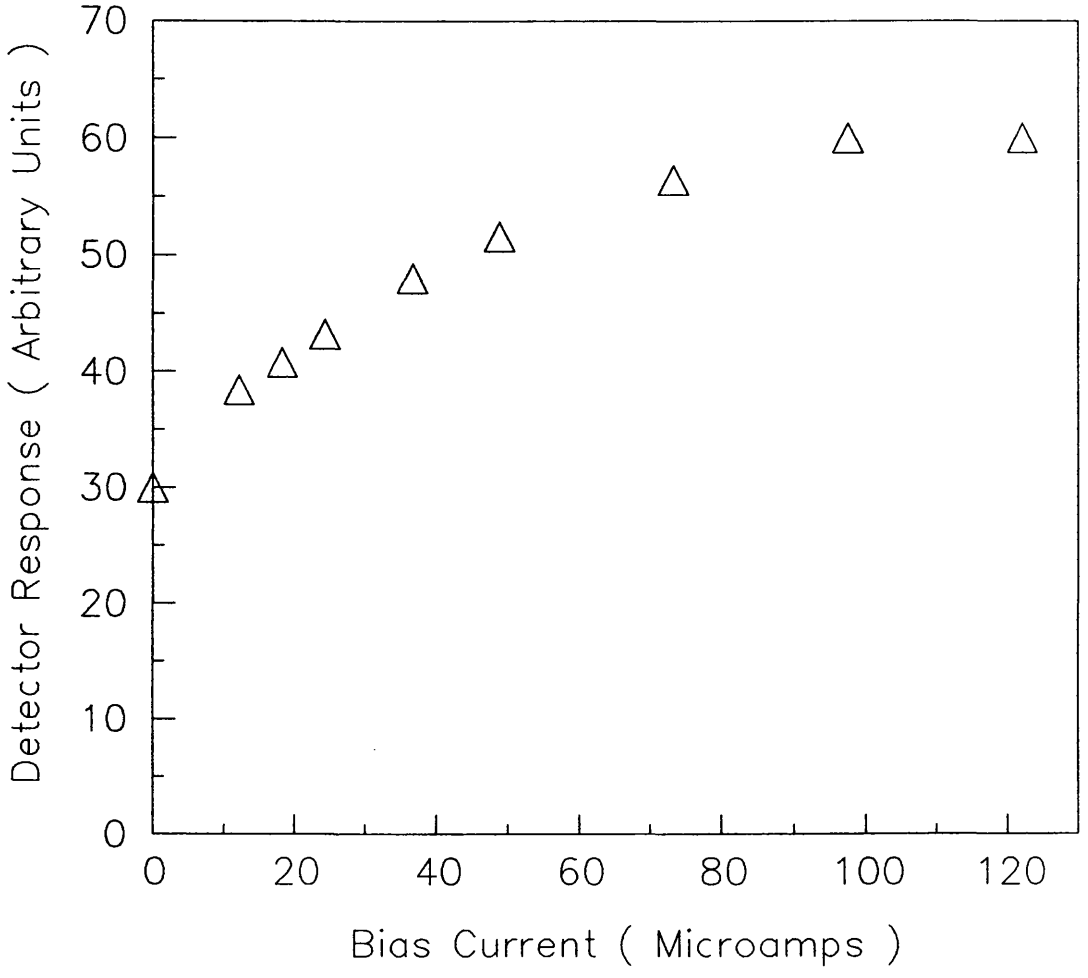

FIGURE 5.14 Variation of detector response with bias current.

The output can be seen to rise to a plateau at approximately 100 μA.

5.8.2 Detection of a 113 GHz klystron

The detection system was further modified to allow the magnets to be brought closer to the detector. The magnetic field achievable was therefore greater than previously possible. The photoconductive cyclotron resonance signal observed for the 113 GHz klystron is shown in figure 5.15.

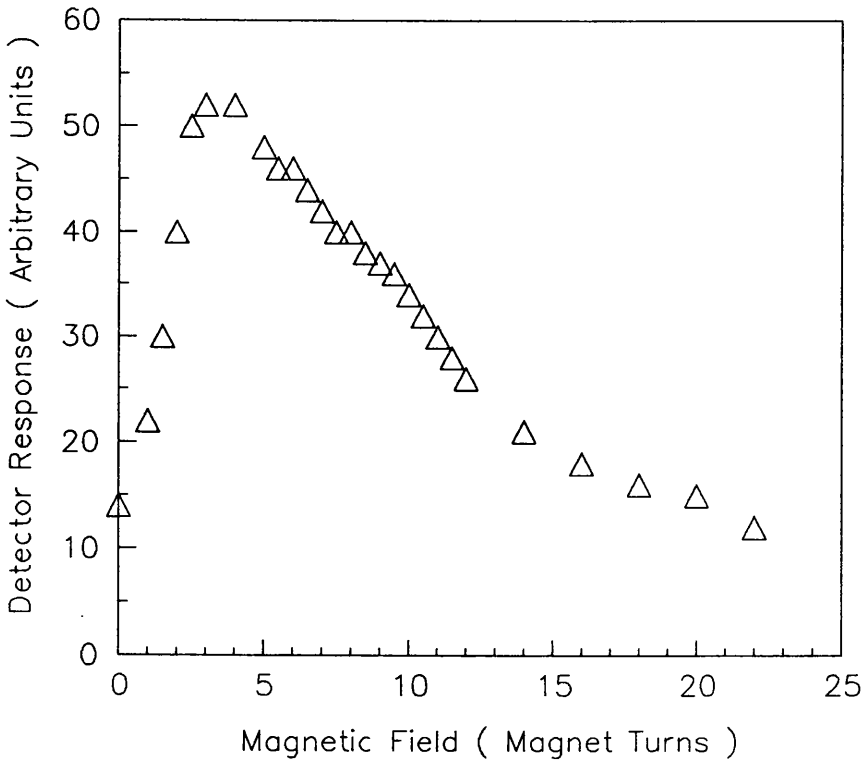

FIGURE 5.15 Photoconductive cyclotron resonance signal produced by a 113 GHz klystron oscillator (magnetic field decreases with increasing number of magnet turns).

The variation of detector response with backshort position is shown in figure 5.16.

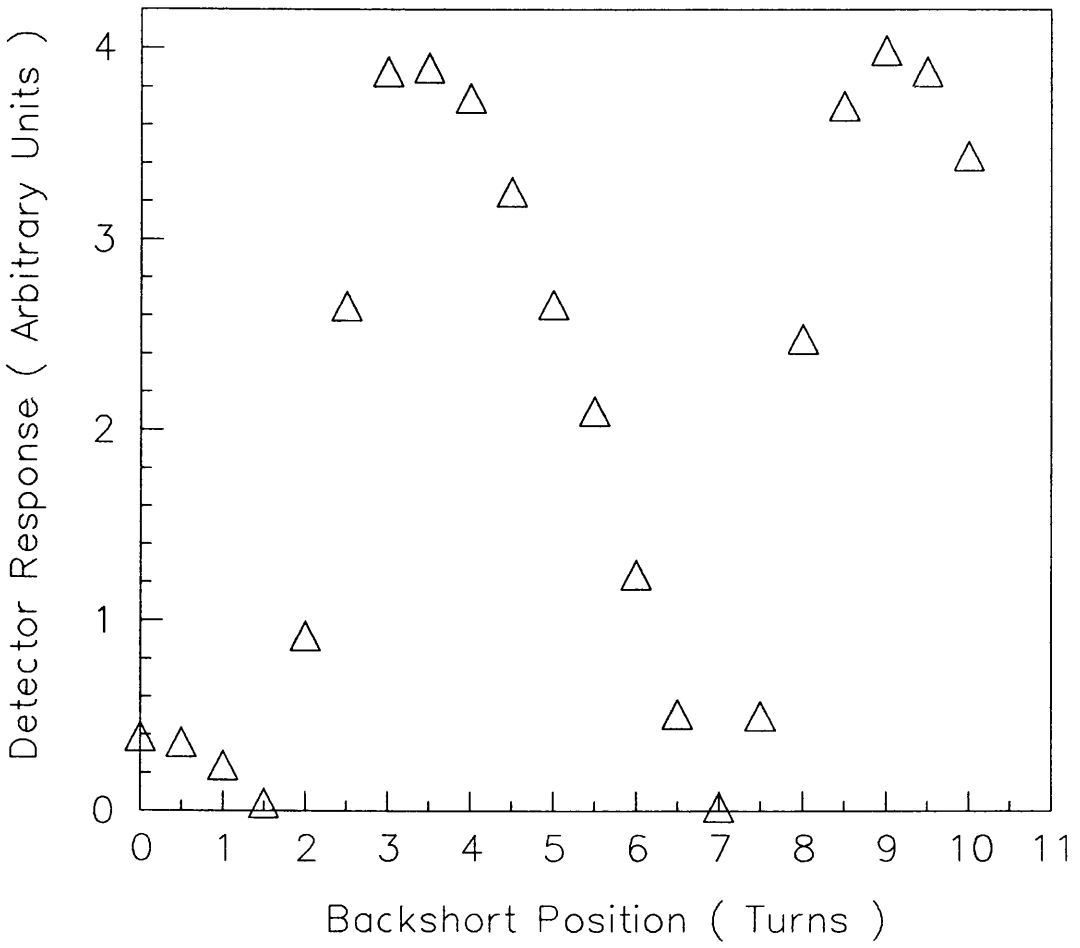

FIGURE 5.16 Variation of detector response with backshort position.

The results are taken at a cyclotron resonance frequency of 113 GHz. It can be seen that the detector response cycles through maximum and minimum values as the backshort position is varied. The cycling of the detector response is due to the variation of the power being absorbed by the detector. A peak in the absorbed power occurring every half a guide wavelength (see appendix A). The distance travelled by the backshort for ten turns of the adjustment screw was measured with a micrometer. From this measurement and figure 5.16, the guide wave length was found to be 3.917 mm. Substituting this value into equation :-

$$\lambda_{gu} = \frac{\lambda_o}{\sqrt{1-\left[\frac{\lambda_o}{2a}\right]^2}} \qquad 5.1$$

(see appendix A) gives the free space wavelength a value of 2.80 mm, corresponding to a frequency of 107 GHz.

The variation of detector response with oscillator power for bias current of 0 and 100 μA is shown in figure 5.17.

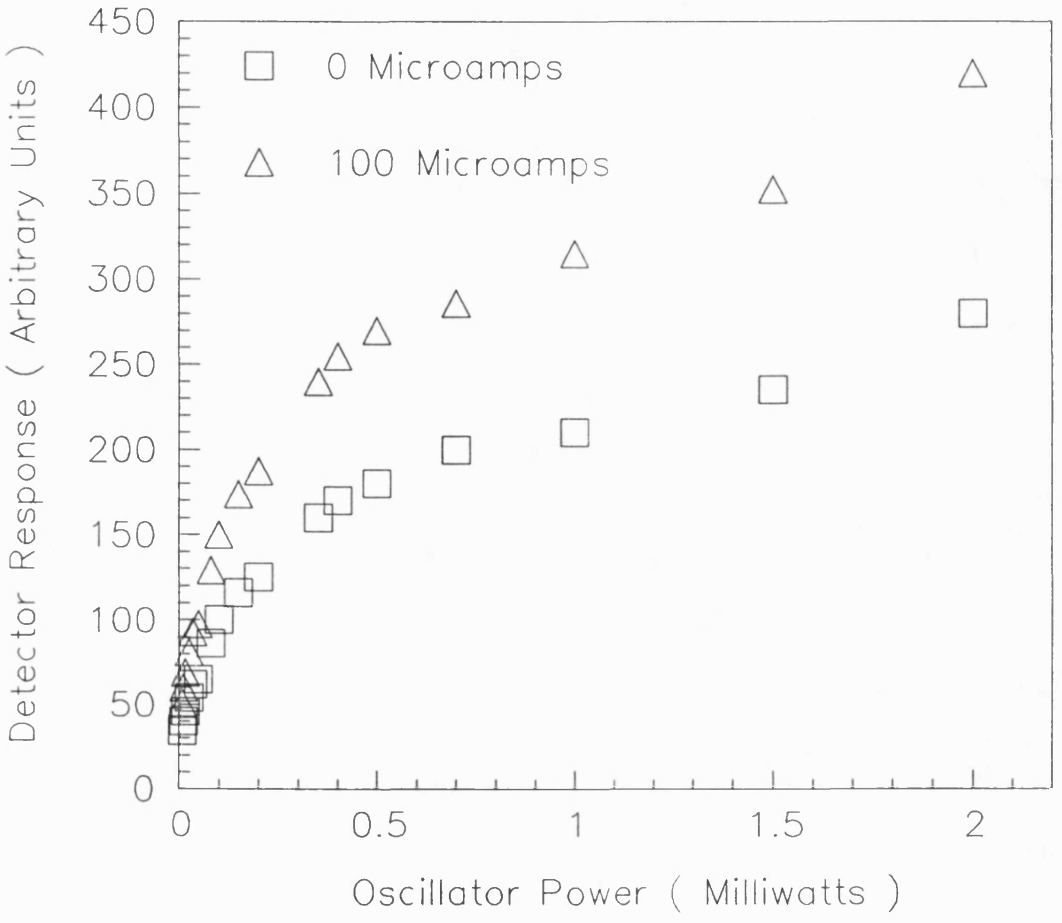

FIGURE 5.17 Variation of detector response with oscillator power for different bias currents.

The curves can be seen to initially rise steeply and then at a value of 600 μW become approximately linear with a shallow gradient.

5.8.3 Measurement of response time

The 113 GHz signal from the klystron oscillator was modulated using a pin modulator. Figure 5.18 shows the photoconductive cyclotron resonance peak at a modulation frequency of 2 MHz.

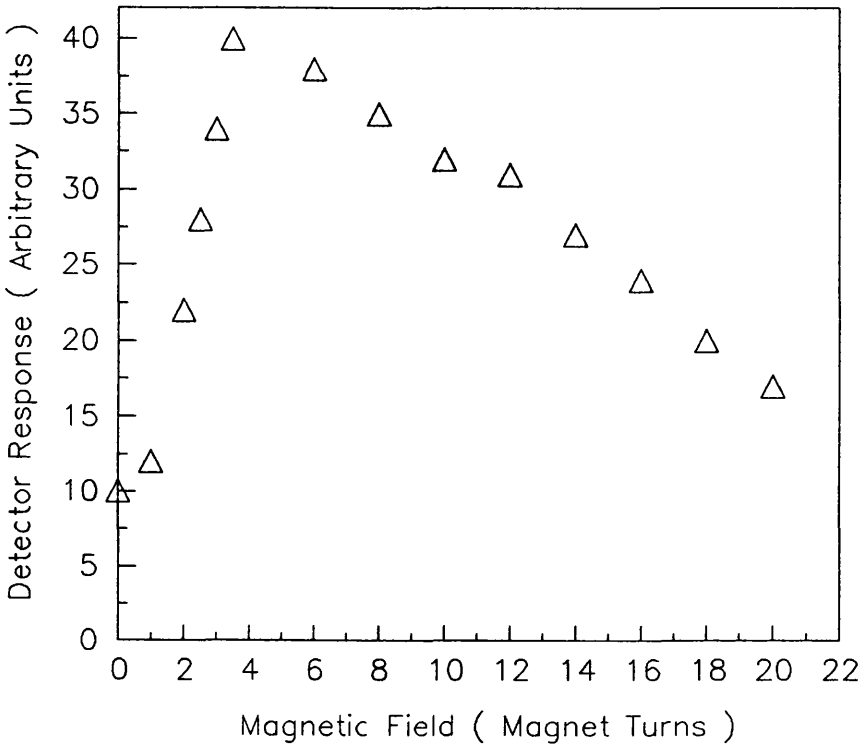

FIGURE 5.18 Photoconductive cyclotron resonance signal produced by a frequency modulated 113 GHz klystron oscillator (magnetic field decreases with increasing number of magnet turns).

The variation of detector response with the modulation frequency is shown in figure 5.19.

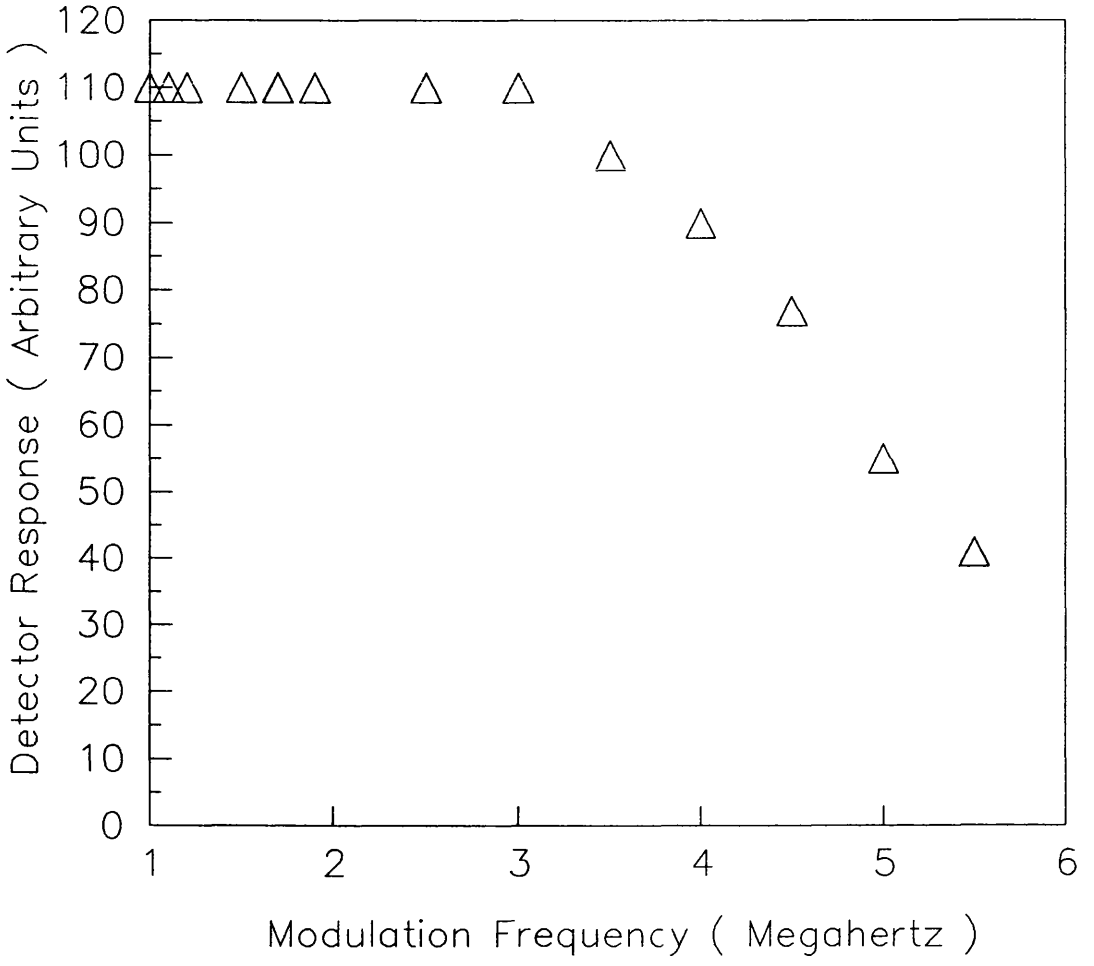

FIGURE 5.19 Variation of detector response with modulation frequency.

The detector signal can be seen to remain constant up to a modulation frequency of approximately 3 MHz, where it begins

to fall. It was postulated that the frequency response observed may have been the frequency response of the amplifier and not that of the detector itself.

To effectively eliminate the frequency response of the amplifying system, a new set of measurements were taken. The detector output was recorded as a function of modulation frequency. Then the output of a Schottky diode detector (of known frequency response) was monitored, for the same range of modulation frequencies, using the same measurement system. The $Ga_{1-x}Al_xAs/GaAs$ heterojunction detector response was then normalised to the Schottky diode detector output. The variation of the normalised detector response as a function of modulation frequency is shown in figure 5.20.

It can be seen that the normalised response remains fairly constant up to a frequency of approximately 4.7 MHz, at which it falls sharply. The modulation frequency corresponds to a detector time constant of 2×10^{-7} s. The time constant measured may still be that of the detector system and not of the detector itself. As the comparison was carried out between a Schottky diode detector and a cryostat mounted detector, it was possible that the frequency limitation was caused by the method of taking the signal from the detector to the cryostat connection plate.

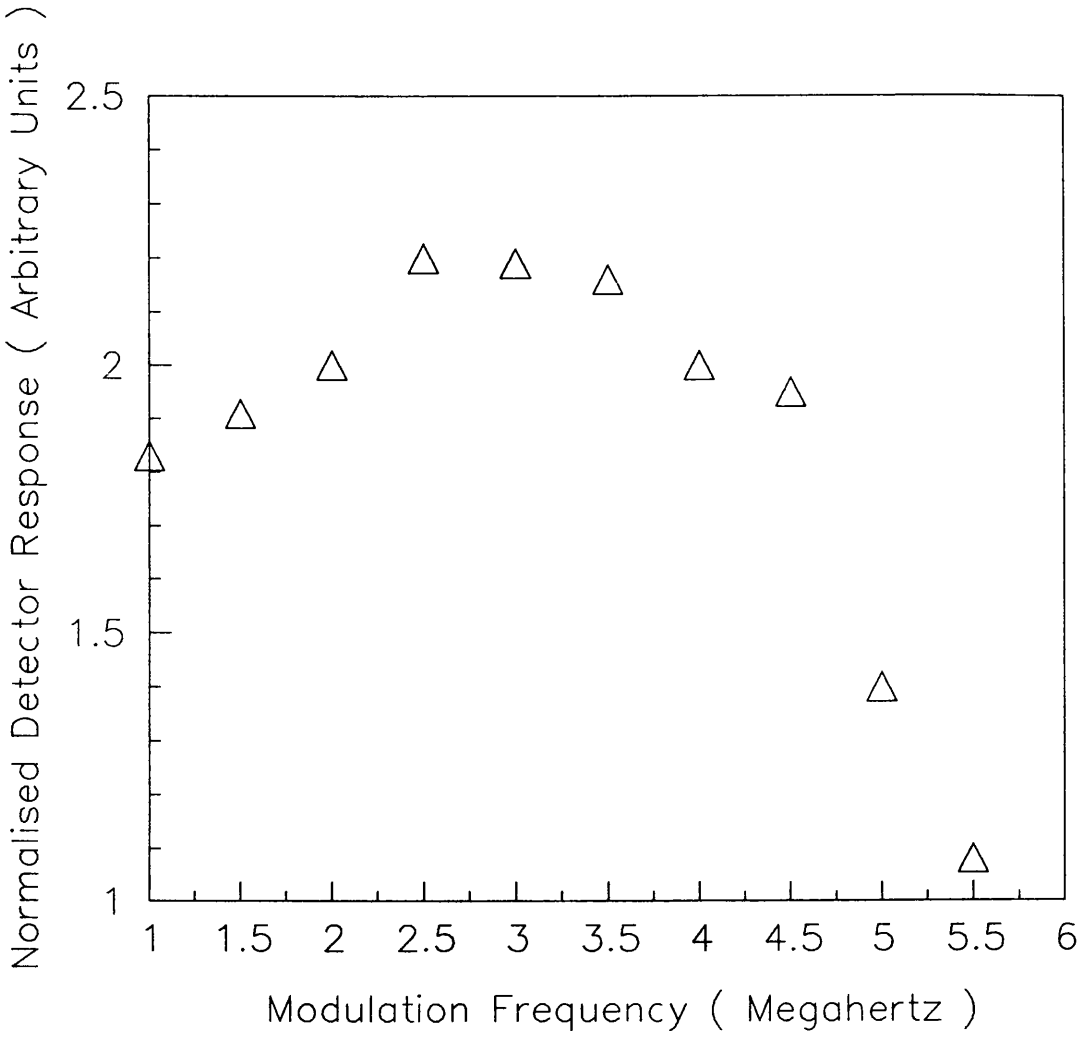

FIGURE 5.20 Variation of normalised detector response as a function of modulation frequency.

CHAPTER 6 DISCUSSION AND FURTHER WORK

6.1 Detector parameters

In chapter one certain figures of merit were defined which enable the comparison of detector performances. The performance of the $Ga_{1-x}Al_xAs/GaAs$ heterojunction detector can thus be described in terms of these four principle figures of merit.

6.1.1 Responsivity

The voltage responsivity is the change in the rms signal voltage, dV, from the detector produced by a change, dP, in the power incident upon it:-

$$\Re = \frac{dV}{dP} \qquad 1.1$$

In the course of this research project four different detector systems were developed in an attempt to optimise the performance of the detector.

(i) The preliminary Oxford detector system.

The preliminary Oxford detector system was used to detect radiation from a 98 GHz Gunn oscillator. The variation of measured responsivity as a function of oscillator power is shown in figure 6.1.

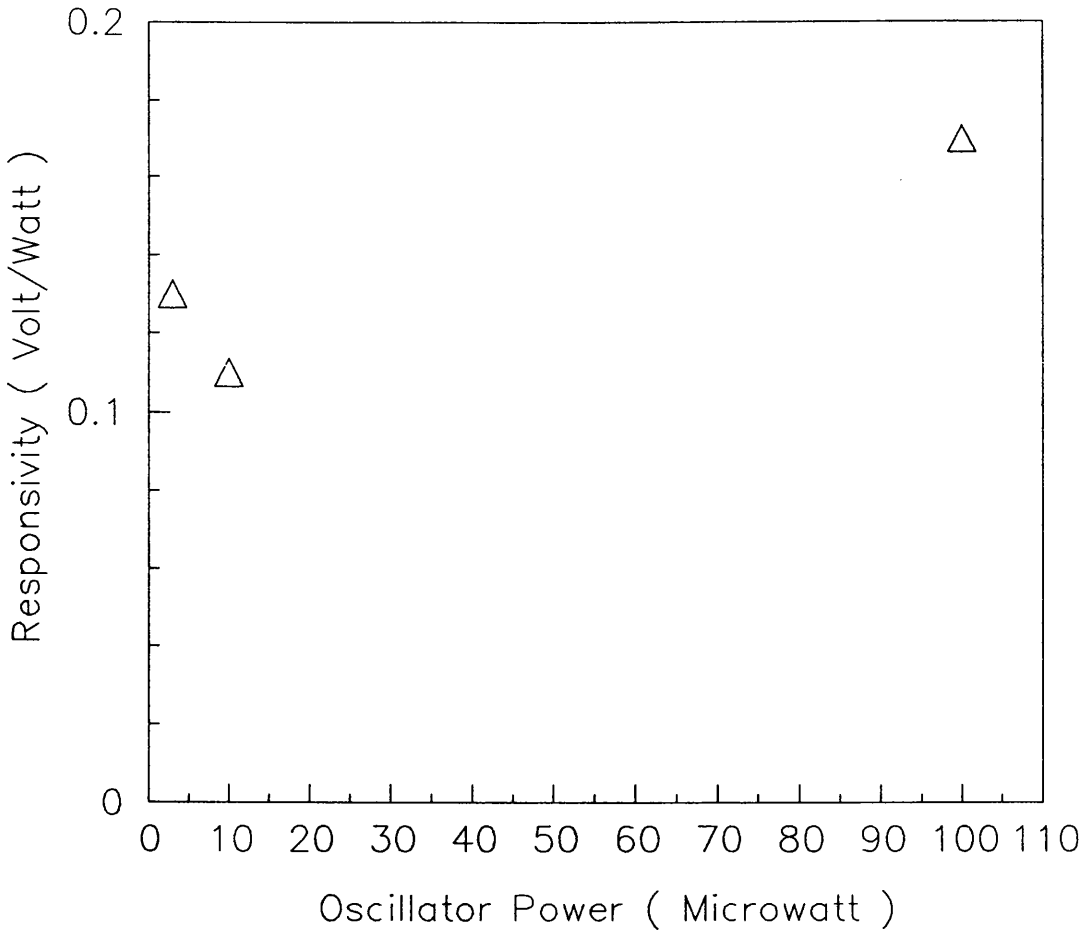

FIGURE 6.1 Variation of voltage responsivity as a function of oscillator power (Oxford System - preliminary set-up).

In the preliminary experiments the detector had no special detector mount. The radiation was simply directed at the detector along a light pipe. The maximum responsivities measured ranged from 0.11 to 0.17 V/W for oscillator powers of 3 to 100 μW. These results are for a bias current of 10 μA.

The preliminary Oxford detector system was also used to detect radiation from a 119 μm laser. No conclusions concerning the detector's responsivity could be drawn from the laser signal, as the incident power could not be assessed.

(ii) The modified Oxford detector system.

The modified Oxford detector system was used to detect radiation from a 98 GHz Gunn oscillator. Detector B was placed in a specially designed mount incorporating a backshort to maximise the electric field strength at the two dimensional electron gas. Figure 6.2 shows the variation of measured responsivity as a function of oscillator power. The maximum responsivities measured ranged from 0.04 to 0.54 V/W for oscillator powers of 2 to 100 μW. The responsivity was shown to have its highest value at low input power levels, achieving a responsivity of 0.54 V/W at a power level of 2 μW. The responsivity falls off at higher input power levels. These results are for a bias current of 10 μA.

No conclusions could be drawn from the 90 GHz Impatt oscillator concerning the detector's responsivity. Although the input power as a whole could have been measured, it was not possible to determine the distribution of the power between the harmonics observed.

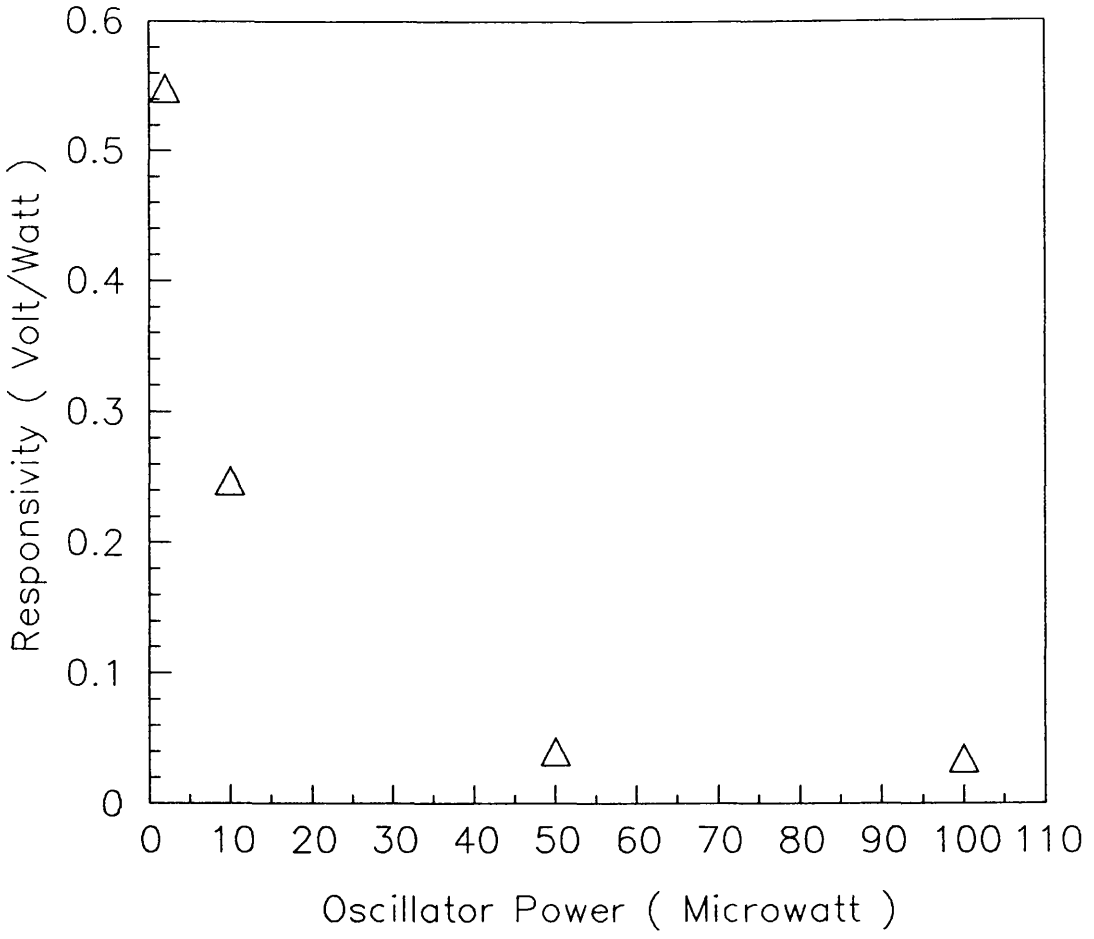

FIGURE 6.2 Variation of voltage responsivity as a function of oscillator power (Modified Oxford System).

(iii) Initial Bath detector system.

The initial detector system at Bath was used to detect radiation from a 98 GHz Gunn oscillator. The variation of the measured responsivity as a function of the oscillator power is shown in figure 6.3, both before and after illumination of the detector with visible light.

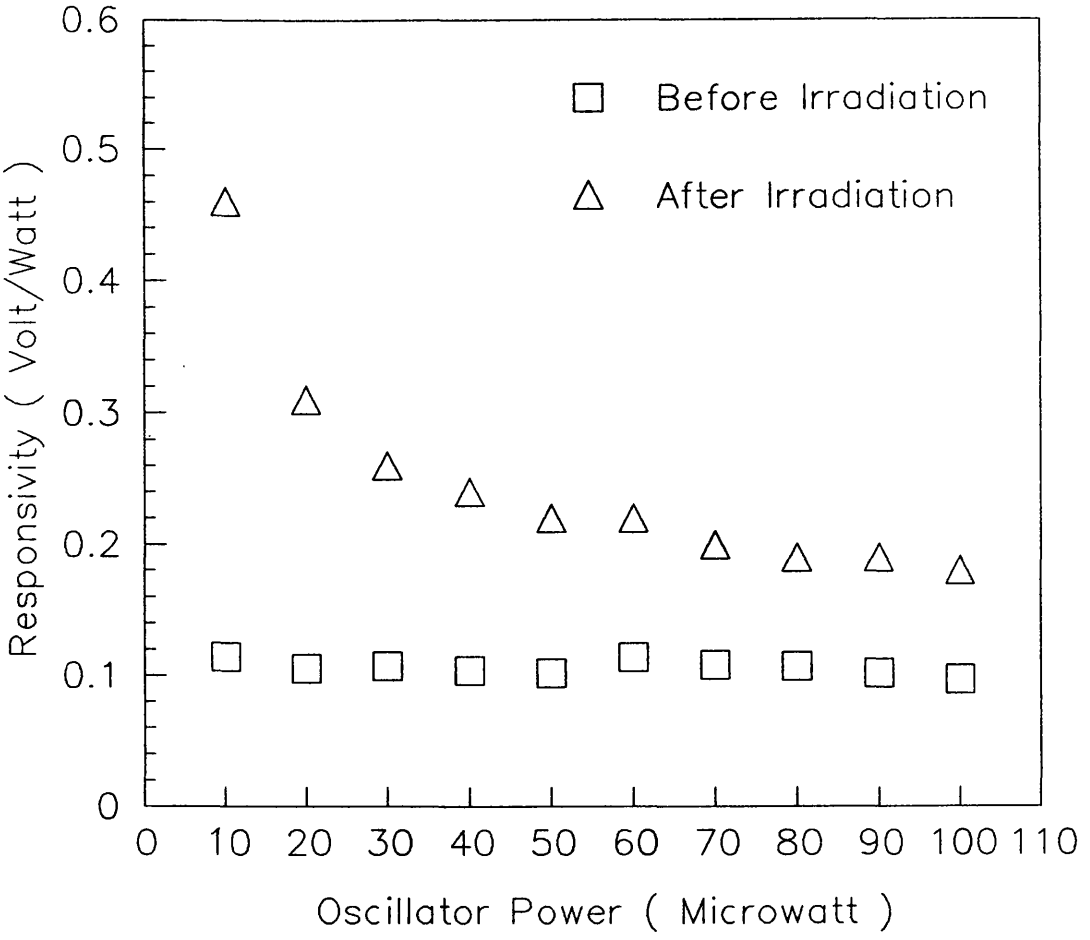

FIGURE 6.3 Variation of voltage responsivity as a function of oscillator power (Initial Bath System).

The maximum responsivities measured ranged from 0.2 to 0.46 V/W (after irradiation with visible light) for oscillator powers of 10 to 100 μW. These results are for a bias current of 10 μA.

It can be seen that the application of visible light more than doubled the responsivity of the detector. The upper curve, corresponding to the detector's responsivity after

illumination, follows a similar shape to that observed with the modified Oxford detector system. The lower curve appears a similar shape to that observed in the preliminary Oxford system, showing a more uniform responsivity over the range of power levels applied. The difference could be due to the change in position of the Fermi level relative to the Landau levels, before and after illumination. Illuminating the detector increases the carrier concentration within the quantum well, due to the persistent photoeffect. It is possible that the Fermi level has moved from a position lying within a Landau level to one lying between two Landau levels.

(iv) The Bath compact detector system.

The final detector system was used to detect radiation from a 98 GHz Gunn oscillator and a 113 GHz klystron oscillator. The variation of the measured responsivity as a function of the oscillator power, for the klystron oscillator is shown in figure 6.4.

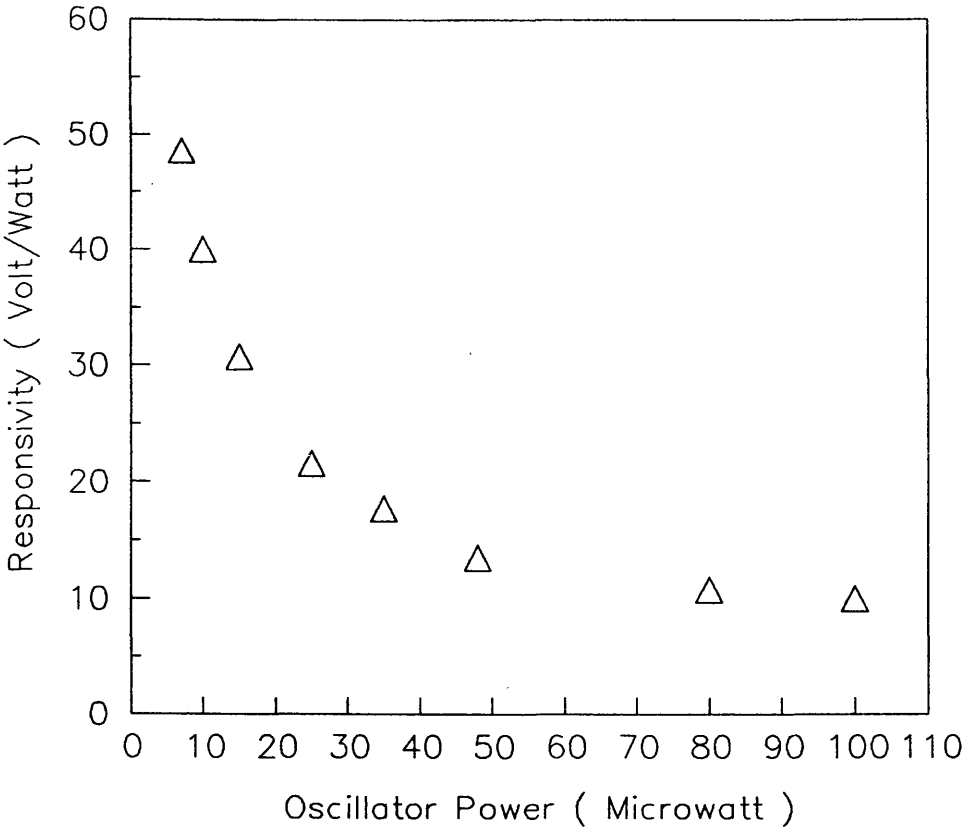

FIGURE 6.4 Variation of voltage responsivity as a function of oscillator power (Bath Compact System).

The responsivity curve can be seen to be the same as observed previously. The responsivity has a value of approximately 49 V/W, when detecting a 7 μW signal. The value of the responsivity falls to 15 V/W for a 100 μW signal. These results are for a zero bias current. Increasing the bias current from zero to 10 μA increased the detector response by approximately 30 %. Therefore at 10 μA a responsivity of 64 V/W would be expected.

Table 1 summarises the responsivities measured for the different detector systems, for a 10 μA bias current.

Detector System	Oscillator Power Range μW	Measured Responsivity V/W
Preliminary Oxford System	3 - 100	0.11 - 0.17
Modified Oxford System	2 - 100	0.04 - 0.54
Initial Bath System	10 - 100	0.2 - 0.46
Bath Compact System	7 - 100	20 - 64

Table 1 Responsivities measured for the four detector systems.

It can be seen that a significant improvement in the measured detector responsivity has been achieved in the final system. A responsivity of 64 V/W was measured on the final system, showing an increase of over two orders of magnitude in the measured responsivity from the preliminary system. The improvement was achieved in a compact system, using permanent magnets in place of the bulky electromagnets in the earlier detector systems.

The exact mechanism responsible for the photoconductive cyclotron resonance signal observed for a two dimensional

electron gas is currently of great interest. The relative importance of the thermal and electronic effects taking place is not yet fully understood. However a rough calculation of the theoretical responsivity of the detector was carried out making the assumption that the observed photoconductive cyclotron resonance signal was due to the heating of electrons above the lattice temperature.

Sakaki et al. determined the change in electron temperature as a function of the power input per electron for $Ga_{1-x}Al_xAs/GaAs$ heterojunctions. The results showed that quite different samples lie on the same experimental curve, see figure 2.13. Therefore for this approximate calculation it is assumed that the detector material used in this project would also lie on or close to this curve.

The electron density of the detector's two dimensional electron gas was approximately 1.5×10^{11} cm^{-2}. The dimensions of the detector were 1.5 mm x 0.25 mm x 0.25 mm. Therefore the number of electrons available to absorb power from the incident electromagnetic radiation was 5.63×10^{8}. Considering a total input power of 10 μW completely absorbed by the electron gas, the input power per electron would be approximately 1.78×10^{-14} W. From Sakaki's experimental data, the resulting rise in electron temperature would be approximately 6.3 K.

The variation of the detector's resistance as a function of temperature was measured as shown in figure 4.9. Assuming that the electron temperature will affect the detector's resistance in the same way as the lattice temperature, this graph enables a change in the detector's resistance to be deduced for a given electron temperature. The gradient of the curve at low temperatures is approximately. 2.1 Ω/K. The change in electron temperature of 6.3 K, produced by an input power of 10 μW, would therefore cause the resistance of the detector to change by approximately 13.2 Ω.

As the actual responsivities measured on this system were for a 10 μA bias current, this bias current will be considered for this calculation. A change in the detectors resistance of 13.2 Ω will result in a change in the detector output voltage of 132 μV, and a subsequent responsivity of 13.2 V/W.

Figure 6.5 shows the calculated detector responsivity as a function of input power.

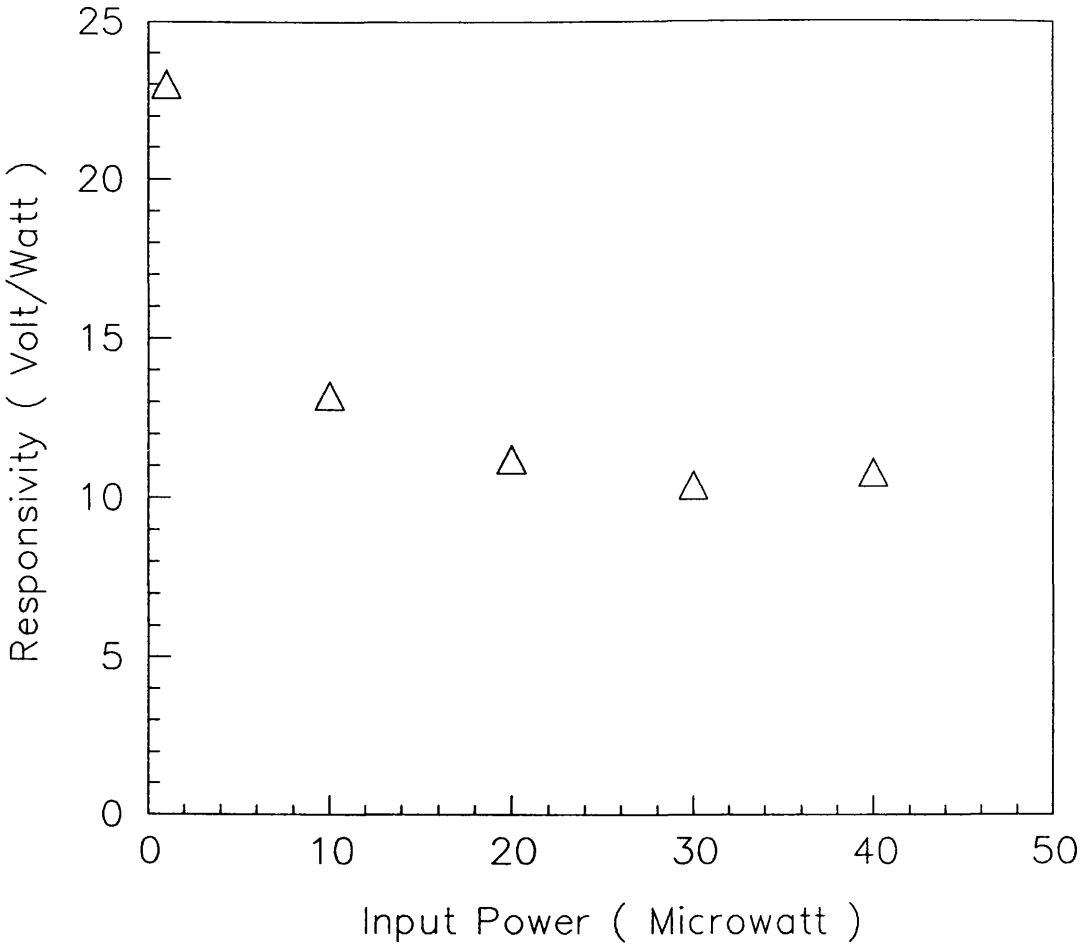

FIGURE 6.5 Calculated detector responsivity as a function of input power.

The above calculation assumed that the photoconductive cyclotron resonance peak was produced solely by the heating of electrons above the lattice temperature. The heating being caused by the absorption of power under cyclotron resonance conditions. The theoretical responsivity curve is similar to that obtained by the final detector system shown in figure 6.4, including the increase in responsivity at

power levels less than 30 μW. However it does not explain the different responsivity curves that have been observed with earlier detector systems. Also the actual responsivity measured with the final detector system, of 64 V/W for an input power of 7 μW, can be seen to be greater than that predicted by this calculation. Therefore, this suggests that the hot electron effect may not fully describe the detection mechanism. Further work is required to determine the exact mechanisms responsible for the detector's response.

The responsivity of 64 V/W measured on the final detector system was calculated using the actual oscillator power output, and the measured voltage output from the cryostat feedthrough. It is highly likely that losses would have occurred within the system, causing this figure to be an underestimate of the detector's intrinsic responsivity. An estimate of the detector's intrinsic responsivity was carried out on the preliminary detector system. A correction was included to take into account the fact that the actual area of the detector contributing to the change in resistance was only a fraction of the total area irradiated. The 11 dB power loss down the initial piece of light pipe was also allowed for. The responsivity was measured for a bias current of 10 μA. From figure 3.14 it can be seen that increasing the bias current from 10 to 100 μA increased the detector response by 156 %. After these factors had been taken into account a detector responsivity of approximately 5500 V/W

was estimated for an incident power of 3 nW. This value is still likely to be an underestimate, as it did not take into account the extra loss in signal power from the end of the initial light pipe to the detector itself. The radiation beam was reflected through a 90 degree angle, and then passed through more light pipe and several windows before reaching the detector. The large increase in the detector's responsivity at very low power levels is in agreement with other cryogenic detectors. These show a drastic increase in responsivity when calibration measurements are made using a thermal source (approximately 10^{-17} W) instead of a coherent source (approximately 1 μW). The increase is also in agreement with the approximate theoretical calculation made above, which indicates a rapid increase in responsivity with decreasing signal level.

6.1.2 Noise equivalent power

The noise equivalent power of a detector is defined as the root mean square value of the sinusoidally modulated radiant power falling upon the detector which will give rise to a root mean square voltage equal to the root mean square noise voltage of the detector.

In the Oxford systems a rough estimate of the N.E.P. was made by measuring the amplitude of the noise fluctuations seen on the output trace, and comparing it to the cyclotron resonance signal amplitude. For detector A a N.E.P. of 4 x

10^{-12} W Hz $^{-1/2}$ was estimated. The estimate took into account the 11dB of power loss down the initial piece of light pipe. The estimate also took into account the fact that the actual area of the detector which was contributing to the change in resistance was only a fraction of the total area irradiated. Detector B was mounted in a specially designed mount incorporating a backshort to maximise the electric field strength at the two dimensional electron gas. Therefore an area correction is not valid for this system. For detector B a N.E.P. of 8 x 10^{-10} W Hz $^{-1/2}$ was estimated. This implies that the backshort in the detector mount may not have been located in the optimum position behind the detector. A more satisfactory detector mount would have a movable backshort, which could be adjusted to optimise the power absorbed by the two dimensional electron gas. This was in fact incorporated in the final detector system.

6.1.3 Spectral response

The spectral response of a detector is defined in chapter one as the band of the spectrum to which the detector responds and the manner in which some figure of merit varies within this band. Frequently the figure of merit is that of responsivity.

The $Ga_{1-x}Al_xAs/GaAs$ heterojunction detector has been shown to detect radiation at frequencies of 98 GHz from a Gunn oscillator, 90 GHz, 180 GHz (second harmonic), and 270

GHz (third harmonic) from an Impatt oscillator, 113 GHz from a klystron and 2.5 THz from a laser. This represents a very large band of the electromagnetic spectrum. The variation of the responsivity within this spectral range was unable to be determined, as explained previously.

6.1.4 Response time

An attempt was made with the final Bath experimental apparatus to estimate the response time of the detector. As described in chapter five, the response from both a $Ga_{1-x}Al_xAs/GaAs$ heterojunction detector and a Schottky diode detector were monitored for the same range of modulation frequencies. The $Ga_{1-x}Al_xAs/GaAs$ heterojunction detector output was then normalized to the Schottky diode detector. The variation of the normalised detector response as a function of the modulation frequency is shown in figure 5.20. The response was shown to remain fairly constant until a frequency of 4.7 MHz, at which it falls sharply. It should be noted that it is possible that the frequency limitation may still have been caused by the detector output arrangement itself, and that the true frequency limitation of the detector may in fact be far higher. The modulation frequency of 4.7 MHz corresponds in the upper limit to a time constant of 2×10^{-7} seconds.

6.2 Comparison with the indium antimonide hot electron bolometer

The principal detectors currently available for the sub-millimetre band are described in section 1.2. The most comparable detector to the $Ga_{1-x}Al_xAs/GaAs$ heterojunction detector is the indium antimonide hot electron bolometer. Both are bulk detectors, cooled to helium temperature. Comparing the responsivities of the two detectors, it can be seen that the responsivity of the indium antimonide detector of 8000 V/W [Q.M.C. Instruments 1991] is far greater than that measured for the $Ga_{1-x}Al_xAs/GaAs$ heterojunction detector of 64 V/W. It must, however, be taken into consideration that the responsivity quoted for the indium antimonide detector is measured under highly optimised conditions. The responsivity predicted by the initial Oxford system was 5500 V/W. This value did not take into account the extra loss in signal power from the end of the initial light pipe to the detector itself. The radiation beam was reflected through a 90 degree angle, and then passed through more light pipe and several windows before reaching the detector. Considering the non-optimized conditions in which the responsivity measurement was made, the $Ga_{1-x}Al_xAs/GaAs$ heterojunction detector's responsivity may be comparable with that of the indium antimonide detector.

The quoted noise equivalent power for the indium antimonide detector is 1 x 10^{-12} W/Hz$^{-1/2}$ [Q.M.C. Instruments 1991]. A very rough estimate of the noise equivalent power of the $Ga_{1-x}Al_xAs$/GaAs heterojunction detector gave a value of 4 x 10^{-12} W/Hz$^{-1/2}$. These values compare well.

The principal weakness of the indium antimonide detector lies with its slowness in response. Typical response times are in the region of 10^{-6} s. When used in a mixer system this corresponds to maximum intermediate frequency bandwidth of 1 MHz. Results from the $Ga_{1-x}Al_xAs$/GaAs heterojunction detector show that it has a response time of 2 x 10^{-7} s. The response time measured could have been due to the detector output arrangement. The actual response time could be much faster than this. Rikken et al measured an exponential time constant of 20 ns.

6.3 Further work

The main failing of the third detector system lies in its inability to achieve magnetic field strengths of greater than approximately 0.3 T. For the investigation of the detector response for frequencies above approximately 123 GHz higher magnetic fields will be required. The mechanism for the variation of the magnetic field strength was also far from optimum.

An improved detector system would incorporate a helium cooled superconducting magnet mounted within the detector cryostat. A magnet system which could sweep through magnetic field strengths up to a value of 2 T would ensure that the detector's response to frequencies up to approximately 820 GHz could be investigated. A cooled amplifying system within the detector cryostat would also reduce the noise in the system.

Most of the measurements carried out have been restricted to frequencies of 98 GHz and 113 GHZ because of the availability of oscillators and waveguide components. In the final system it was also restricted by the magnetic field strength achievable, as explained above. Nevertheless, since it is in the submillimetre range that this detector is likely to have most impact, future work should be carried out at higher frequencies. High frequency oscillators or frequency multipliers could be used to provide the desired frequency radiation.

Once an optimised detector system has been achieved, further investigation into the $Ga_{1-x}Al_xAs/GaAs$ heterojunction detector's performance should be carried out.

The responsivity and the noise equivalent power should be assessed. Under optimised conditions, a conventional technique involving the observations of a thermal black-body source of variable temperature could be used to assess these quantities.

One of the most important parameters to quantify is the time response of the detector. A possible method for achieving this involves measuring the beat between two Gunn oscillators. The apparatus involved is shown in figure 6.6.

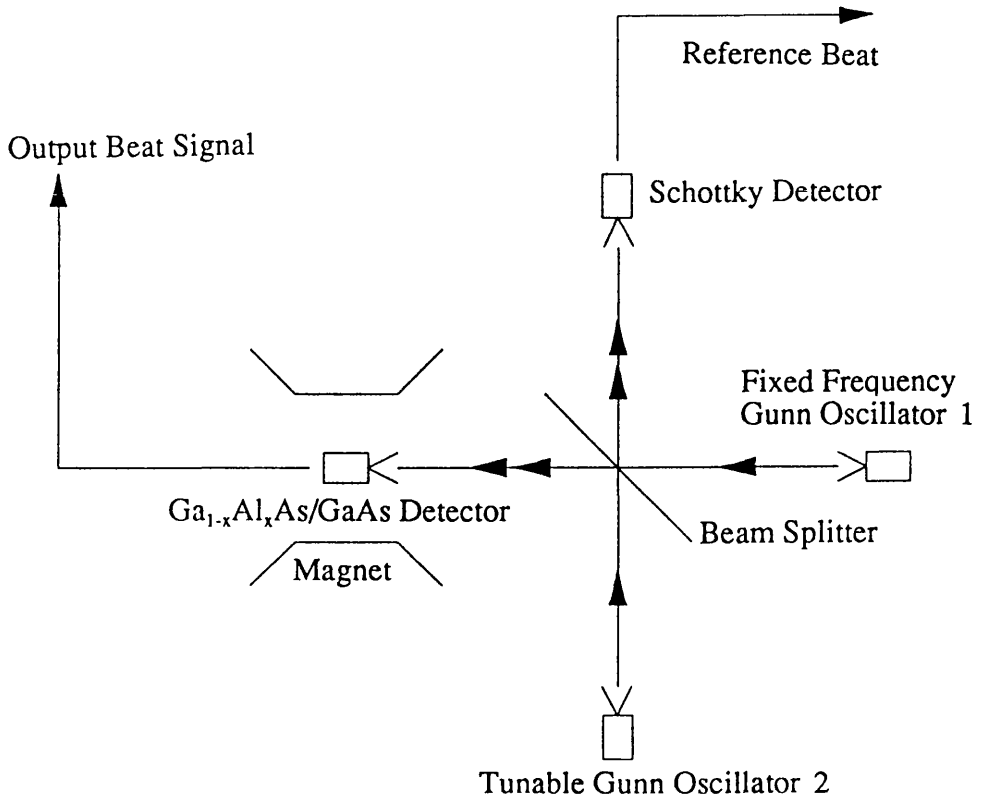

FIGURE 6.6 Apparatus for accurate measurement of detector response time.

Oscillator two would be tuned to gradually increase the beat frequency. The response time would then be given by the reciprocal of the frequency at which the beat disappears.

In this project the emphasis was on the development of a detector system as a whole. Although three different

$Ga_{1-x}Al_xAs$/GaAs heterojunction detectors were used, it was not feasible to differentiate between them. Therefore different $Ga_{1-x}Al_xAs$/GaAs heterojunctions should be assessed on the new system to characterise the effect that the two dimensional electron gas carrier concentration and electron mobility have upon the detectors response.

Investigation into the exact mechanism of detection is needed to determine what effect or combination of effects are responsible for the observed detector signal.

A direct comparison with an indium antimonide hot electron bolometer would also be of interest.

CHAPTER 7 CONCLUSIONS

The modulation doped $Ga_{1-x}Al_xAs/GaAs$ heterojunction detectors consisted of a GaAs layer in contact with a $Ga_{1-x}Al_xAs/GaAs$ layer. An approximately triangular one-dimensional potential well is produced at the interface. Carrier motion in the perpendicular direction is quantized, while motion parallel to the interface remains free. A two dimensional electron gas is thus formed. When a magnetic field is applied to the heterojunction at a low temperature, a change in the density of states occurs in the plane normal to the field direction. The states fall into allowed levels called Landau levels; the energy gap between these levels being given by $E = \hbar\omega_c$. If electromagnetic radiation is applied perpendicular to the magnetic field at the cyclotron resonance frequency, then the energy can be absorbed enabling electrons to jump from one Landau level to the next. This mechanism leads to a change in the resistance of the detector which enables the radiation to be detected.

A $Ga_{1-x}Al_xAs/GaAs$ heterojunction detector was used to detect radiation from a Gunn oscillator (98 GHz), an Impatt oscillator (90GHz, 180GHz, 270 GHz), a klystron (113 GHz) and an optically pumped infrared laser (2.5 THZ).

Preliminary experiments were carried out at Oxford University. These predicted a responsivity of above 5500 V/W and a N.E.P. of 4×10^{-12} W $Hz^{-1/2}$ for detection of a 98 GHz oscillator. Shubnikov de Haas oscillations were also observed for the detector. A detector mount was designed for use with this system. Further experiments were carried out which included the detection of harmonics at 90 GHz, 180 GHz and 270 GHz from an Impatt oscillator. These measurements illustrated the potential of the detector as a low resolution scanning spectrometer.

A detector system was developed at Bath. The system incorporated a specially designed detector mount with a backshort, and a quasi optical system to direct the radiation beam onto the detector. The system allowed the detector to be irradiated with visible light, while at helium temperature. The system was used to detect radiation from a 98 GHz Gunn oscillator. The detector's responsivity was observed to double with the application of visible light.

Having achieved a working system at Bath, a need for a more compact detector system was recognized. The whole detector system was fitted into a standard Infrared Laboratories HD3 cryostat, the type of which are frequently used with current detectors. The detector mount incorporated its own magnets and an adjustable backshort. A responsivity of 64 V/W was measured on this system, showing an increase of over two

orders of magnitude in the actual measured responsivity from the preliminary experiments. The responsivity obtained on this detector system was thought to be too great to have been achieved by the hot electron effect alone, although no conclusion could be drawn about the exact detection mechanism. However, this value is still below that predicted by the preliminary experiments which included corrections for the power loss between the oscillator and the detector. An estimate of the time constant of the detector, gave a value of 2×10^{-7} seconds. The time constant measured may have been that of the detector system and not of the detector itself due to the signal output arrangement.

Further optimization of the detector system is required before a full investigation into the $Ga_{1-x}Al_xAs/GaAs$ heterojunction detector's performance can be carried out. The responsivity, noise equivalent power and time response of the detector should be accurately assessed. Different $Ga_{1-x}Al_xAs/GaAs$ heterojunctions should be assessed to characterise the effect that the two dimensional electron gas carrier concentration and electron mobility have upon the detectors response. The exact mechanism of detection should also be investigated.

A direct comparison with an indium antimonide hot electron bolometer would also be of interest.

ACKNOWLEDGEMENTS

This work was performed at the School of Physics at the University of Bath, with support from the Science and Engineering Research Council.

The author would like to thank Nigel Cronin for his guidance and encouragement throughout this project. The author thanks Philips Research Laboratories, Redhill, for supplying the $Ga_{1-x}Al_xAs/GaAs$ heterojunction detectors and for their continued interest in this project. Thanks also go to Robin Nicholas and Mark Brummel of Oxford University, for their help and advice, particularly in the use of their apparatus during the initial stage of this project.

The author also thanks the other members of the School of Physics, especially David Bullett, Orhan Berktay, Andrew Baker and Deborah Harris for their encouragement and help.

Finally the author would like to express her gratitude to her husband, Keith, for supporting her in all things during this study.

REFERENCES

G. Abstreiter, J.P. Kotthaus, J.F. Koch and G. Dorda. 1976. " Cyclotron resonance of electrons in surface space-charge layers on silicon." Physical Review B 14(6), 2480-2493.

T. Ando and Y. Uemura. 1974. " Theory of quantum transport in a two-dimensional electron system under magnetic fields. I characteristics of level broadening and transport under strong fields." Journal of the Physical Society of Japan 36(4), 959-967.

T. Ando. 1975. " Theory of the cyclotron resonance lineshape in a two-dimensional system." Journal of the Physical Society of Japan 38(4), 989-997.

T.Ando, A.B. Fowler and F. Stern. 1982 " Electronic properties of two-dimensional systems." Review of Modern Physics 54(2), 437-672.

F.R. Arams. 1973. " Infra-red to millimetre wavelength detectors." Artech House inc.

G. Bastard. 1982. " Theoretical investigations of super-lattice band structure in the envelope- function approxi-mation." Physical Review, B25(12), 7584-7597.

H.J.A. Bluyssen, J.C. Maan, L.J. van Ruyven, F Williams and P. Wyder. 1978." Mechanism of cyclotron resonance induced conductivity in n-GaAs." Solid State Communications 25, 895-898.

E.R. Brown, M.J. Wengler and T.G. Philips. 1985a. " Absolute response and noise equivalent power of cyclotron resonance assisted InSb detectors at submillimeter wavelengths." Journal of Applied Physics, 58(5). 2051-2059.

E.R. Brown, J. Keene and T.G. Phillips. 1985b. " A heterodyne receiver for the submillimeter wavelength region based on cyclotron resonance in InSb at low temperatures." International Journal of Infrared and Millimeter Waves 6(11), 1121-1138.

M.A.C.S. Brown, and M.F. Kimmit. 1963. " Narrow bandwidth tuneable infra-red detectors." British Communications and Electronics, August, 608-612

E. Burstein, D.N Langenberg and B.N. Taylor. 1961." Superconductors as quantum detectors for sub-millimeter-wave radiation." Physical Review Letters 6(3), 92-94.

J.M. Cassels. 1982. " Basic quantum mechanics." The Macmillian Press Ltd. 109-113.

M.J. Chou, D.C. Tsui and A.Y. Cho. 1987. " FIR photoconductivity in the integral quantum hall regime in GaAs/AlGaAs." Proceedings of the 18th Conference on the Physics of Semiconductors, 437-440.

N.J. Cronin and V.J. Law. 1985. " Planar millimeter-wave diode mixer." IEEE Transactions on Microwave Theory and Techniques MTT-33(9), 827-830.

A.H. Dayem and R.J. Martin. 1962. " Quantum interaction of microwave radiation with tunneling between superconductors." Physical Review Letters, 246-248.

G.H. Döhler. 1983. " Solid-state superlattices." Scientific American 249(5), 118-126.

J.L. Dunham. 1932. " The Wentzel-Brillouin-Kramers method of solving the wave equation." Physical Review 41, 713-720.

F.F. Fang, T.P. Smith III and S.L. Wright. 1988. " Landau level broadening and scattering time in modulated doped GaAs/AlGaAs heterostructures." Surface Science 196, 310-315.

C. T. Foxon and J.J. Harris. 1986. " The growth of high purity III-V structures by molecular beam epitaxy." Philips Journal of Research 41(3), 313-324.

M.A. Frerking. 1987. " Summary of submillimeter (terahertz) receiver technology conference at Lake Arrowhead." Conference Digest, Twelfth International Conference on Infrared and Millimeter Waves. 111-112.

D.W. Goodwin and R.H. Jones. 1961. " Far infrared and microwave detector." Journal of Applied Physics 32(10), 2056-2057.

J.J. Harris, C.T. Foxon, D.E. Lacklison and K.W.J. Barnham. 1986. " Scattering mechanisms in (Al,Ga)As/GaAs 2DEG structures." Superlattices and Microstructures 2(6), 563-568.

M. Helm, E. Gornik, A. Black, G.R. Allan, C.R. Pidgeon, K. Mitchell and G. Weimann. 1985 " Hot electron landau level lifetime in GaAs/GaAlAs heterostructures." Physica 134B, 323-326.

K. Hess. 1979. " Impurity and phonon scattering in layered structures." Applied Physics Letters 35(7), 484-486.

R.E. Horstmann, E.J. Van der Broek, J. Walker, R.W. Van der Heijden, G.I.J.A. Rikken, H. Sigg, P.M. Frijlink, J. Maluenda and J. Hallais. 1984. " Cyclotron resonance from the far infrared transmission and the photoconductivity of the two-dimensional electron gas of a GaAs/AlGaAs heterojunction." Solid State Communications 50(8), 753-756.

B.D. Josephson. 1962. " Possible new effects in superconductive tunnelling." Physics Letters 1(7), 251-253.

M.F. Kimmitt. 1970. " Far-infra red techniques." Pion Limited.

M.A. Kinch. 1968. " Heterodyne detection at mm wavelengths using a Rollin InSb bolometer." Applied Physics Letters 12(3), 78-80.

M.A. Kinch and B.V. Rollin. 1963. " Detection of millimetre and sub-millimeter wave radiation by free carrier absorption in a semiconductor." British Journal of Applied Physics 14, 672-676.

C. Kittel. 1976. " Introduction to solid state physics." John Wiley and Sons, Inc.

J.F. Koch. 1975. " The dynamics of conduction electrons in surface space charge layers." Festkorperprobleme XV, 79-112.

Sh.M. Kogan. 1963. " On the theory of hot electrons in semiconductors." Soviet Physics - Solid State 4(9), 1813-1819.

B. Lax. 1961. " Cyclotron resonance." Science 134. 1333-1340.

Landau and Lifshitz. 1977. " Quantum Mechanics." Pergamon Press Ltd.

U.S. Lidholm. 1978. " Low pass stripline filters for mm-wave fixer applications." Research Report 131, Research Laboratory of Electronics and Onsala Space Observatory, Chalmers University of Technology, Gothenberg, Swenden.

J.C. Maan, Th. Englert, D.C. Tsui and A.C. Gossard. 1982 " Observation of cyclotron resonance in th photoconductivity of two dimensional electrons." Applied Physics Letters 40(7), 609-610.

R.J. Nelson. 1977. " Long-lifetime photoconductivity effect in n-type GaAlAs." Applied Physics Letters 31(5). 351-353.

R.J. Nicholas. 1987. " High field magnetotransport: lectures I and II: analysis of Shubnikov de Haas oscillations and parallel field magnetotransport." Physics and applications of quantum wells and superlattices. Plenun Press. 217-228.

R.J. Nicholas, M.A. Brummel and J.C. Portal. 1984. " High magnetic field characterisation of MOCVD heterostructures and superlattices." Journal of Crystal Growth 68, 356-369.

Y.Okuyama and N.Tokuda. 1990. " Phonon-drag thermoelectric power in $Al_xGa_{1-x}As/GaAs$ heterojunctions at low temperatures." Physical Review B 42(11), 7078-7083.

Q.M.C. Instruments. 1991. Private communication.

E.H. Putley. 1960. " Impurity photoconductivity in n-type InSb." Proceedings of the Physical Society 76, 802-805.

E.H. Putley. 1961. " Impurity photoconductivy in n-type InSb." Journal of the Physics and Chemistry of Solids 22, 241- 247.

S. Ramo, J.R. Whinnery and T. Van Duzer. 1965. " Fields and waves in communication electronics." John Wiley and Sons, Inc.

G.L.J.A. Rikken, P. Wyder, K. Ploog, J.M. Chamberlain, R.T. Grimes and G.Hill. 1988. " Nanosecond far infra red magnetospectroscopy of GaAs/AlGaAs heterostructures." Surface Science 196, 303-309.

B.V. Rollin. 1961. " Detection of millimetre and sub-millimetre wave radiation by free carrier absorption in a semiconductor." Proceedings of the Physical Society 77, 1102-1103.

K.F. Sander and G.A.L. Reed. 1978. " Transmission and propagation of electromagnetic waves." Cambridge University Press.

H. Sakaki, K. Hirakawa, J. Yoshino, S.P. Svensson, Y. Sekiguchi, T. Hotta and S. Nishii. 1984. " Effects of electron heating on the two-dimensional magnetotransport in AlGaAs/GaAs heterostructures." Surface Science 142. 306-313.

S. Das Sarma and F. Stern. 1985. " Single-particle relaxation time verses scattering time in an impure electron gas." Physical Review B 32(12), 8442-8444.

D. Stein, G. Ebert, K. von Klitzing and G. Weimann. 1984. " Photoconductivity on GaAs-$Al_xGa_{1-x}As$ heterostructures." Surface Science 142, 406-411.

F. Stern and S. Das Sarma. 1984. " Electron energy levels in GaAs-$Ga_{1-x}Al_xAs$ heterojunctions." Physical Review B 30(2), 840-847.

H.L. Stormer, R. Dinger, A.C.Gossard, W. Wiegmann and M.D. Sturge. 1979. " Two dimensional electron gas at a semiconductor-semiconductor interface." Solid State Communications 29, 705-709.

H. L. Stormer, A. Pinczuk, A.C. Gossard and W. Wiegmann. 1981. " Influence of an undoped (AlGa)As spacer on the mobility enhancement in GaAs-(AlGa)As superlattices." Applied Physics Letters 38(9), 691-693.

B. Vinter. 1984. " Subband and charge control in a two-dimensional electron gas field-effect transistor." Applied Physics Letters 44(3), 307-309.

J.M. Ziman. 1964. " Principles of the theory of solids." Cambridge University Press.

APPENDIX A WAVEGUIDE TECHNIQUES

(a) Waveguide Transmission.

Consider a waveguide system consisting of two parallel plates as shown in figure A.1. The figure shows only a section of the system since both the plates are considered to be extended to infinity in both directions. The plates are the only boundaries to electromagnetic wave propagating between them. Each metal plate is considered to be a perfect conductor. No electric field can exist parallel to the wall at the surface of the wall. Hence the electric field of the electromagnetic wave must be perpendicular to the plane of the walls as shown in figure A.1.

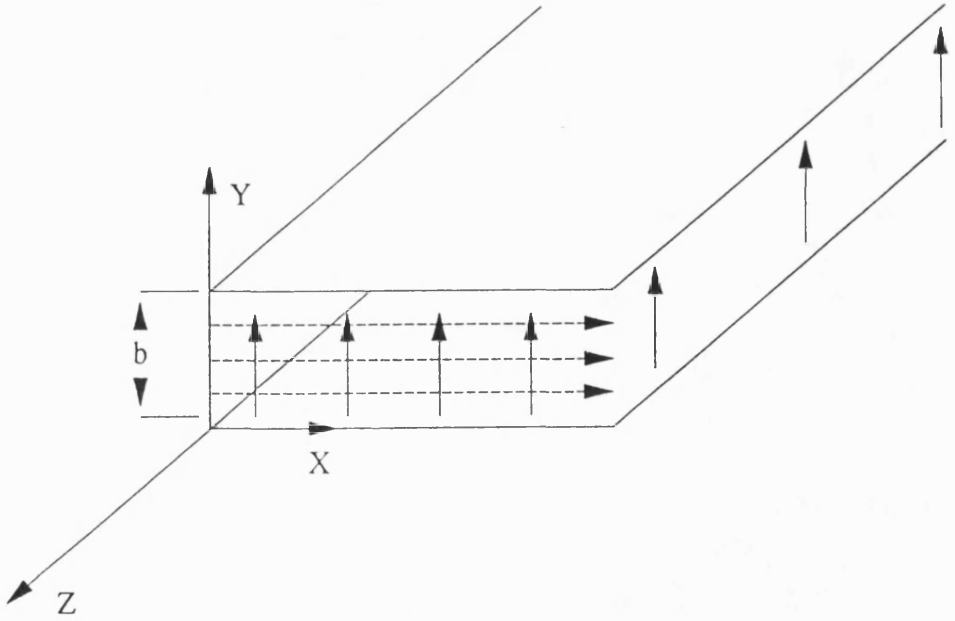

FIGURE A.1 A portion of an infinite parallel plate waveguide.
electric field. ------ magnetic field.

A perfectly conducting sheet is also a perfectly reflecting mirror, so that the electromagnetic field patterns shown in figure A.1 would be reflected to make the field patterns of an infinite plane wave in an infinite medium propagating in the z-direction. Hence the parallel plate waveguide can be considered to have taken a slice out of the plane wave which is propagating in the direction of the plates and whose electric field is perpendicular to the plane of the plates.

Figure A.2 shows a plane wave impinging at an angle onto a plane conducting sheet which is acting as a perfect reflector.

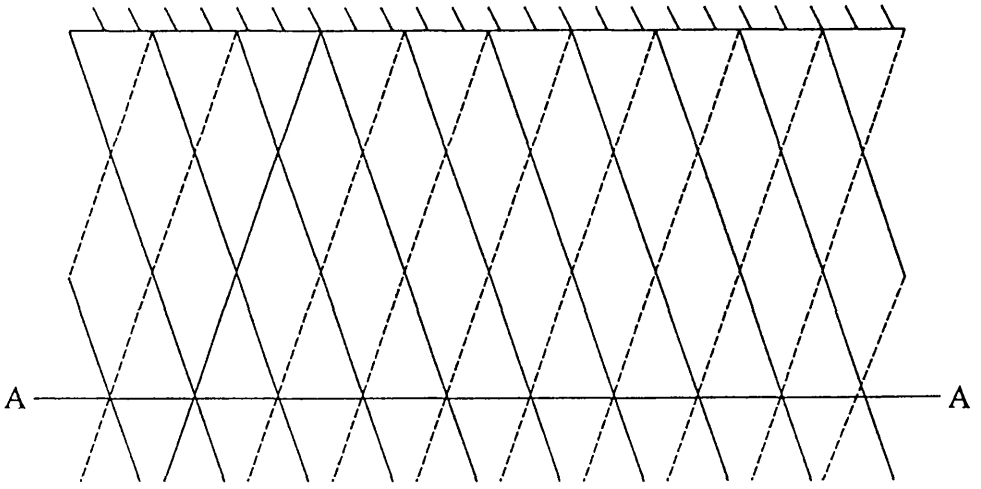

FIGURE A.2 Plane wave reflections from a plane conducting sheet, showing lines of equal phase for both incident and reflected wave.

The lines on the diagrams denote positions of equal phase, both on the incident and on the reflected wave. The direction of propagation of the wave will be perpendicular to the lines of equal phase which are a wavelength apart. It can be seen that a second conducting sheet could be positioned at A-A parallel to the first sheet, without affecting the wave pattern between the sheets. Such a plane wave propagating by reflection from two parallel reflectors is shown in figure A.3 together with a single ray along the direction of propagation of the plane wave.

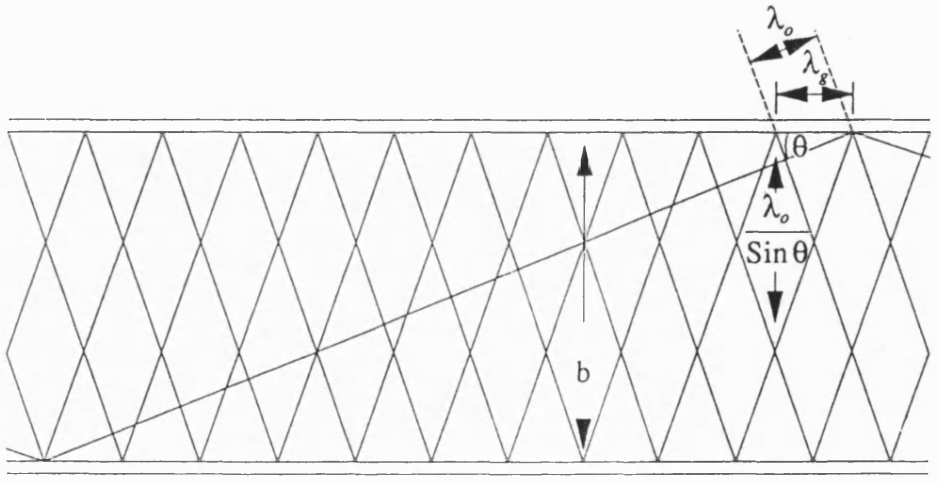

FIGURE A.3 Ray and phase front representation of an electromagnetic wave propagating between parallel plate waveguide.

It is seen that the ray is reflected without loss at an angle θ from the faces of the reflectors. The given boundary

conditions that the value of electric field must be zero at the plates, results in the condition that there should be a whole number of half wavelengths in the spacing between the plates. If that wavelength is λ_0 the projection of the wavelength is $\lambda_0/\sin\theta$. Then b, the spacing between plates, must satisfy the condition given by

$$b = \frac{n\lambda_0}{2\sin\theta} \qquad A.1$$

or

$$\sin\theta = \frac{n\lambda_0}{2b} \qquad A.2$$

where n is an integer. Therefore, θ will be zero if the spacing between the plates is just half a wavelength. Then the wave will bounce back and forth between the plates and there will be no propagation in the z-direction. This condition is called cutoff. The wavelength at which this occurs is called the cutoff wavelength, λ_c, and is given by

$$\lambda_c = \frac{2b}{n} \qquad A.3$$

As the frequency is raised, λ_0 /2b will be less than unity and θ will take on a finite value representing some component of the propagation in the z-direction.

In figure A.3 the direction of the propagation is in the plane of the paper and parallel to the plane of the plates. It can be seen that the wavelength in the direction of propagation is not the same as the wavelength of the plane wave. The wavelength in the direction of propagation along the waveguide is called the waveguide wavelength, denoted by λ_g. It is the projection of the plane wave wavelength in the direction of propagation between the plates, hence

$$\lambda_g = \frac{\lambda_0}{\cos\theta} \qquad A.4$$

Combining equations A.2 and A.4 to eliminate θ gives

$$\lambda_g = \frac{\lambda_0}{\sqrt{\left[1-\left(\frac{n\lambda_0}{2b}\right)^2\right]}} \qquad A.5$$

and substituting for λ_c gives

$$\lambda_g = \frac{\lambda_0}{\sqrt{\left[1-\left(\frac{\lambda_0}{\lambda_c}\right)^2\right]}} \qquad A.6$$

Therefore for a parallel plate guide, the guide wavelength is given by equation A.6.

The form of a rectangular waveguide is shown in figure A.4.

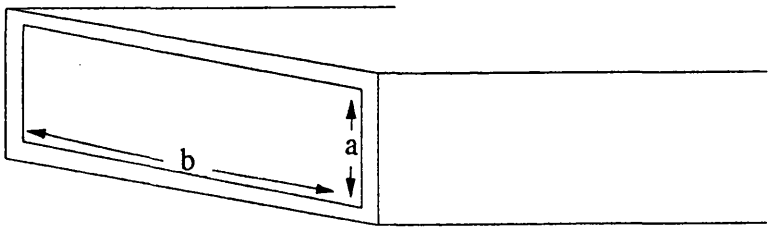

FIGURE A.4 Rectangular Waveguide.

The broad dimension is usually called a and the narrow dimension b. These dimensions apply to the inside of the waveguide, as anything external to these surfaces does not affect the wave inside the waveguide. The cut-off frequency for the rectangular wave guide occurs at

$$\lambda_c = 2a \qquad A.7$$

This cut-off frequency is therefore that for which the wide dimension is one half-wavelength. Substituting this value into equation A.6 the rectangular guide wavelength is given by

$$\lambda_g = \frac{\lambda_0}{\sqrt{\left[1 - \left(\frac{n\lambda_0}{2a}\right)^2\right]}} \qquad A.8$$

The cutoff frequency for a circular waveguide is given by

$$\frac{2\pi a}{x} \qquad A.9$$

where x is a solution of a Bessel function appropriate to a mode in a circular waveguide. The guide wavelength for a circular guide is therefore given by

$$\lambda_g = \frac{\lambda_0}{\sqrt{\left[1-\left(\frac{\lambda_0 x}{2\pi a}\right)^2\right]}} \qquad A.10$$

(b) Short-circuited guide

A waveguide can be considered as shorted if a conducting plate is placed across the entire section of the guide so that the transverse component of the electric field is reduced to zero over all of that section. The form of the resulting standing wave pattern is shown in figure A.5.

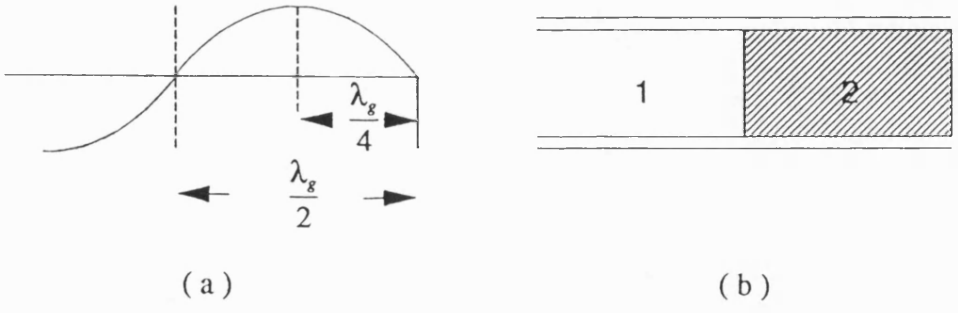

FIGURE A.5 (a) Standing waves of transverse electric field in shorted guide. (b) Guide with dielectric discontinuity.

The transverse electric field is zero at the conducting plate and at multiples of $\lambda_g/2$ in front of it. The transverse electric field and hence the power transfer along the waveguide is a maximum at odd multiples of $\lambda_g/4$ in front of the plate.

When a detector is mounted in a waveguide system, it is desirable to place it in a position at which it will absorb optimum power. A tuneable backshort is used to achieve this aim. A tuneable backshort is a conducting plate used to terminate the guide behind the detector. The position of the backshort is varied until a maximum in power absorption occurs at the detector. From the above, this will be approximately $\lambda_g/4$ behind the detector. If a tuneable backshort is not viable then the guide is simply terminated with a conducting plate $\lambda_g/4$ behind the detector.

(c) Stripline Filters

Stripline is a high frequency transmission line consisting of a thin planar conductor supported on a dielectric sheet with an earthed metallic plate on the opposite side of the dielectric. The impedance of the stripline varies with the width of the central conductor. A section where the central conductor has a greater width will present a lower impedance than a narrow section. Basically, the low impedance sections constitute shunt capacitances to ground and the high impedance sections constitute series inductances. Therefore

by creating a sequence of high impedance followed by low impedance sections along a stripline, a filter of inductors and capacitances can be formed.

A short can be achieved at the end of a filter by terminating the stripline at a distance of:

$$l + \frac{n\lambda}{2\sqrt{\epsilon_{eff}}} \qquad A.11$$

where ϵ_{eff} is the effective dielectric constant of the stripline. A typical suspended quartz-substrate (ϵ_r) configuration will give ϵ_{eff} = 1.5 [Lidholm 1978]. l is the measured zero impedance distance from the end of the filter as shown in figure A.6. The measurements were taken for an experimental filter whose dimensions are shown. The zero impedance distance for other filters must therefore be scaled accordingly.

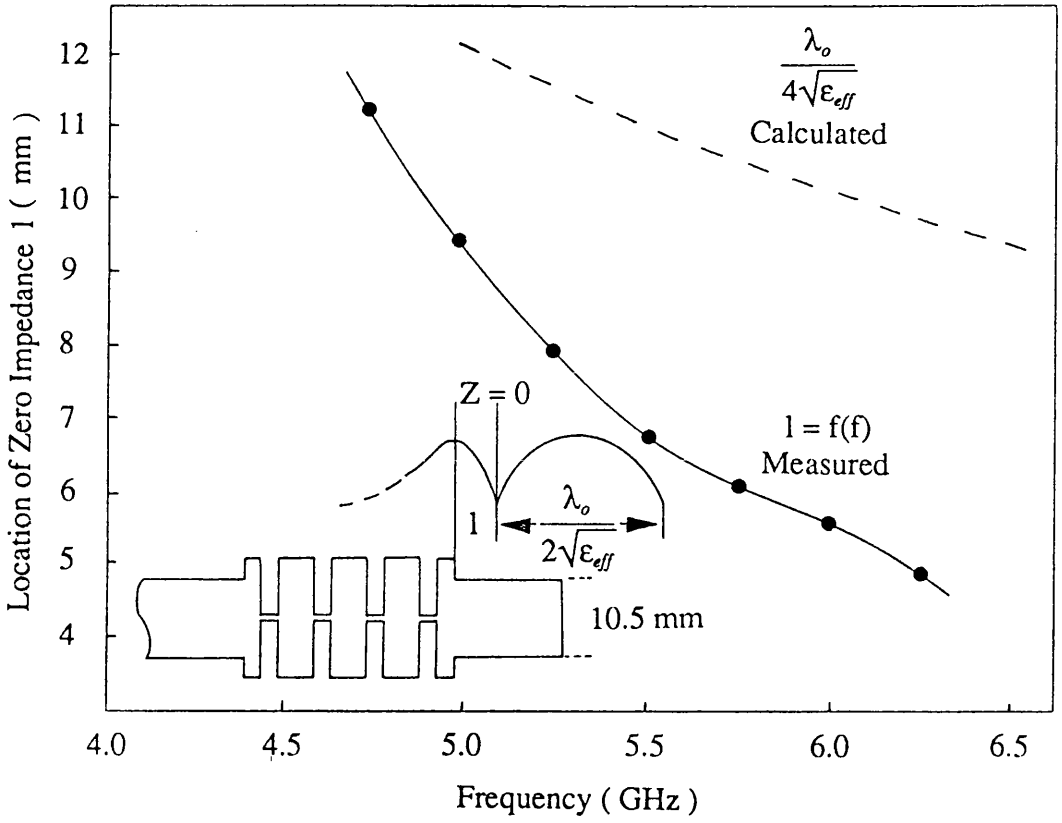

FIGURE A.6 The locations of zero impedance in front of the filter as a function of frequency.

APPENDIX B WORKSHOP DRAWINGS

B2 - Detector mount

B3 - Cross section of detector mount

B4 - Stripline channel in detector mount

B5 - Magnet holder

B6 - Flange face for back of detector mount

B7 - Backshort

B8 - Flange face for front of detector mount

1 DETECTOR MOUNT
ALL MEASUREMENTS ARE IN MMS
MATERIAL - BRASS
SCALE ~ 3:1

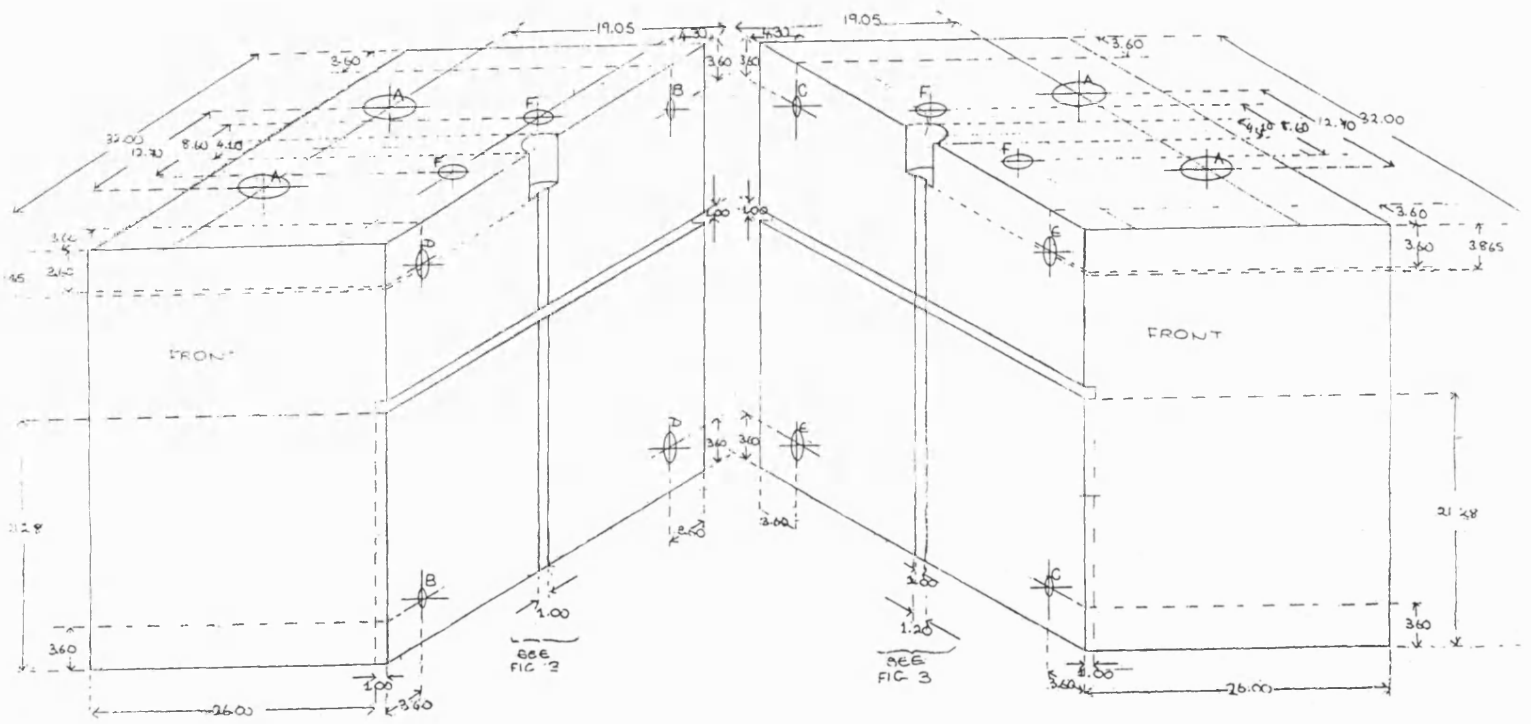

B2

2 CROSS SECTION OF DETECTOR MOUNT

ALL MEASUREMENTS ARE IN MMS

MATERIAL BRASS

SCALE ~ 3 : 1

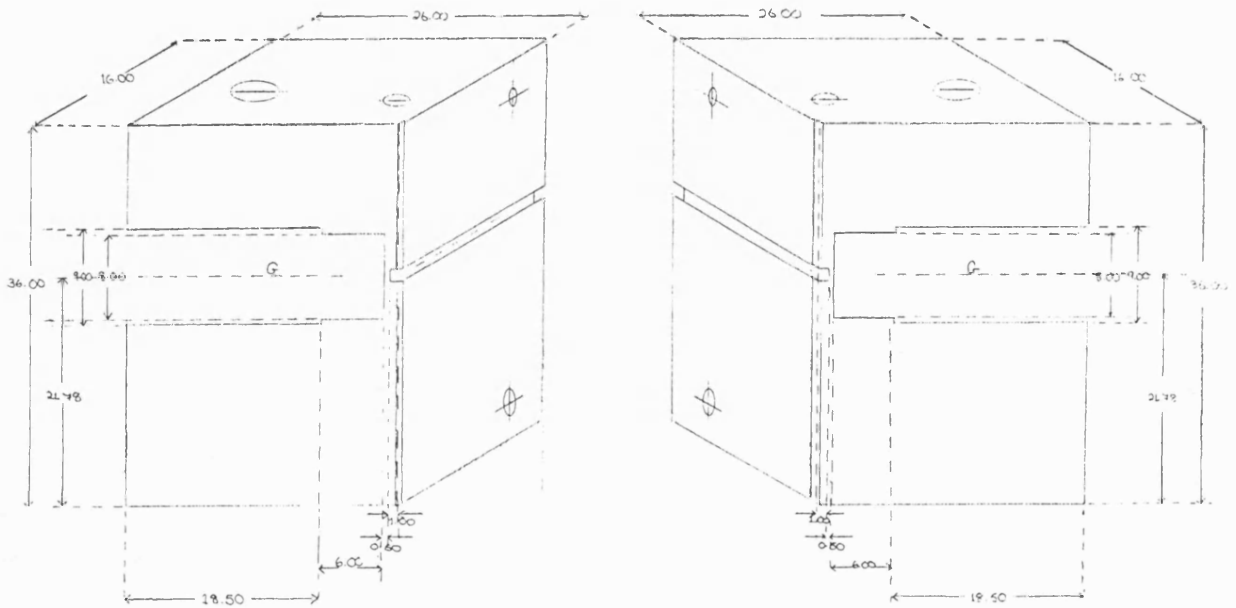

3

STRIPLINE CHANNEL IN DETECTOR MOUNT

ALL MEASUREMENTS ARE IN MMS

MATERIAL - BRASS

SCALE - 10 : 1

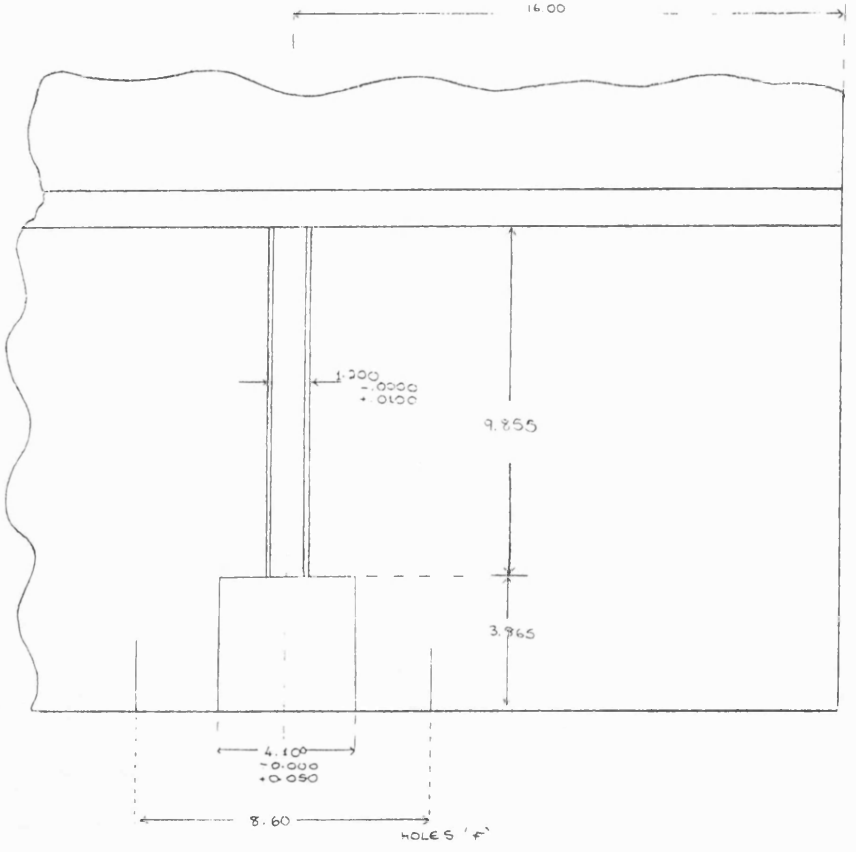

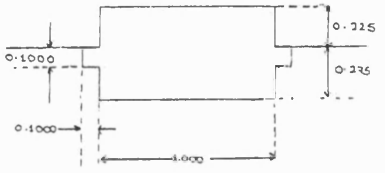

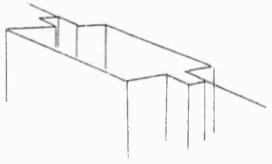

4

MAGNET HOLDER

ALL MEASURMENTS ARE IN MMS
MATERIAL BRASS
SCALE ~10 1

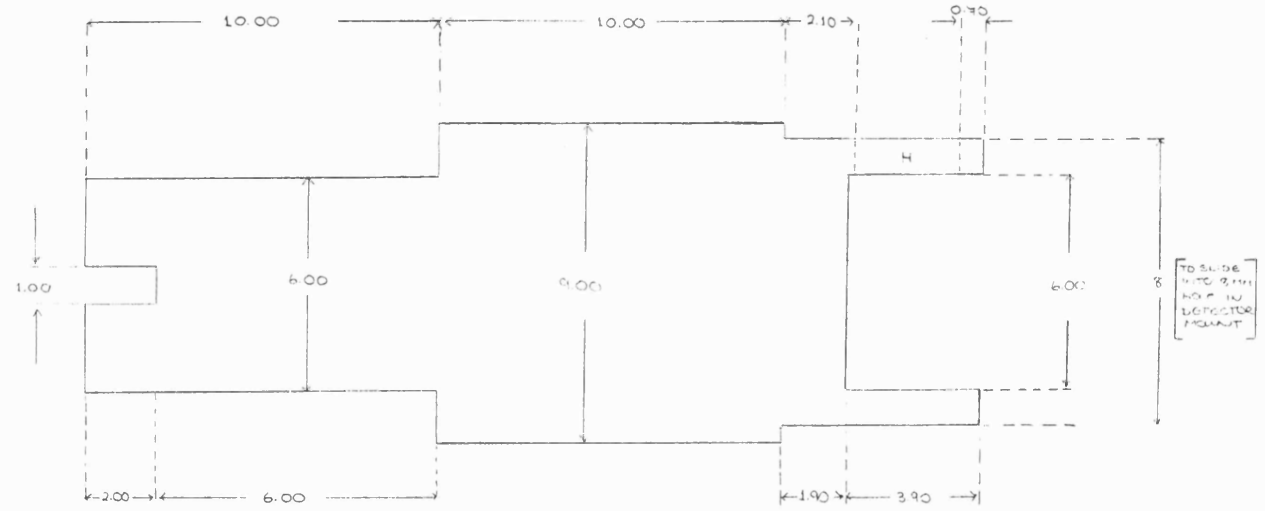

5

FLANGE FACE FOR BACK OF DETECTOR MOUNT

ALL MEASUREMENTS ARE IN MMS

MATERIAL - BRASS

SCALE ~ 10 : 1

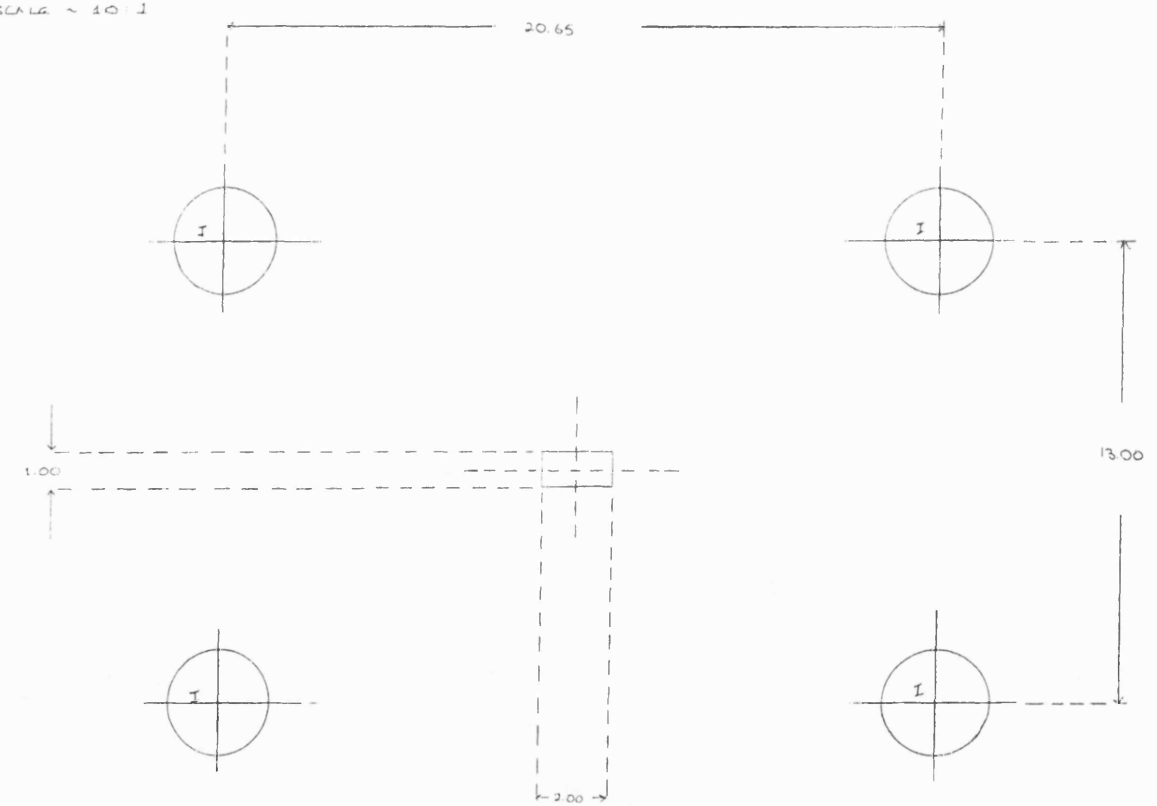

6

BACKSHORT

ALL MEASUREMENTS ARE IN MMS

MATERIAL - BRASS

SCALE ~10 : 1

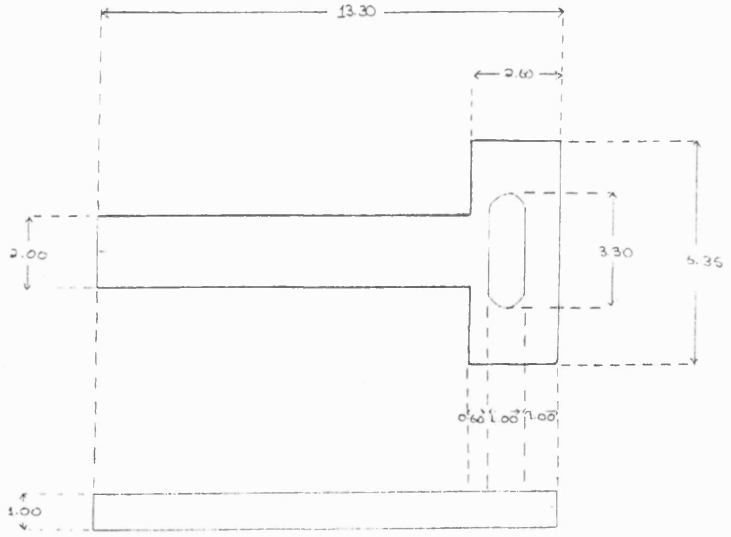

B7

7

FLANGE FACE FOR FRONT OF DETECTOR MOUNT
ALL MEASUREMENTS ARE IN MMS
MATERIAL - BRASS

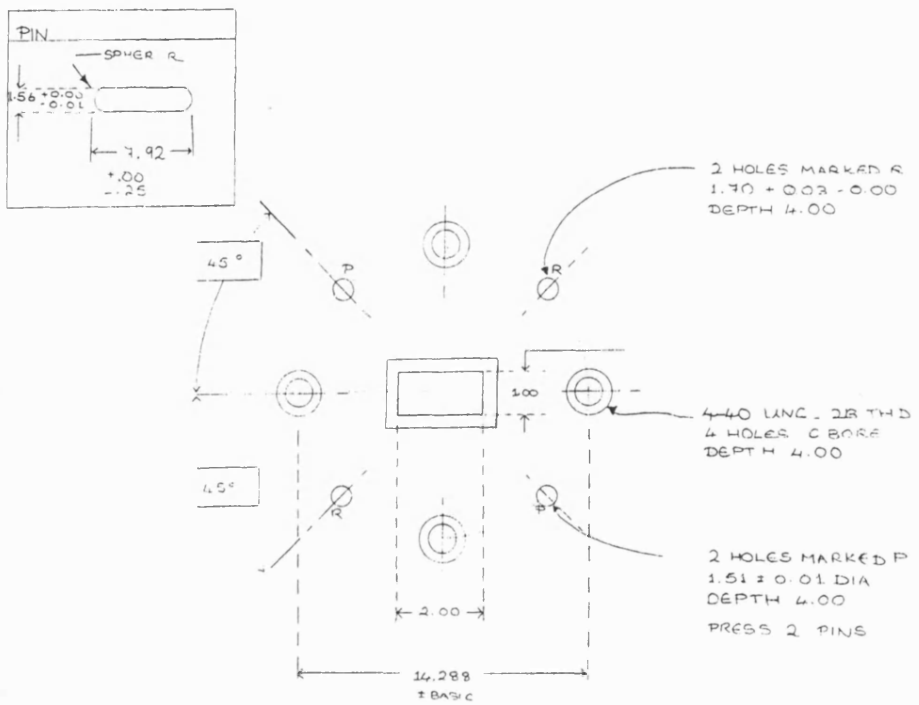

APPENDIX C

PUBLISHED PAPERS

International Journal of Infrared and Millimeter Waves, Vol. 8, No. 8, 1987

MILLIMETER AND SUBMILLIMETER DETECTION USING $Ga_{1-x}Al_xAs$/GaAs HETEROSTRUCTURES

S. M. Smith and N. J. Cronin

School of Physics,
University of Bath,
Claverton Down, Bath BA2 7AY, U.K.

R. J. Nicholas and M. A. Brummell

Clarendon Laboratory,
Parks Road, Oxford OX1 3PU, U.K.

J. J. Harris and C. T. Foxon

Philips Research Laboratories,
Redhill, Surrey RH1 5HA, U.K.

Received March 15, 1987

We have shown that a $Ga_{1-x}Al_xAs$/GaAs heterostructure can be used as a sensitive tunable detector of mm-wave/sub-mm-wave radiation. The mechanism for detection requires the application of a magnetic field varying from approximately 0.2T at 94GHz (3.2mm wavelength) to 6.2T at 2500GHz (119μm wavelength). The responsivity and N.E.P. at 3.2mm have been roughly estimated at 200V/W and $5\times10^{-11}W/\sqrt{Hz}$ respectively. The speed of such a detector could be several orders of magnitude greater than comparable InSb detectors.

Key words : submillimetre, $Ga_{1-x}Al_xAs$/GaAs, detector

0195-9271/87/0800-0793$05.00/0

Introduction

The submillimetre region of the spectrum extends from 300 to 1000GHz; exploitation of the full potential of this region has been restricted, however, by the limited range of devices which are capable of functioning at such high frequencies. One of the most significant shortcomings has been the absence of a fast submillimetre detector. Comparing the sub-mm and short-mm regions with the infrared it is apparent that detectors in the infrared are far superior in terms of both speed and noise equivalent power (N.E.P.). The reason for this difference is that no extrinsic photoconductive detectors are available working at wavelengths greater than about 100μm. At longer wavelengths most detectors are based upon hot electron effects which are intrinsically slower and less responsive.

In view of the important applications for fast detectors, considerable efforts are being made to fill the gap by developing new devices. We here report on a new type of detector based on a $Ga_{1-x}Al_xAs/GaAs$ heterojunction which responds to radiation ranging from 3.2mm to 119μm and which for theoretical reasons promises to be up to four orders of magnitude faster than currently available detectors.

Two dimensional electron gas heterostructures (2 DEGS)

The physical system which we have been studying is the modulation doped $Ga_{1-x}Al_xAs/GaAs$ heterojunction, with x typically 0.33, in which a quasi-two-dimensional electron gas (2 DEG) is formed as an inversion layer in the GaAs at the interface. The low temperature electron mobility in these structures can be greatly enhanced by modulation doping where only the $Ga_{1-x}Al_xAs$ is doped so that the electrons are spatially separated from the ionised donors which dominate the scattering. An undoped $Ga_{1-x}Al_xAs$ spacer layer at the interface increases this separation and further enhances the mobility [1]. The bar shaped sample studied was prepared by molecular beam epitaxy at the Philips Research Laboratories, Redhill. The growth techniques and 2 DEG properties have been reported previously [2]. Ohmic contacts to the sample were prepared by rapid alloying of a Au:Ge:Ni metalisation. At 4.2K, in the dark, the electron concentration in the two-dimensional

gas was $2x10^{11}cm^{-2}$, with a mobility of $6x10^{5}cm^{2}V^{-1}s^{-1}$; the carrier density could be increased to $4x10^{11}cm^{-2}$ by using the persistent photoconductivity effect. The electron states are quantised by an approximately triangular potential well at the interface, and the lowest confined state occurs at 25mev above the bottom of the well [3]. The Fermi level lies 7mev above this and the second confined level, which is 20mev above the lowest, is therefore unoccupied and remains so over the whole carrier density range.

The 2 DEG detector

As described above, the two dimensional electron gas exists in a set of sub-bands created by the confinement of the quantum well. The energy separation of these sub-bands is too great to be of direct interest in the wavelength range considered here, however, upon application of a magnetic field each sub-band further subdivides into Landau levels whose energy separation is determined by the magnitude of the applied field. Incident electromagnetic waves are absorbed by exciting transitions between Landau levels provided that the frequency equals the cyclotron resonance frequency. In a $Ga_{1-x}Al_xAs/GaAs$ heterostructure, $m^*/m \simeq 0.07$, and thus for 100GHz radiation (photon energy 0.06mev), the cyclotron frequency, $w_c = eB/m^*$ matches the incident frequency at a magnetic field B, of approximately 0.2T.

We have recently conducted a series of experiments in which we have used a heterojunction to detect signals from a 94GHz Gunn oscillator, a 119μm laser and a multifrequency Impatt oscillator. The sample was mounted across a rectangular waveguide in a specially designed detector mount, shown in figure 1. The backshort was arranged using shims to be a distance of approximately one quarter of a guide wavelength from the sample, at 94GHz. Figure 2 shows the experimental set-up used. Signals from the sources were modulated by a 1KHz chopper and then passed along a light pipe to the detector which was situated at the centre of a magnet. The 2 DEG heterostructure was constant current biased and the output voltage amplified and phase-sensitively detected. Input power level was adjusted by a variable attenuator and measurements were taken at 4.2K.

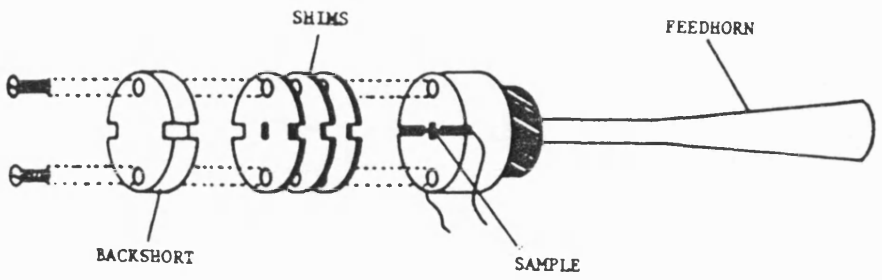

Figure 1. Detector mount

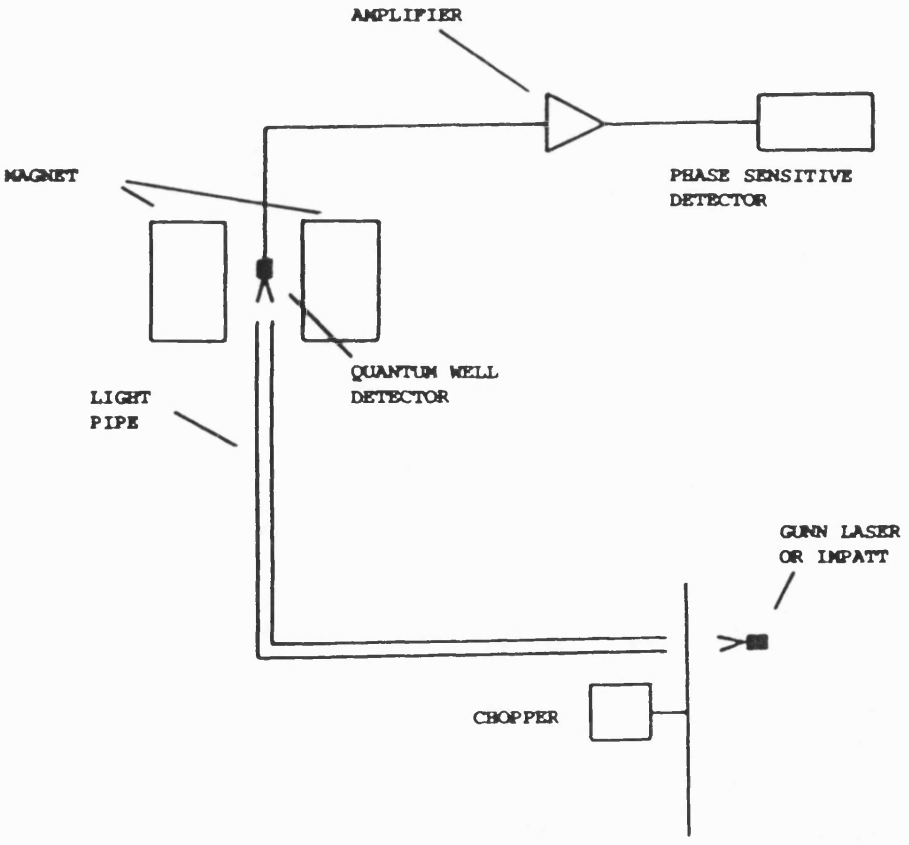

Figure 2. Experimental set-up

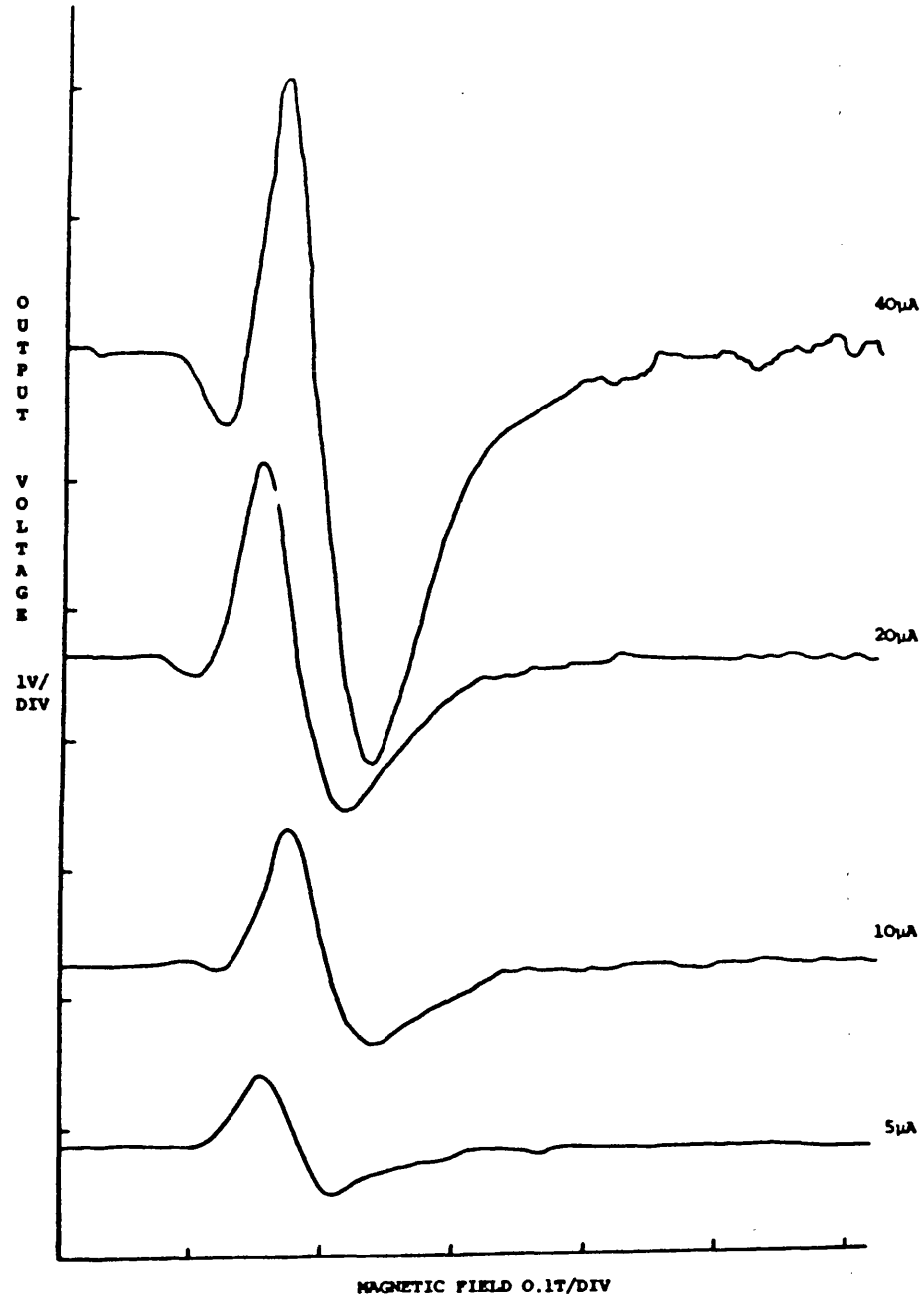

Figure 3. 94GHz detection at 0.2T input power 10μW, various d.c. bias currents

Results

Figures 3 to 5 summarise the results obtained. During our measurements the sample operating conditions were far from optimum since the magnet system used is not ideal for mm-wave experiments. Nevertheless the results show great

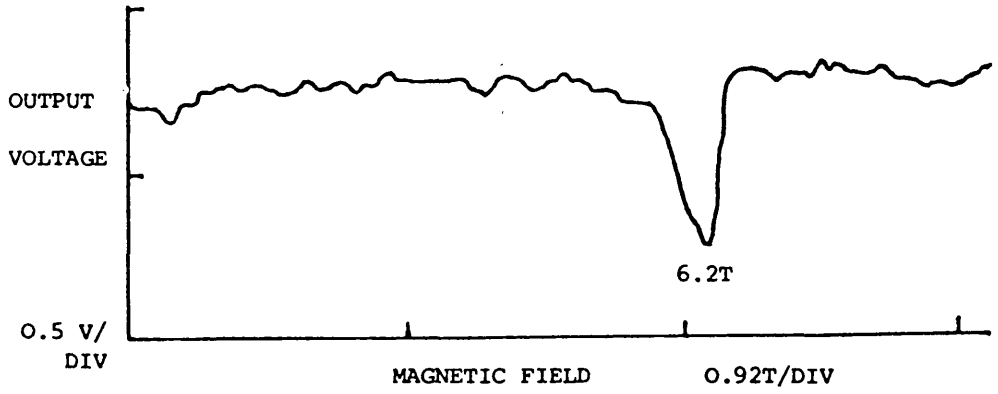

Figure 4. 119μm detection at 6.2T

promise. Figures 3 and 4 show the detector output against applied magnetic field with 3.2mm and 119μm illumination respectively. As can be seen, there is a strong detection of the 3.2mm signal at a field of approximately 0.2T and a weaker detection of the 119 m signal at a field of 6.2T. These fields correspond approximately to the cyclotron resonance absorption observed directly in these structures [4], although the lineshapes are somewhat different. The linewdiths are of order 0.05T or less, indicating the very high quality of these samples and suggesting that sharp tunability of the detection is possible. No conclusions about the responsivity can be drawn from the 119μm result since we were unable to assess the incident power levels. However, from the 3.2mm data, using reasonable assumptions concerning the mismatch of signal power to the detector we can obtain a very rough estimate of the responsivity to be approximately 200V/W. By measuring the amplitude of noise fluctuations seen on the trace we can also roughly estimate the N.E.P. of the detector to be approximately $5\times10^{-11}W/\sqrt{Hz}$.

Figure 5 shows a scan of the output of an Impatt oscillator tuned to give harmonics at 90 and 180GHz, illustrating the potential of the device as a low resolution scanning spectrometer.

The exact mechanism of the response is not clear. Large signals were sometimes observed under zero bias conditions, indicating a photovoltaic response. In an earlier report on far infra-red and cm-wave photoconductivity, Stein et al [5] found a strong bolometric response modulating the D.C. conductivity in lower mobility samples.

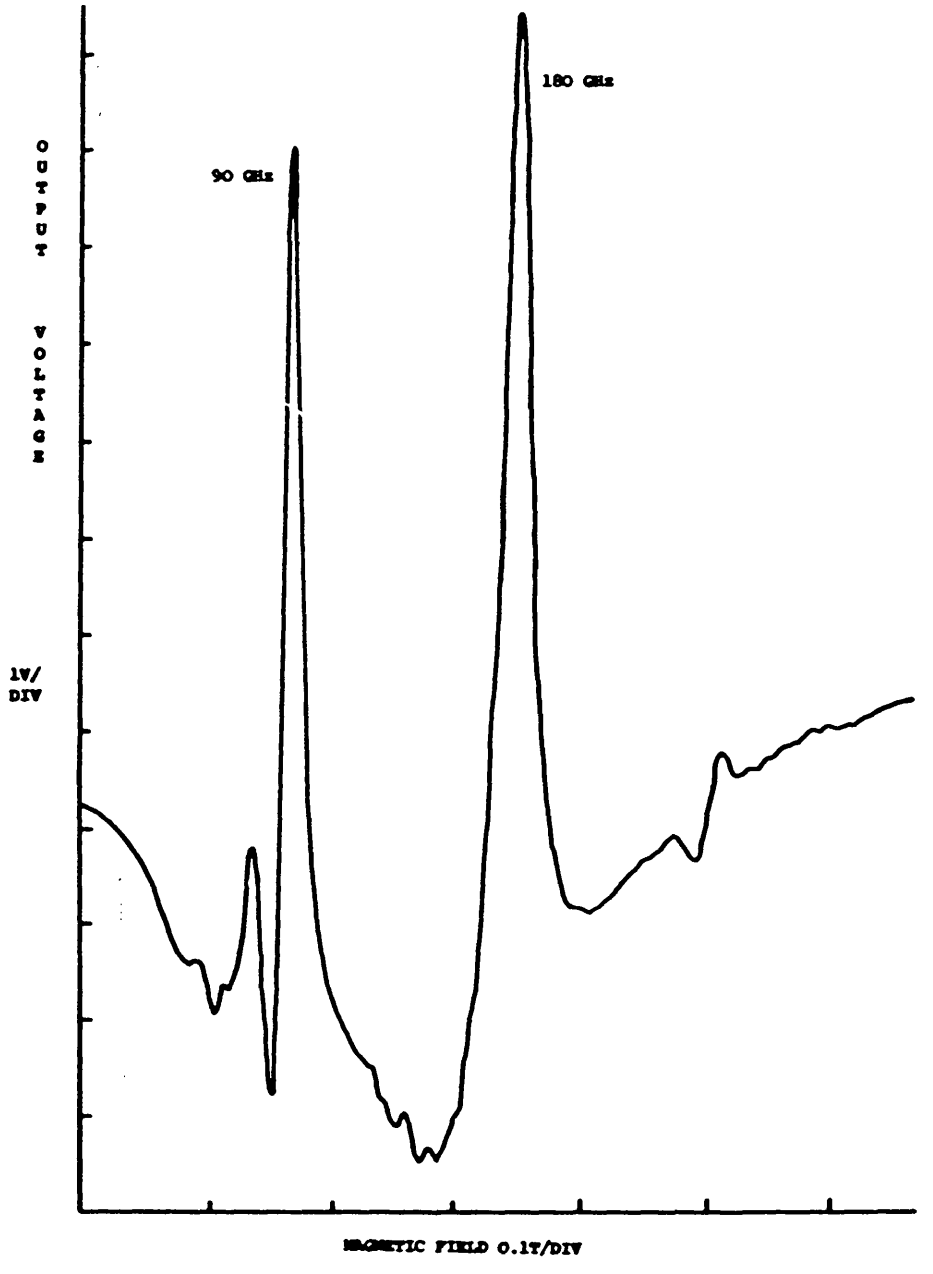

Figure 5. Harmonics from an impatt oscillator

Cyclotron resonance was only seen in the far infra-red, while at frequencies of 10-35GHz strong Shubnikov de Haas oscillations were observed together with a weak spin resonance. The cyclotron resonance appeared to be a photoconductive response, while the bolometric Shubnikov de Haas signals contained a slow response component attributed to variations in the lattice temperature. At the high chopping speed used during this experiment, only the

modulation of the resistivity due to electronic processes will be seen. Any modulation due to the change in the lattice temperature will have too high a time constant to be observed.

2 DEG Detector compared with other Detectors

The Schottky barrier diode is the standard millimetre wave detector/mixer [6]. It has the advantage of room temperature operation (although it benefits from cooling) but relies for its high frequency performance upon the very low capacitance of the rectifying junction. Therefore as the operating frequency increases, the area of the junction must fall correspondingly. Obviously the accuracy achievable by photolithography sets an upper limit on the frequency for which diodes can be made. The 2 DEG detector being a bulk (or more properly sheet) device does not suffer from this limitation. Another fundamental limitation of the S.B. diode, as far as the sub-mm is concerned, is the high level oscillator (L.O.) requirement in mixer applications ($\simeq$ 1mw). In comparison, the 2 DEG detector should require less than 1μw.

A better comparison can be made with the InSb detector/mixer. This is also a helium cooled bulk device, typical responsivity and N.E.P. for an InSb bolometer being 1750V/W and 3×10^{-12}W/$\sqrt{\text{Hz}}$ respectively [7]. As can be seen allowing for the non-optimal conditions under which the 2 DEG detector was tested, the results are very comparable. The weakness of InSb lies in the comparative slowness of the response (compared with the Schottky barrier diode). Typical response times are in the region of 10^{-6}s giving I.F. bandwidths (mixer) of at most 1MHz [8]. For comparison the estimated relaxation times for transitions between Landau levels in the 2 DEG are of the order of 10^{-10} seconds [9]. I.F. bandwidths could therefore be several orders of magnitude greater.

A relatively recent development has been the superconductor insulator superconductor (SIS) detector [10]. This is a helium cooled device with low L.O. requirement and good performance both in terms of noise and speed. The limitation of this detector, however, is that once again it relies on small area junctions for its high frequency performance.

The 2 DEG structure has several other significant advantages:

(a) Since the mobile carriers in the well originate from donors outside of the well they are unable to recombine as the temperature is reduced. Hence the crystal will remain conducting even at the lowest temperatures.

(b) The impedance of a typical device at 4.2K is expected to be around 50 ohms which is ideal for matching to a low noise amplifier.

(c) It may be possible to increase the sensitivity of the detector by growing a number of heterojunctions or quantum wells in parallel. This is an additional degree of freedom not shared by InSb.

(d) The number of carriers in the well may be varied by illumination by visible light or by gating with a third electrode. Again this is a degree of freedom for optimization not available to other detectors.

(e) Standard GaAs ohmic contact technology (e.g. alloyed Ge-Au-Ni) can be adapted to make low noise contacts to the crystal. This is important since the development of contact technology has been a major component in the optimization of other detectors. Such contacts are readily formed using photolithographic techniques and proton isolation can be used to define small active areas. Hence array detector systems may be made possible with the 2 DEG detector.

Acknowledgements

The authors wish to thank C. White and J. Hewett for technical assistance. One of us (S.M.S.) is grateful to the Science and Engineering Research Council for a research studentship.

References

1. H.L. Stormer, R. Dingle, A.C. Gossard, W. Wiegmann and M.D. Sturge "Two-Dimensional Electron Gas at a Semiconductor-Semiconductor Interface", Solid State Comm. 29, 705-709 (1979).

2. C.T. Foxon and J.J. Harris, "Growth of High Purity III-V Structures by Molecular Beam Epitaxy", Philips J. Res. 41, 313-324 (1986).

3. F. Stern and S. Das Sarma "Electron Energy Levels in GaAs/$Ga_{1-x}Al_xAs$ Heterojunctions", Phys. Rev. B 30, 840-847 (1984).

4. M.A. Hopkins, R.J. Nicholas, M.A. Brummell, J.J. Harris and C.T. Foxon, "Cyclotron Resonance and Screening Effects in GaAs/GaAlAs Heterojunctions", Proc. Second Int. Conf. on Superlattices, Microstructures and Microdevices, Gothenburg, Superlattices and Micro-Structures, 2, 319-322 (1986).

5. D. Stein, G. Ebert, K. von Klitzing and G. Weimann, "Photoconductivity on GaAs/$Al_xGa_{1-x}As$ Heterostructures" Surf. Sci. 142, 406-411 (1984).

6. N.J. Cronin and V.J. Law, "Planar millimetre-wave diode mixer", IEEE Trans. Microwave Theory and Techniques, Bol. MTT-33, No. 9, 827-830 (1985).

7. M.A. Kinch, "Heterodyne Detection at mm Wavelengths using a Rollin InSb Bolometer", Appl. Phys. Letters 12 (3), 78-80 (1968).

8. T.G. Phillips and K.B. Jefferts, "A Low Temperature Bolometre Heterodyne Receiver for Millimetre wave Astronomy", Rev. Sci. Inst. 44, 1009-1014 (1973).

9. H. Sakaki, K. Hirakawa, J. Yoshino, S.P. Svensson, Y. Sekiguchi and T. Hotta, "Effects of Electron Heating on Two Dimensional Magnetotransport in AlGaAs/GaAs Heterostructures", Surf. Sci. 142, 306-313 (1984).

10. T.G. Phillips, D.P. Woody, G.J. Dolan, R.E. Miller and R.A. Linke, "Dayem-Martin (SIS Tunnel Junction) Mixers for Low Noise Heterodyne Receivers", IEEE Trans. Mag-17, 684-689 (1981).

A NEW SUBMILLIMETRE-WAVE DETECTOR USING CYCLOTRON RESONANCE IN $Ga_{1-x}Al_xAs$/GaAs HETEROSTRUCTURES

S.M. Smith, N.J. Cronin, J.J. Harris* and C.T. Foxon*

Millimetre-Wave Group, University of Bath, Bath, BA2 7AY, U.K.
*Philips Research Laboratory, Redhill, Surrey, RH1 5HA, U.K.

ABSTRACT

We have shown that a $Ga_{1-x}Al_xAs$/GaAs heterostructure can be used as a sensitive tunable detector of mm-wave/submm-wave radiation. The mechanism for detection requires the application of a magnetic field varying from approximately 0.2T at 94GHz (3.2mm wavelength) to 6.2T at 2500GHz (119μm wavelength). The speed of such a detector could be several orders of magnitude greater than comparable InSb detectors.

INTRODUCTION

The submillimetre region of the spectrum extends from 300 to 1000 GHz; exploitation of the full potential of this region has been restricted, however, by the limited range of devices which are capable of functioning at such high frequencies. One of the most significant shortcomings has been the absence of a fast submillimetre detector.

Recent experimental progress will be presented on the development of a new type of submillimetre detector, which we have already shown to respond to radiation ranging from 3.2mm to 119μm [1]. This new device is based upon recently developed $Ga_{1-x}Al_xAs$/GaAs heterojunction structures and for theoretical reasons the speed of such a detector could be several orders of magnitude greater than comparable InSb detectors.

$Ga_{1-x}Al_xAs$/GaAs HETEROJUNCTIONS

The physical system that we have been studying is a modulation doped $Ga_{1-x}Al_xAs$/GaAs heterojunction, with x typically 0.33. This consists of a narrow band-gap layer of GaAs in contact with a wider band-gap $Ga_{1-x}Al_xAs$ layer. A dopant impurity usually Si is incorporated into the $Ga_{1-x}Al_xAs$ layer and free carriers from this region can diffuse into the undoped GaAs, causing an accumulation layer to be formed in the GaAs at the heterojunction. The conduction band discontinuity at this point provides a potential barrier which restricts the return of the electrons into the $Ga_{1-x}Al_xAs$. The band bending in the GaAs caused by the accumulation region produces an approximately triangular, one-dimensional potential well perpendicular to the interface. Carrier motion in the perpendicular direction is quantised, forming a set of bound energy states. Motion along the interface remains unhindered and is practically free from ionised-impurity scattering (the limiting factor for the low-temperature mobility) because of the spatial separation of parent donors and free electrons [2]. Using molecular beam epitaxy single wells may be grown or multiple layers can be formed to produce the so called superlattice structure. Electrical contact to the well or wells is made via ohmic contacts formed using standard GaAs processing techniques.

THE 2 DEG DETECTOR

As described above, the two dimensional electron gas exists in a set of sub-bands created by the confinement of the quantum well. The energy separation of these sub-bands is too great to be of direct interest in the wavelength range considered here. However, upon application of a magnetic field each sub-band further divides into Landau levels the energy separation of which is determined by the magnitude of the applied field. Incident electromagnetic waves are absorbed by exciting transitions between Landau levels provided that the frequency equals the cyclotron resonance frequency. Cyclotron resonance may be used as the basis of a detector if the resistance of the crystal depends upon the occupancy of the Landau levels. Absorption of a photon inducing a transition then gives rise to a change in the resistance of the crystal which can be transformed to a voltage change by application of a constant current bias.

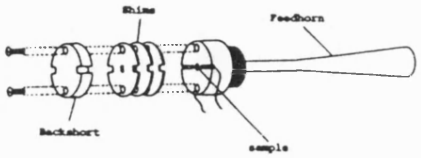

Figure 1
Detector mount

We have recently conducted a series of experiments in which we have used a heterojunction to detect signals from a 94GHz Gunn oscillator, a 119μm laser and a multifrequency Impatt oscillator. The sample was mounted across a rectangular waveguide in a specially designed detector mount, shown in figure 1. The backshort was arranged using shims to be a distance of approximately one quarter of a guide wavelength from the sample, at 94GHz. Signals from the sources were modulated by a 1kHz chopper and then passed along a light pipe to the detector which was situated at the centre of a magnet. The 2 DEG heterostructure was constant current biased and the output voltage amplified and phase sensitively detected. Input power level was adjusted by the variable attenuator and measurements were taken at 4.2K.

PRELIMINARY RESULTS

Figures 2 to 4 summarize the results obtained. During our measurements the crystal operating conditions were far from optimum since the magnet system used is not ideal for mm-wave experiments. Nevertheless these results already show great promise. Figures 2 and 3 show the detector output against applied magnetic field with 3.2mm and 119μm illumination respectively. As can be seen, there is a strong detection of the 3.2mm signal at a field of approximately 0.2T and a weaker detection of the 119μm signal at a field of 6.2T.

Figure 4 shows a scan of the output of an Impatt oscillator tuned to give harmonics at 90 and 180GHz. The potential of the device as a low resolution scanning spectrometer is clearly demonstrated by this result.

CH2490-1/87/000-0233 $1.00 ©1987 IEEE

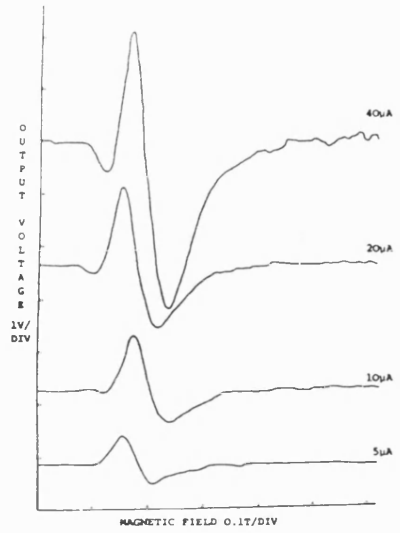

Figure 2
94GHz detection at 0.2T input power 10μW, various d.c. bias currents

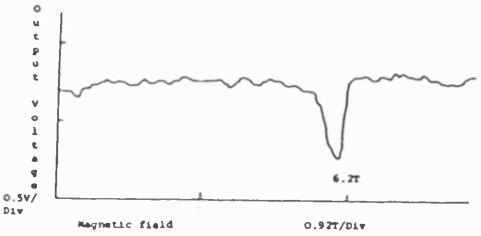

Figure 3
119μm detection at 6.2T

Currently, the fastest bulk submillimetre detector is the InSb hot electron bolometer. It is therefore interesting to compare the energy relaxation time for hot electrons in InSb with the relaxation time between Landau levels in the 2 DEG detector. The relaxation times are in the order of 10^{-6}S [3] and 10^{-10}S [4] respectively, from which we can conclude that the 2 DEG detector could be up to four orders of magnitude faster than InSb. InSb is often used as a mixer in submillimetre receivers, its bandwidth being limited to approximately 500kHz by the speed of the crystal. A system based upon a 2 DEG detector may therefore be expected to have a useable bandwidth of up to 5GHz.

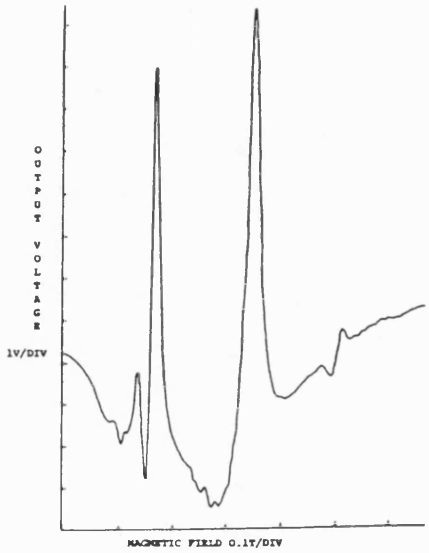

Figure 4
Harmonics from an impatt oscillator

REFERENCES

[1] S.M. Smith, N.J. Cronin, R.J. Nicholas, M.A. Brummell, J.J. Harris and C.T. Foxon. *Int. J. IR and MM Waves*, 1987, vol. 8

[2] H.L. Stormer, R. Dingle, A.C. Gossard, W. Wiegmann and M.D. Sturge. *Solid State Commun.* 1979, vol. 29, pp. 705-709

[3] J.J. Whalen. "Mixing and Energy Relaxation in Indium Antimonide" *Ph.D. Thesis, The Johns Hopkins University*, 1969.

[4] H. Sakaki et al. *Surface Science*, 1984, vol. 142, pp. 306-313